TECHNISCHE
UNIVERSITÄT
WIEN

Vienna University of Technology

CERN

DISSERTATION

Energy Verification in Ion Beam Therapy

Ausgeführt zum Zwecke der Erlangung des akademischen Grades eines
Doktors der technischen Wissenschaften
unter der Leitung von

Privatdoz. Dipl.-Ing. Dr.techn. Michael Benedikt

Institutsnummer: E141
Atominstitut der Österreichischen Universitäten

eingereicht an der Technischen Universität Wien

Fakultät für Physik

von

Dipl.-Ing. Fabian Moser

Matrikelnummer 0225488
Mittelgasse 35/22, 1060 Wien

Wien, im Mai 2012

_____
(Dipl.-Ing. Fabian Moser)

Zusammenfassung

Ionenstrahltherapie ist eine Methode zur Behandlung von malignen Tumoren, meist mit Protonen oder Kohlenstoff-Ionen. Sie hat den Vorteil, dass vor allem bei tief liegenden Tumoren das umliegende Gewebe deutlich weniger belastet wird als bei konventioneller Strahlentherapie, was am abrupten Anstieg und anschließenden Abfall ("Bragg-peak") der im Gewebe deponierten Dosis liegt.

Damit Ionen bis zu den erforderlichen Eindringtiefen von etwa 30 cm in Gewebe eindringen, müssen sie auf eine entsprechende kinetische Energie von etwa 250 MeV bei Protonen oder etwa 400 MeV/n bei Kohlenstoff-Ionen beschleunigt werden. Durch eine Kombination verschiedener Energien ("Stapeln" der Bragg-peaks) wird eine gleichmäßige Dosisverteilung erzielt.

Die medizinischen Verwendung des erzeugten Strahls stellt weitreichende Anforderungen an die Entwicklung und Konstruktion des Beschleunigers und der eingesetzten Software. Eine "online" Überwachung sämtlicher Strahlparameter erlaubt die frühzeitige Erkennung von Abweichungen derselben von den jeweiligen Vorgabewerten und dient der Begrenzung der mit solchen Abweichungen verbundenen Risiken. Die vorliegenden Arbeit behandelt in diesem Zusammenhang die Verifikation der Strahlenergie.

Im ersten Schritt wurden die Auswirkungen fehlerhafter Strahlenergien auf die Behandlung bzw. auf die erzeugte Dosisverteilung analysiert. Insbesondere mussten die maximal akzeptablen Abweichungen bei verschiedenen Energien und Teilchenarten bestimmt werden. Ein umfassender Überblick über mögliche Methoden zur Messung von Teilchenenergien bestimmt für jede Methode die den Anforderungen entsprechenden Kenndaten und nennt gegebenenfalls Beispiele für den Einsatz an bereits existierenden Anlagen. Es stellte sich heraus, dass die Anforderungen am ehesten von einer Flugzeitmessung oder von einer Messung der Dosisverteilung bei Absorbtion der Teilchen erfüllt werden. Diese beiden Methoden wurden anschließend im Detail betrachtet.

Eine Flugzeitmessung in einem Synchrotron erfordert eine Messung des Umfangs des geschlossenen Orbits und der Umlauffrequenz des Teilchenpakets. Der Umfang wird aus den über das Synchrotron verteilten Strahlpositionsmessungen berechnet. Dabei spielt nicht nur die vorgesehene Genauigkeit der Positionsmessungen sondern auch deren Verteilung entlang des Beschleunigers eine Rolle. Außerdem muss die Art, Lage und Genauigkeit der Beschleunigermagneten berücksichtigt werden. Eine Simulation möglicher Magnet- und Messfehler zeigt die erzielbare Genauigkeit der Umfangsmessung. Die Genauigkeit der Messung der Umlauffrequenz bestimmt sich vor allem aus der Dauer der Messung.

Da keine der existierenden Dosisverteilungsmessungen eine ausreichende Geschwindigkeit und zugleich Genauigkeit aufweist, wurde für diese Messung ein Konzept eines neuen Detektortyps entwickelt. Aufgrund der hohen Strahlenhärte fiel die Wahl auf einen Diamantdetektor, wobei anhand von detaillierten Simulationen mit realistischen Strahleigenschaften und Detektordimensionen gezeigt wurde, dass eine Anordnung von zwei handelsübliche Detektoren in Kombination mit einem passenden Reichweitenmodulator die gestellten Anforderungen erfüllt.

Abstract

Ion beam therapy is a method for treatment of malignant tumours, mostly with protons or carbon ions. It has the advantage that the tissue surrounding the tumour receives significantly less dose compared to conventional radiation therapy because of the abrupt rise and subsequent decay ("Bragg peak") of the dose deposited in tissue.

In order to penetrate to the necessary depths of up to $30\,\mathrm{cm}$ in tissue, the ions must be accelerated to energies of about $250\,\mathrm{MeV}$ in case of protons or about $400\,\mathrm{MeV/n}$ in case of carbon ions. By a combination of different energies ("stacking" of Bragg peaks), a homogeneous dose distribution is achieved.

The adoption of accelerators for medical applications has significant implications concerning the requirements towards development and construction of the accelerator hardware and software. An on-line verification of all beam parameters provides early detection of erroneous parameters and serves the reduction and limitation of associated risks. In this context, this thesis examines the verification of the ion beam energy.

First, the consequences of an irradiation with incorrect beam energies had to be analysed. In particular the maximum acceptable errors at different energies and for different particle types had to be determined. A comprehensive overview of possible methods for energy verification lists the specific requirements for each method from the maximum acceptable errors and, where possible, discusses examples for depolyment at existing facilities. It turns out, that the imposed requirements are best met by either a time-of-flight measurement or a measurement of the depth-dose distribution during particle absorption. These two methods are therefore studied in detail afterwards.

A time-of-flight measurement in a synchrotron consists of a measurement of the closed orbit circumference and the bunch revolution frequency. The circumference is computed from beam position measurements distributed along the synchrotron ring. The precision of the circumference measurement depends not only on the precision of those measurements, but also on their locations along the ring and on the type, position and precision of the lattice magnets. A simulation of the foreseen magnet and measurement errors determines the circumference precision that can be achieved. The precision of the revolution frequency measurement mainly depends on the measurement duration.

Since there exists no fast and precise depth-dose measurement concept, a new detector concept had to be developed for that purpose. Due to its outstanding radiation hardness, a diamond-based detector concept was chosen. Detailed simulations using realisitc beam properties and detector dimensions showed that a design based on two off-the-shelf diamond layers in combination with a range shifter is able to fulfill the requirements.

Acknowledgements

This thesis would not have been possible without the support of many people. First and foremost the author wishes to express his gratitude to his supervisor, Privatdoz. Dr. Michael Benedikt, project leader of MedAustron, who offered the great opportunity of this work as well as his invaluable support and guidance. At this point the opportunity shall not be missed to thank Prof. Dr. M. Regler whose commitment to the MedAustron project has been inspiring and was certainly the seed of this work. Sincere gratitude are also due to MedAustron team members Dr. Ulrich Dorda and Dr. Johannes Gutleber without whose assistance this research project would not have been successful. Dr. Gutleber was of immense help in understanding and establishing the objectives of this work and his supervision and experience helped to keep this project on track and focused, especially during the early stages. Dr. Dorda offered his sustained and generous support throughout this entire work and was always willing to share his knowledge and experience. His indispensable help in discussions, hints, corrections and feedback in general is greatly appreciated. Special thanks also go to Marcus Palm, for sharing thoughts, challenges, references and an office.

Contents

Abbreviations

ADC   Analogue-to-digital converter

ALPF   Analogue low-pass filter

BGO   Bismuth germanium oxide

BPM   Beam Position Monitor

CCE   Charge Collection Efficiency

CERN   Conseil Européen pour la Recherche Nucléaire

CMS   Compact Muon Solenoid

CVD   Chemical Vapor Deposition

DLPF   Digital low-pass filter

DNA   Deoxyribonucleic acid

FFT   Fast Fourier Transform

FWHM   Full Width Half Maximum

GSI   GSI Helmholtzzentrum für Schwerionenforschung; formerly Gesellschaft für Schwerionenforschung

HEBT   High Energy Beam Transfer line

INFN   Istituto Nazionale di Fisica Nucleare

LET   Linear Energy Transfer

LLUPTF   Loma Linda University Proton Treatment Facility

MCD   Minimum-Covariance Determinant

MCP   Micro-Channel Plate

MDACC   University of Texas MD Anderson Cancer Center

MIP   Minimum Ionising Particle

MLFC   Multi-Layer (or Multi-Leaf) Faraday Cup

MTBF	Mean Time Between Failures
MTTR	Mean Time To Recover
MWW	Mann-Whitney-Wilcoxon test, also called Mann-Whitney U test
PCA	Principal Component Analysis
PET	Positron Emission Tomography
PIMMS	Proton-Ion Medical Machine Study
PMMA	Polymethylmethacrylate; also acrylic glass or Plexiglas™
PSI	Paul Scherrer Institut, Villigen
RBE	Relative Biological Effectiveness
RF	Radio Frequency; often refers to the Radio Frequency accelerating cavity
RMS	Root Mean Square
SEM	Secondary Emission Monitor
SNR	Signal-to-Noise Ratio
SPS	Super Proton Synchrotron
ToF	Time of Flight
w.-eq.	water-equivalent
w.r.t.	with respect to

Nomenclature

$\bar{\square}$	average or mean value e.g. average velocity $\bar{v}$
$\sigma_\square$	uncertainty or standard deviation e.g. uncertainty of the velocity σ_v
β, γ	relativistic factors, where $\beta = v/c$ and $\gamma = m/m_0$
B	magnetic field
c	speed of light in vacuum
C	circumference
C_0	circumference of the reference orbit
E_k	kinetic particle energy
f	frequency
ℓ	length or arc length
m, m_0	particle mass and rest mass
N	total count e.g. number of particle or number of elements
p	particle momentum
q	particle charge
Q, Q_{res}	Tune and resonance tune
ρ	arc radius
s	local longitudinal co-ordinate
θ	arc or bending angle
t	time
T	time period e.g. observation period or record length
v	velocity
x, y	local transverse, i.e. horizontal and vertical, co-ordinates for the beam

1. Ion Beam Therapy

1.1. Medical motivation

1.1.1. Cancer

Cancer (medically: malignant neoplasm) is one of the main causes of death to date. In Europe, the probability to die of cancer is 25 % averaged over all sexes and ages, which is second only to diseases of the circulatory system [62]. At the same time, the probability to be cured after a diagnosis is about 47 % [33]. The cures are as manifold as the number of cancer types, including surgery, chemotherapy, radiation therapy, immunotherapy, monoclonal antibody therapy and other methods. Conventional radiation therapy with photons or electrons (see section 1.1.2 below) is one of the most common treatments. As much as 70 % of all cancer patients receive this type of treatment either as primary or as adjuvant therapy, i.e. in combination with other treatments such as surgery or chemotherapy [45].

1.1.2. Radiation therapy

Radiation therapy is the use of ionising radiation to penetrate human tissue and destroy the cancer cells by inflicting radiation damage. This damage mainly concerns the DNA of the cell, prohibiting the self-reparatory and duplication mechanisms of the cell to recover from the suffered damages.

Figure 1.1 shows the results of a Geant4 [9] simulation of depth-dose distributions of different types of ionising radiation, namely photons, electrons, protons and carbon ions. Regarding the photon dose distribution, it must be noted that in practice, i.e. during conventional radiation therapy, a broad spectrum of photon energies is generated, usually by means of Bremsstrahlung of fast electrons in an anode, while in the displayed example only a mono-energetic photon beam has been simulated. Nevertheless, in order to achieve an increased dose in the tumour compared to the surrounding healthy tissue using conventional photon radiation, the irradiation must be applied from different angles, focussing in the target region. One remarkable feature of photon radiation is the low dose level at the entrance, hence the potential to spare the skin compared to other types of radiation. The dose build up observed within the first part of the depth-dose distribution stems from secondary electrons emitted in the forward direction.

For the treatment of superficial tumours and if the underlying tissue should be spared, electron beams are more appropriate than photons, because the dose deposited by this type of radiation drops after a certain dose maximum as can be seen in figure 1.1. The position of the dose maximum as well as the maximum depth at which a significant dose
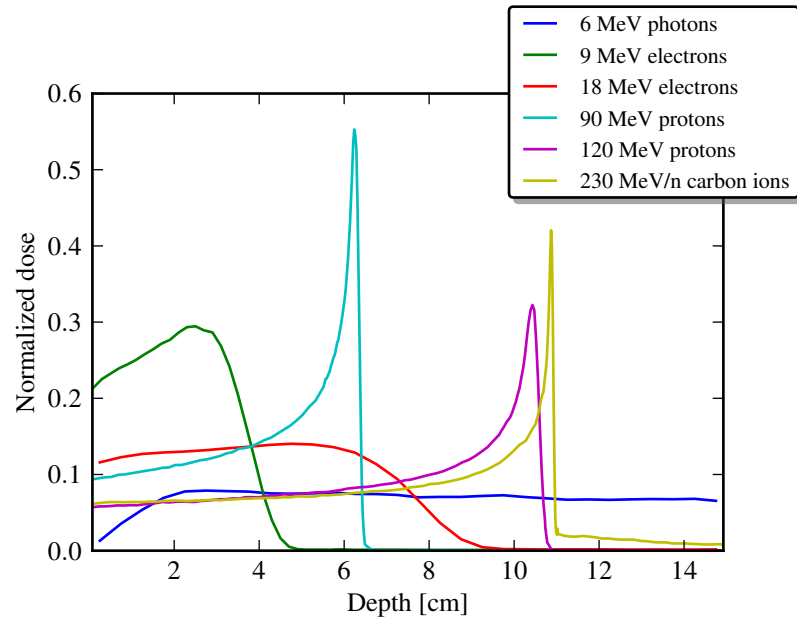
Figure 1.1.: Comparison of simulated depth-dose distributions of different types of ionising radiation in water. The curves have been normalised such that the integrated dose within the displayed range is equal.

is applied is determined by the electron energy.

As first remarked by Wilson [94], for the treatment of deep seated tumours (above a few centimetres), the dose distribution of protons or carbon ions (or ions in general) outmatches that of photons and electrons: The pronounced peak (the so-called Bragg peak) together with the following steep dose fall-off allows for high dose gradients within the irradiated tissue and therefore good dose confinement and minimisation of side-effects.

1.1.3. Indications for ion beam therapy

Indications for ion beam therapy are based on its properties compared to conventional photon beams, especially the reduced dose to adjacent normal tissue. For this reason, but also due to the relatively low required penetration depth and thus beam energy, ion beam therapy has been an accepted treatment modality for uveal melanoma. For cases that cannot be treated satisfactorily with brachytherapy because of the thickness of the melanoma or its vicinity to the optic nerve, ion beam therapy is recommended [80]. For paediatric tumours it is assumed that ion beam therapy is in general superior to photon radiation therapy because of the expected reduced risk for secondary malignancies due to the reduced dose to normal tissue. While skull base chordomas and chondrosarcomas are most often treated by surgery, incomplete resection due to vulnerable normal tissue can be compensated by adjuvant high-dose ion beam therapy.

Another indication for ion beam therapy may be the treatment of certain tumours suspected of possessing radiation resistant regions containing hypoxic cells. Compared to photon radiation, the reduction in the oxygen enhancement ratio as well as in the cell cycle sensitivity may be advantageous in these cases.

1.1.4. Experiences

Currently there are 37 operating ion beam therapy facilities in the world, not including 17 that are under construction and 2 that are planned [72]. Most of them feature cyclotron accelerators (see section 1.2.2) and therefore provide proton beams only. More than 84000 patients have received an ion beam treatment, about 90 % of which has been proton therapy. The published studies with the highest number of patients are those regarding either treatment of uveal melanomas or prostate cancer. Egger et al. [32] report that excellent eye retention rates at 5 years between 89.5 and 100 % depending on the tumour size have been achieved at the Paul Scherrer Institut (PSI) with proton beam therapy for uveal melanomas. From the Loma Linda University Proton Treatment Facility (LLUPTF), Slater et al. [84] report disease-free survival rates comparable with other forms of local therapy and minimal morbidity when using proton therapy for treatment of prostate cancer. Results of carbon ion radiotherapy conducted at the GSI Helmholtzzentrum für Schwerionenforschung (GSI) show high local control rates for skull based tumours and confirm the safety of this treatment type with respect to toxicity [81].

1.2. Ion beams

1.2.1. RBE and particle types

In addition to the different depth-dose distribution of ions compared to photons used in conventional radiotherapy (see section 1.1.2), their efficiency in producing cell kill is also increased [45]. In order to allow for treatment planning and comparison on the basis of the biological effect, the concept of Relative Biological Effectiveness (RBE) is commonly used. The RBE is defined as the ratio of the absorbed doses of a reference photon beam and a beam of any other radiation yielding the same biological effect. Unfortunately, the RBE cannot be uniquely defined for a given radiation, but varies with particle type and energy, dose, dose per fraction, degree of oxygenation, cell or tissue type, biological end point and other parameters.

Within certain limits, the RBE further amplifies the Bragg peak of the deposited dose via its dose dependency. This effect is most pronounced for carbon ions compared to lighter or heavier ions. Therefore carbon ions are an increasingly popular and investigated choice among particle types for ion beam therapy in parallel to protons, which are the most easy to handle due to their favourable charge to mass ratio.

1.2.2. Particle accelerators

All existing or planned ion beam therapy facilities feature either a cyclotron or a synchrotron as main particle accelerator. The cyclotron delivers a high intensity continuous beam. It is much more compact, easier to handle and maintain and overall less expensive than the synchrotron. On the other hand it has only one fixed extraction energy and no carbon ion cyclotrons exist at present. In order to obtain the different beam energies, the beam energy must be adjusted by shooting the beam through absorbers of different thickness. The particles are slowed down by scattering processes resulting in a broad energy distribution and a spectrometer-type beam line performs energy selection at the cost of beam intensity.

When the use of other than proton beams is planned, a synchrotron is the accelerator of choice. The synchrotron extraction energy of the ion beam can be selected on a cycle to cycle basis, providing exactly the desired beam energies with a narrow energy spread.

The main difficulty in widespread use of ion beam therapy is the size and cost of both of the above mentioned accelerator types. Efforts to develop and make available smaller and less expensive accelerators such as ultra-compact synchrotrons or Dielectric wall accelerators [56] are still in the early research stages.

1.3. Safety

The production of a high-energy ion beam involves a large number of devices and includes a significant amount of software involved with the control of those devices. The successful production of the ion beam is a matter of the correct and timely setting of a large number of parameters.

In order to avoid making assumptions about the correct functioning of the beam production, it is obligatory to verify the output, i.e. the characteristics of the produced ion beam. This is required especially when the ion beam is used for medical treatment. If the beam is to be used in non-clinical research only, such a verification is not obligatory, since incorrect beam parameters do not endanger persons.

Apart from the verification of the particle type, intensity, profile, angle and position, it is equally important to verify the exact energy of the ions, as it affects the treatment success to the same degree. Reliable verification of all of the mentioned parameters is expected to significantly relax the complexity and cost of risk management concerning the medical treatment.

1.3.1. Regulations

Several international and national safety regulations must be respected when developing, constructing or operating an ion beam therapy facility in Austria, most notably the following:

- The European directive concerning medical devices 93/42/EEC [1] ("medical device directive") and its national implementation.

- The European directive concerning the health protection of individuals against the dangers of ionizing radiation in relation to medical exposure 97/43/Euratom [4] and its national implementation.

- The European directive laying down basic safety standards for the protection of the health of workers and the general public against the dangers arising from ionizing radiation 96/29/Euratom [3] and its national implementation.

- The European directive on machinery 2006/42/EC [5] and its national implementation.

1.3.2. The Medical Device Directive

The directive 93/42/EEC concerning medical devices is applied in Austria through the Medizinproduktegesetz [2]. A medical device is, amongst other definitions, any instrument, apparatus or appliance to be used for human beings for the purpose of treatment or alleviation of disease. Following the classification established in the directive, an ion beam treatment facility is considered a class II b medical device and therefore requires inspection by a notified body with regard to the design and manufacture of the device. One of the central requirements imposed by this directive is to *eliminate or reduce as far as possible risks* when adopting solutions for the design and construction of the medical device. For more specific requirements arising from this directive see its Annex I.

Relevant standards where conformity results in presumed compliance with this directive are:

- EN ISO 13485:2003 Medical devices – Quality management systems — Requirements for regulatory purposes

- EN ISO 14155:2003 Clinical investigation of medical devices for human subjects

- EN ISO 14971:2007 Medical devices – Application of risk management to medical devices

- EN ISO 15225:2000 Nomenclature – Specification for a nomenclature system for medical devices for the purpose of regulatory data exchange

Other relevant standards are:

- EN IEC 60601-1:2005 Medical electrical equipment – Part 1: General requirements for basic safety and essential performance

- EN IEC 62304 Medical device software – Software life cycle processes

The directive concerning medical devices does not affect the application of directive 97/43/Euratom and directive 96/29/Euratom. Devices which are also machinery shall also meet the essential health and safety requirements set out in Annex I to directive 2006/42/EC to the extent to which those essential health and safety requirements are more specific than the essential requirements set out in this directive.

1.4. Reliability, Maintainability and Availability

The aim of any beam verification measurement is not only to provide optimum patient safety through optimum performance, but also to provide it continuously, i.e. with high availability. In terms of reliability engineering, availability is a combination of reliability and maintainability.

Reliability is the probability that a device will perform its intended function during a specified period of time under stated conditions. The most common parameter for reliability is the Mean Time Between Failures (MTBF). The reliability of the energy prediction based on the energy budget depends on the reliability of the involved components and their role. If a failing component does not degrade the performance to an unacceptable level, that failure does not lead to a failure of the entire system (principle of redundancy).

The *maintainability* measures the ease with which a device can be maintained, i.e. defects can be corrected. Consequently, a suitable parameter for maintainability is the Mean Time To Recover (MTTR). For redundant systems, an MTTR of zero is possible if the system as a whole continues to operate without failure. However, the redundant components themselves need to be recovered upon failure and they always have a non-zero MTTR.

With those two parameters for reliability and maintainability, the *availability A* of a system can be obtained by the formula

$$A = \frac{\text{MTBF}}{\text{MTBF} + \text{MTTR}} \qquad (1.1)$$

As described above, for redundant systems a MTTR of zero is possible, but since no real system has an availability of one, the MTTR parameter makes no sense for the system as a whole. Therefore, the availability has to be derived from the system architecture and the component availability. The availability required by ion beam therapy facilities is usually at around 99 % [30, 79].

2. Ion Beam Energy

2.1. Beam energy

2.1.1. Energy range

Because the position of the Bragg peak is determined by the particle energy (see figure 1.1), the required set of particle energies is determined by the demanded range of depths accessible for treatment. The minimum depth for which ion beam treatment is used is determined by the dose fall-off of electron beams. Since electron beams are in general easier to generate and handle, they are preferred to ion beam treatment up to a range of about $3\,\mathrm{g/cm^2}$ (i.e. a depth of $3\,\mathrm{cm}$ in water). The maximum required depth is less clearly defined, but the most common choice is $25\,\mathrm{g/cm^2}$ (i.e. $25\,\mathrm{cm}$ in water) for the most deep-seated tumours.

For proton beams these ranges correspond to energies between 60 and $195\,\mathrm{MeV}$ at the entrance into the patient [11]. If passive beam spreading should be possible, the energy loss suffered from scattering must be accounted for. Therefore proton energies up to $250\,\mathrm{MeV}$ may be necessary. For carbon ion beams the above ranges correspond to particle energies between 120 and $400\,\mathrm{MeV/n}$ [20].

2.1.2. Depth-dose distribution

For efficient evaluation of energy-related dose errors, a semi-analytical depth-dose model developed by Bortfeld [18] has been used in this thesis. Of the available parameters of the mono-energetic model, only two change with the energy: R_0 and σ, corresponding to the particle range and the amount of longitudinal straggling respectively. Those two parameters have been determined by fitting the model to simulated dose distributions at 11 different energies for protons. The depth-dose distributions that served as the fit objectives have been generated by a dedicated Geant4 [9] application simulating 100000 primary particles in a water tank and scoring the total energy deposit (see figure 2.1a for a few selected energies and section 4.3 for further details of the simulation). For intermediate energies, the parameters have been stepwise interpolated.

Despite the different interaction processes, the same model has also been used for carbon ions, but all model parameters (i.e. also p, α, β and γ^1) were "freed" for the fit. The nature of the model implies that the increased neutron dose (especially behind the

---

[1]The parameters p and α are defined by the exponential energy-range relationship $R_0 = \alpha E_0^p$. β quantifies the fluence reduction due to nuclear interactions and γ represents the fraction of locally absorbed energy released in nonelastic nuclear interactions.

Bragg peak) is not accounted for. Nevertheless, the peak shape and the preceding dose plateau were reproduced well enough for the desired application (see figure 2.1b).

2.1.3. Energy spread

To get a comprehensive picture of the kinetic energies of the particles that impinge on the patient, not only the average kinetic energy but also the shape of the energy distribution or, more specifically, at least its width must be considered. The width of the energy distribution is often referred to as the "energy spread" and that term will also be used here. The energy spread can be either too high, when the dose fall-offs at the edges of the target region are too broad, or too low, when the treatment plan falsely relies on a certain energy spread, to guarantee dose homogeneity within the target.

For the betatron-core driven 3rd order extraction mechanism employed at MedAustron, the energy distribution is determined by the horizontal phase-space amplitude distribution of the waiting beam and the scale is determined by the parameters of the resonant sextupole and the lattice chromaticity Q'. The relation between the relative momentum offset and the normalised amplitude is [20, p.37]

$$\left|\frac{\Delta p}{p}\right| = A\left|\frac{S}{Q'}\right|\sqrt{\frac{1}{48\pi\sqrt{3}}}$$

where $S = \frac{1}{2}\beta_x^{3/2}\ell_s k'$ is the normalised (by β) sextupole strength and the other variables together with their respective value for the MedAustron synchrotron are: the chromaticity $Q' = -3.725$, the horizontal twiss function at the electrostatic septum $\beta_x = 8.77\,\mathrm{m}$, the effective magnetic length of the sextupole $\ell_s = 0.2\,\mathrm{m}$ and the normalised (by p) sextupole gradient $k' = 10.7\,\mathrm{m}^{-2}$.

Relating the momentum to the kinetic energy by

$$E_k = \sqrt{(pc)^2 + E_0^2} - E_0$$

where c is the speed of light and $E_0 = m_0 c^2$ is the mass-equivalent energy, results in the following relation between the relative kinetic energy offset and the relative momentum offset:

$$\frac{\Delta E_k}{E_k} = \frac{\gamma+1}{\gamma}\left|\frac{\Delta p}{p}\right| \tag{2.1}$$

and finally the relation between the relative energy offset and the normalised amplitude:

$$\left|\frac{\Delta E_k}{E_k}\right| = A\frac{\gamma+1}{\gamma}\left|\frac{S}{Q'}\right|\sqrt{\frac{1}{48\pi\sqrt{3}}} \tag{2.2}$$

The normalised amplitude is defined as $A = \sqrt{X^2 + X'^2}$ with the normalised phase-space coordinates $X = x/\sqrt{\beta_x}$ and $X' = x\alpha_x/\sqrt{\beta_x} + x'\sqrt{\beta_x}$, where α_x is the derivative of the Courant-Snider beta function ($\alpha_x = -\frac{1}{2}\frac{d\beta_x}{ds}$).
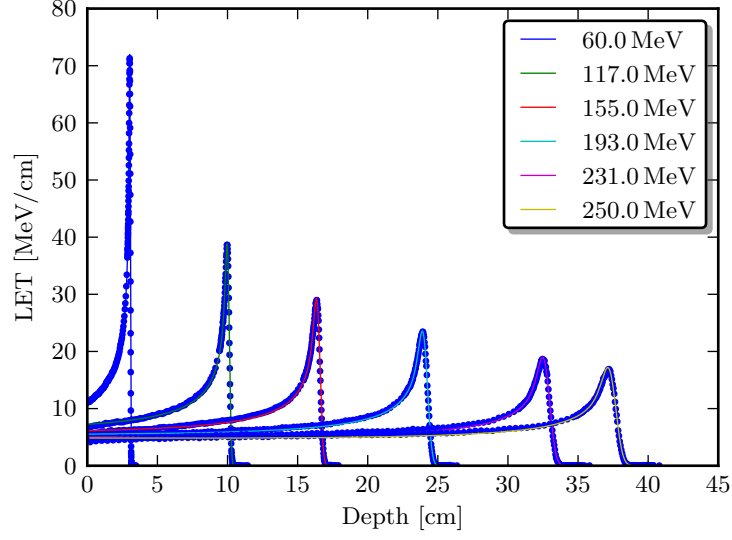
(a) Protons
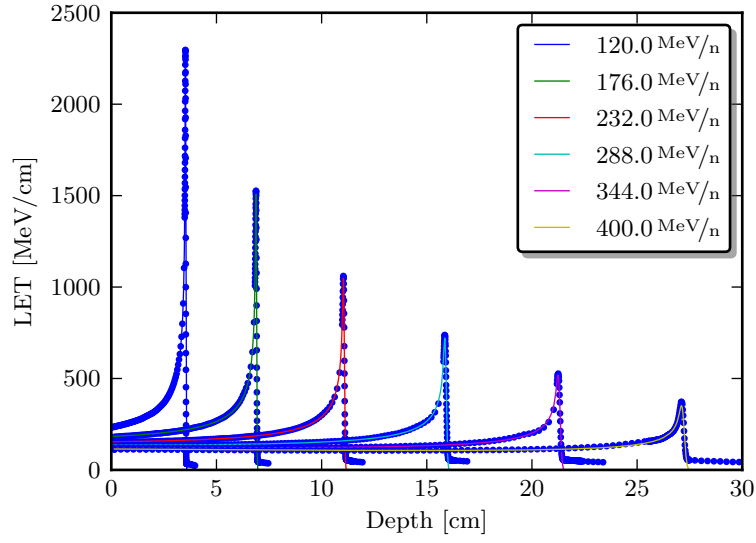
(b) Carbon ions

Figure 2.1.: Semi-analytical depth-dose model (lines) fitted to simulated dose distributions (dots) in water.
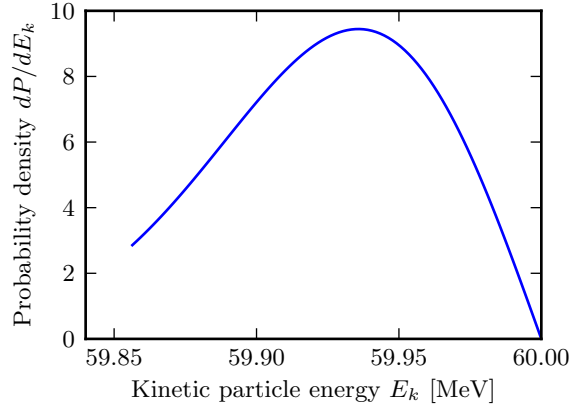
Figure 2.2.: Exemplary probability density function of the kinetic particle energy for a low-energy proton beam with a horizontal emittance of $\varepsilon_x = 1.4286\pi \, \text{mm mrad}$.

Hence, under the assumtion of a Gaussian amplitude distibution, the normalised amplitude distribution can be derived from a two-dimensional normal distribution in normalised horizontal phase-space with a standard deviation of $\sigma = \sqrt{\varepsilon_x/\pi}$, determined by the geometric horizontal emittance ε_x, which is subject to adiabatic damping (i.e. it decreases with increasing energy). To illustrate the expected energy spread of the extracted particles, figure 2.2 shows an exemplary distribution of kinetic particle energies of the extracted beam for a low-energy proton beam.

2.2. Energy stacking

Figure 2.3 shows the pin-shaped 3-dimensional dose distribution of a monoenergetic ion beam in water. In order to produce arbitrary depth-dose distributions for medical treatment, different ion beam energies must be used to place the Bragg peak at different depths (see figure 2.4). In the transverse plane, different beam positions on the surface allow to produce "spot-by-spot" different shapes. Different irradiation "intensities" allow to weigh the applied dose of each energy or spot. Additionally, irradiation from different sides of the irradiated object allow to minimise the dose near the surface. The irradiation directions, energies, spot positions and weights make up an irradiation plan (also called "treatment plan"). For medical treatment, the irradiation plan must balance two general requirements:

- The dose applied to the tumour must be above a certain minimum.

- The dose applied to healthy tissue must be as low as possible.

The optimum balance of these two requirements is achieved by a dose distribution which exactly equals the minimum level for the tumour region and is zero everywhere else. It is
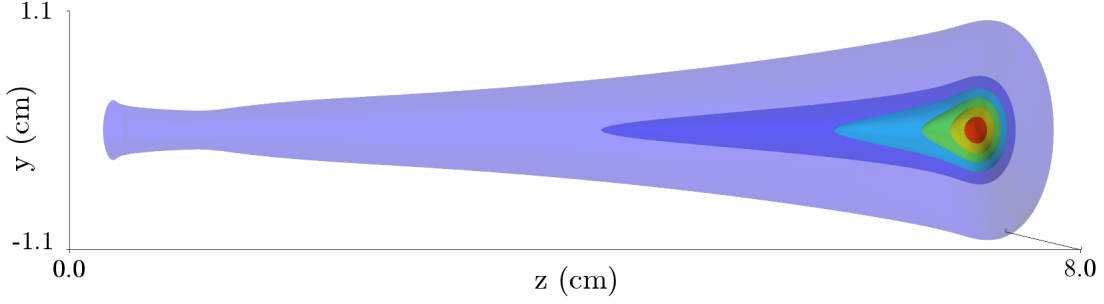
Figure 2.3.: Example of the dose distribution of a single spot at a depth of 7.6 cm in water irradiated with a proton beam at 100 MeV. The beam profile of the incident beam (at $z = 0$ cm) is Gaussian with a standard deviation of 1 mm in the transverse plane. Displayed are six equidistant isosurfaces of the applied dose. The outermost surface indicates 0.1 % of the maximum dose. The innermost surface indicates 90 % of the maximum dose.
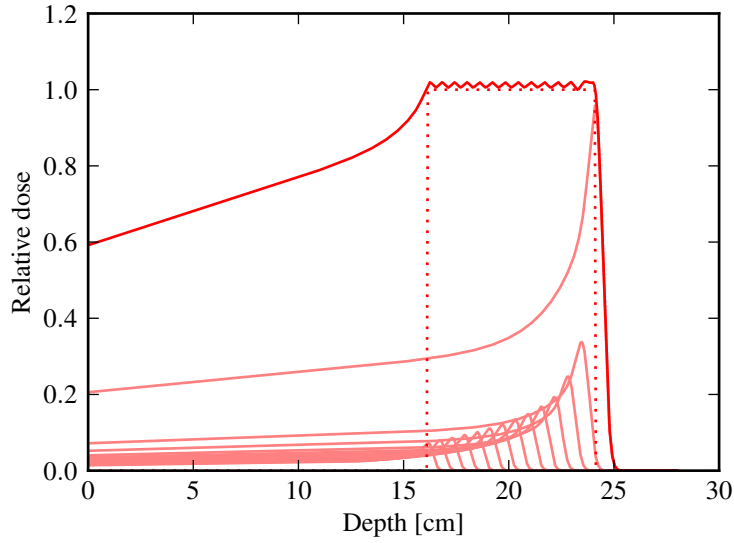
Figure 2.4.: Example of a dose distribution achieved by energy stacking. The irradiation target lies at depths between 16.2 and 24.2 cm as indicated by the vertical dashed lines. The Bragg peaks corresponding to 14 layers are produced by using protons with kinetic energies between 155 and 195 MeV.

clear from the depth-dose distributions shown in figures 2.3 and 2.4, that it is impossible to apply zero dose to the tissue around the tumour if the tumour should receive any dose at all. But it is possible to achieve roughly equal dose at every point in the tumour region.

2.2.1. Ridge filter

For low kinetic energies, the Bragg peak of the depth-dose distribution is sharper than for higher kinetic energies, because the particles suffer from less scattering (see also 2.2.4.3). Therefore, the sensitivity of the energy stack to energy errors is expected to be highest for the lowest energies.

In order to decrease the necessary layer density, it is foreseen that a ridge filter may be used, which "smears" the dose peaks by adding additional scattering and effectively broadening the energy distribution of the beam. Due to the wider Bragg peak a ridge filter also reduces the sensitivity to energy errors. When determining the acceptable energy errors (see section 2.3), the use of a ridge filter is assumed for carbon beams of all energies. For proton beams, a ridge filter is not required at high energies but may be optionally used for low energies. Hence, for low-energy proton beams both options are studied.

Where applicable, the properties of the ridge filter are similar to the one described by Weber and Kraft [90], i.e. approximately $2\,\mathrm{mm}$ thickness with a profile that introduces a Gaussian range smearing according to a standard deviation of $0.5\,\mathrm{mm}$ (water-equivalent). This smearing is achieved by a plate made of Polymethylmethacrylate (PMMA) of the cited thickness with a periodic structure of fine grooves that can be placed $60\,\mathrm{cm}$ upstream of the patient.

2.2.2. Quality measures

To judge the quality of a given dose distribution, first a figure of merit must be introduced which can be applied to the dose distribution and second, a limit in terms of that measure must be decided upon. This section introduces a few measures and defines the measure used for benchmarks later on.

2.2.2.1. Surface dose

It is unavoidable that the healthy tissue surrounding the irradiation target (e.g. a tumour) also receives a certain amount of dose. Naturally it is desired to keep this amount at a minimum while at the same time avoiding the dose at "cold spots" to drop below a certain minimum (see below).

One way to quantify the amount of healthy tissue exposure and to have a comparable measure, is to evaluate the dose deposited at the surface of the irradiated volume (e.g. the patient). The amount of dose deposited at the surface will be referred to as "surface dose" in the following.

2.2.2.2. Cold spots

The term "cold spot" in this context refers to a small region inside the target that receives less dose than its surroundings i.e. a local minima of the dose distribution. More specifically, such a region is only of interest, if it lies in the target area, where a certain minimum dose level is required. If the dose at a cold spot is below that minimum level, the risk that the tumour survives is increased and with it the risk of a treatment failure.

To avoid such risks, it makes sense to increase the overall dose such that potential cold spots are still at the minimum dose level. Of course this strategy also increases the dose applied to healthy tissue in general and the surface dose in particular.

2.2.2.3. Relative surface dose

This is the surface dose (at depth 0) of a given dose distribution divided by the dose of the coldest spot inside the target region, combining the two previous benchmarks. This provides an idea how much dose exposure the healthy tissue will receive if all layer weights are scaled up such that the cold spot receives the minimum necessary dose.

The ideal values for the relative surface dose vary for shallow and deep-seated tumours. Therefore this benchmark is not suited for a general comparison of stack quality.

2.2.2.4. Homogeneity

In order to discuss a dose homogeneity requirement, first a definition of what homogeneity means as well as how and where it is measured, must be agreed upon. Two candidates are:

- Dubini et al. [30, section 2.20] use a definition based on dose variations within a lower and upper depth limit, each anchored to a relative dose level with margins that depend on the the slope distal dose fall-off.

- The definition introduced by Weber and Kraft [90, equation (6)] (based on an integral of the squared offset) seems more intuitive but is more of theoretical nature and cannot easily be applied to depth-dose distributions.

Coutrakon et al. [25] avoid the explicit definition of a homogeneity measure, but mention $\pm 2\,\%$ inherent dose "non-uniformity" for the ideal dose distribution.

2.2.2.5. Choice of measure

Among the listed options for a quality measure, the cold spot measure is the most appropriate, because a bad performance in terms of minimum dose inside the target volume is the most critical problem during the treatment. Although exposure of healthy tissue is almost equally critical, the necessary exposure can vary greatly between different treatment situations and a measure including it therefore cannot be used for general comparison purposes. Homogeneity on the other hand is influenced by dose maxima in the target volume, which do not influence the quality of the treatment. *For the analysis*

of the influences of energy errors in this document, only the cold spot measure will be used.

2.2.3. Quality requirement

Requirements found in literature vary between 5 % dose errors [25] and 11 % inhomogeneity [30]. As an attempt to assume a reasonable, although admittedly somewhat arbitrary value, *a minimum cold spot value of* 90 % *of the intended dose will be used to deduce the energy verification requirements in this document.*

2.2.4. Treatment planning

2.2.4.1. Number of layers

An essential property of any treatment plan and thus any energy stack is the number of layers. The choice of this number is a trade-off between several factors:

- More layers lead to better homogeneity, therefore lower necessary overall dose in order to avoid cold spots and therefore also lower exposure of healthy tissue.

- Fewer layers result in a shorter treatment time, therefore lower probability of patient movement and also the ability to treat more patients in total.

The number of layers actually employed strongly depends on the shape and location of the target volume. For the purpose of comparison, if not mentioned otherwise, all simulations presented here use 10 layers over varying depth ranges, which are adapted to the achieved treatment plan homogeneity (in order to make treatment plans comparable at different energies), e.g. 1.2 cm for a 60 MeV proton beam up to 10 cm for a 250 MeV proton beam.

2.2.4.2. Planning strategy

While the above measures can all be applied to dose distributions which are more or less affected by energy errors, it is also of interest to measure the quality of the ideal dose distribution given by the treatment plan. In fact, the choice of such a measure will determine the implemented treatment plans, because they will be optimised with regard to the chosen measure. An important consideration during the choice of a quality measure for treatment plans is the robustness of the results against energy errors. For this study, two strategies have been evaluated.

The first and apparently most common treatment planning strategy is based on equidistant layers or layers spaced according to a well-defined function, e.g. where the distance between consecutive layers is chosen relative to their Bragg peak width (see 2.2.4.3). From a given set of layer positions one computes the weight, i.e. the relative intensity of each layer, such that the sum of the dose contributions forms a plateau. The algorithm used here chooses the weights such that the dose level at the local minima correspond to the intended dose level. This strategy is referred to as "weights planner" in the following.

The second treatment planning strategy evaluated here is based on optimisation of both, layer positions and weights. The algorithm is implemented as a minimisation of the surface dose with the optimisation constraint that the dose level within a specified target region must be equal or above an intended dose level. The choice of the surface dose as the objective function of the optimisation is an easy implementable measure for the exposure of healthy tissue surrounding the target. This strategy is referred to as "full planner" in the following. For practical reasons[2], only a certain number of energies is available to be chosen from.
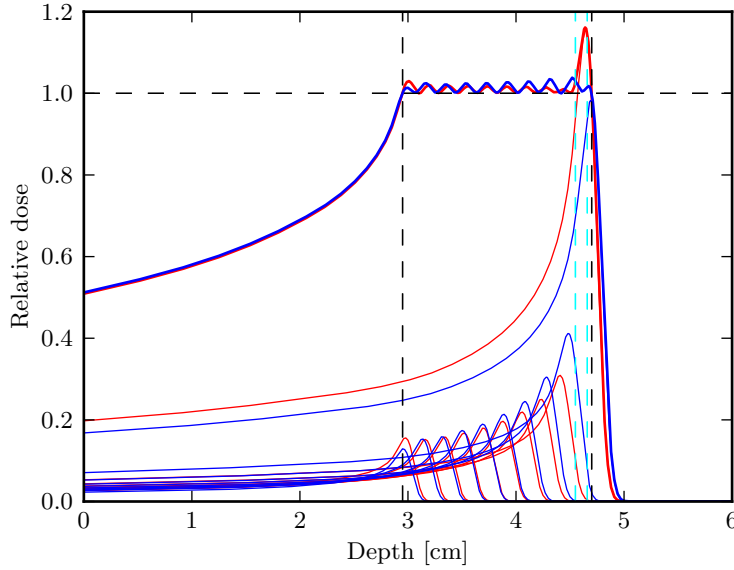
Figure 2.5.: Comparison of two treatment planning strategies for a target at depths between 2.95 and 4.7 cm (chosen corresponding to the lowest proton beam energy and 10 layers at a realistic layers density). The irradiation is done with proton beams between 60 and 77 MeV after passing through a ridge filter. The treatment plan generated by the weights planner is indicated by the solid blue line. The treatment plan generated by the full planner is indicated by the solid red line. For both plans, the thin lines indicate the 10 layers separately. The black dashed lines indicate the target region and the intended dose.

To illustrate the different treatment plans resulting from the two planning strategies (the weights planner used an equidistant spacing in this example), figure 2.5 shows the

---

[2]Only a discrete set of energies is available from the accelerator control system since energy dependent parameters - like magnetic field ramps - must be configured on a case-by-case, i.e. energy-by-energy basis. Also the irradiation duration should be limited and many energies would necessitate many spills.

result of both for the same target. The most obvious difference between the two ideal dose distributions is the relative emphasis of the last layer chosen by the full planner. At the second glance, the unsurprisingly slightly lower surface dose achieved by the full planner can be noticed.

Although the full planner performs better when looking at the ideal dose distribution, it turns out that the plans generated by the weights planner are more robust against energy errors. This can be explained with the lower influence of errors in the beam energy of the deepest layer. The treatment plans used for the benchmarks in this document have been generated by the weights planner.

2.2.4.3. Layer spacing

Due to multiple scattering, the Bragg peak width of high-energy particles is always larger than that of low-energy particles of the same type. Figure 2.6 demonstrates the effect of the varying peak width on a treatment plan if equal spacing of all layers is employed during treatment planning.
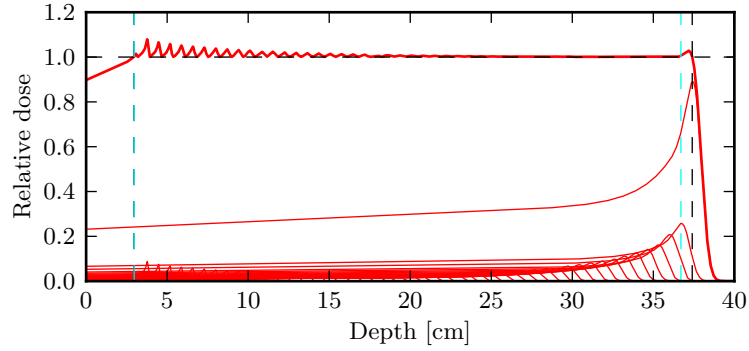
Figure 2.6.: Relative dose levels generated by a treatment plan containing 50 layers which covers a target between 3 and 37.4 cm (corresponding to proton beam energies from 60 to 250 MeV) with equidistant spacing.

An intuitive approach to compensate the decreased homogeneity in the distal region is, to adjust the layer spacing proportional to the width of the Bragg peak. The FWHM of the Bragg peak of protons in water is well approximated by a linear function of the particle range:

$$w_{\mathrm{FWHM}}(R) = kR + d = 0.085R + -0.035 \, \mathrm{cm} \tag{2.3}$$

where w is the Bragg peak FWHM width, and R is the particle range in water, both in centimetre. k and d are calibration factorswhich have been determined from the fitted Bragg peak model (see section 2.1.2). If R_0 and R_{N-1} are the intended ranges (in centimetres) of the first and last layer respectively corresponding to the target dimensions
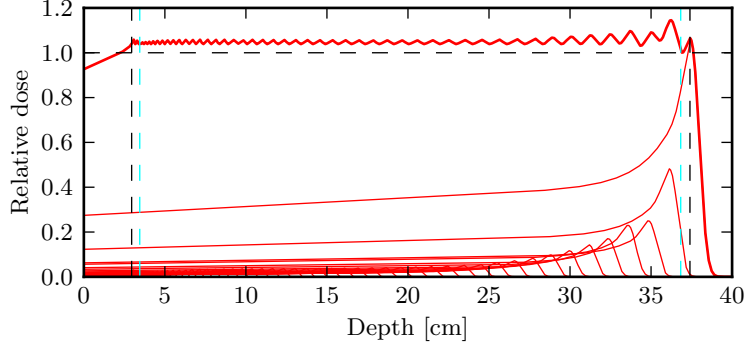
Figure 2.7.: Like figure 2.6, but with layer spacing adjusted proportional to the FWHM of the Bragg peak.
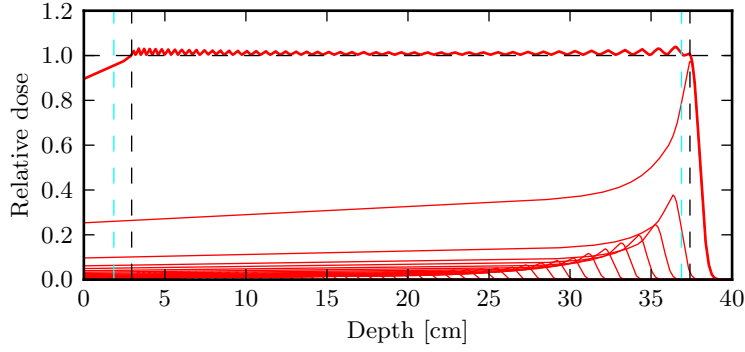
Figure 2.8.: Like figure 2.7, but with moderated adjustment.

and N is the number of layers, a spacing relative to the peak width w is achieved by the following ranges for the layers in between

$$R_i = R_0 + Di + K\frac{i(i+1)}{2} \tag{2.4}$$

where the constants K and D are defined as

$$K \equiv \frac{D_0}{\frac{N}{2} - 1}\left(\frac{w(R_{N-1}) - w(R_0)}{w(R_{N-1}) + w(R_0)}\right) \tag{2.5}$$

$$D \equiv D_0 - K\frac{N}{2} \tag{2.6}$$

and D_0 is the equidistant spacing without adjustment (i.e. when $K = 0$)

$$D_0 \equiv \frac{R_{N-1} - R_0}{N - 1} \tag{2.7}$$

Particle type	Ridge filter	Energy	Maximum acceptable error
Protons	Yes	60 MeV	±0.17 MeV
Protons	No	60 MeV	±0.14 MeV
Protons	No	250 MeV	±0.48 MeV
Carbon ions	Yes	120 MeV/n	±0.22 MeV/n
Carbon ions	Yes	400 MeV/n	±0.33 MeV/n

Table 2.1.: Maximum acceptable energy errors for protons and carbon ions at lowest and highest energy resulting from the minimum required cold spot dose.

Modifying the treatment plan shown in figure 2.6 according to equation (2.4) yields the treatment plan shown in figure 2.7. Unfortunately, this is no improvement but only a shift of the original problem of large unbalanced variations in the dose distribution to the other end of the stack. It is clear that the optimum is somewhere in between. The easiest way to moderate the above adjustment is by decreasing K, emulating a weaker increase of peak width with particle range. Figure 2.8 shows the result of a moderation of K to 64 % of it's original value ($K' = 0.64 \times K$). The treatment plans used to derive the energy precision requirements in section 2.3 employ this kind of moderation to maximise layer density at a given homogeneity.

2.3. Energy verification requirements

The acceptable energy errors can be derived from the minimum acceptable cold spot dose given in section 2.2.3. The acceptable errors are evaluated at minimum and maximum beam energy for proton and carbon ion beams. This is achieved by generating representative treatment plans using the weights planner described in section 2.2.4. All treatment plans have 10 layers. The width of target region and the layer spacing is then chosen such that the homogeneity (i.e. the relative dose variation) of the ideal (i.e. error-free) treatment plan is within 4 % after optimising the tweaking factor (see section 2.2.4.3) and the layer weights.

From the ideal treatment plan the worst-case cold spot dose is then obtained by evaluating the worst-case situation corresponding to a given energy and relative spread error. This worst-case situation corresponds to a simultaneous negative energy shift of all but the deepest layers and a positive energy shift of the deepest layer (see figure 2.9). Concerning the energy spread, it turns out, the worst-case situation is a simultaneous increase of the energy spread for all layers. Such a change in energy spread shifts the stack as a whole to a more shallow region, further deepening the gap generated by the worst-case energy shift. For high-energy beams (250 MeV proton beams or 400 MeV/n carbon beams), the sensitivity to energy spread errors within the regarded limits is negligible.

The principal source for energy spread errors is the term S/Q' in equation 2.2. At the same time, changes in this term translate into changes in the extracted intensity and the beam size. Compared to the intensity, the energy stacking is almost insensitive to such
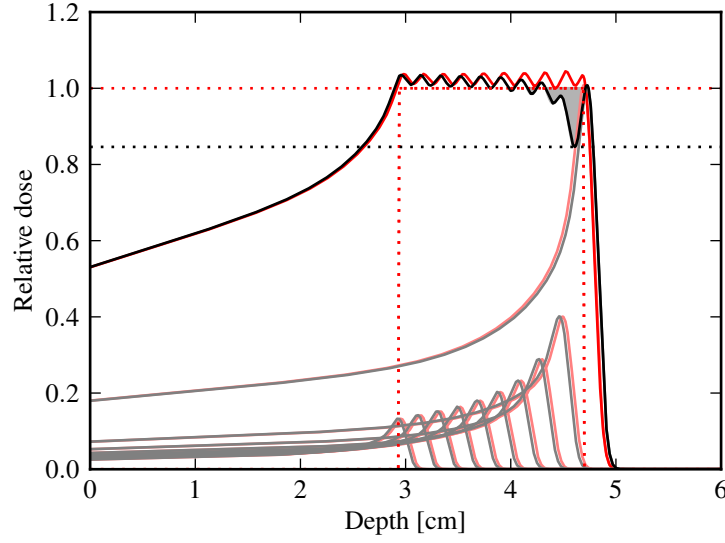
Figure 2.9.: Comparison of a dose distribution of a proton beam treatment using 10 layers with and without energy errors. The strong red line shows the treatment plan, i.e. the dose distribution without energy errors (the thin red lines indicate the layers). The strong black line shows the worst-case dose distribution with energy errors of $\pm 0.3\,\text{MeV}$. The worst-case situation is that the energy of the deepest layer is shifted by $+0.3\,\text{MeV}$ and the energies of all other layers are each shifted by $-0.3\,\text{MeV}$ (the thin black lines illustrate the shifts accordingly). In this case the cold spot (i.e. minimum) dose inside the target drops to $84.6\,\%$ of the intended dose level.

changes, because the influence of range straggling (i.e. the Bragg peak width) on the dose distribution covers the effects of energy spread errors that can happen within the acceptable spot weight errors [66], i.e. the spot weight errors are unacceptable long before the energy spread error are. To nevertheless account for them, a conservative maximum relative change of $1\,\%$ of S/Q' has been assumed, decreasing the maximum acceptable energy error between 4 and $10\,\%$ compared to zero energy spread error. Table 2.1 summarises the maximum acceptable energy errors for different particle types and energies under this assumption.

Summary The following list provides a summary of the energy verification requirements, combining the results of the above sections with the baseline parameters for medical operation at MedAustron [28]:

- For carbon ion beams used in combination with a ridge filter, beam energies (i.e. average particle energies) outside a limit between ±0.25 and $\pm0.37\,\mathrm{MeV/n}$, depending on the beam energy, must be rejected.

- For proton beams, beam energies outside a limit between ±0.14 and $\pm0.48\,\mathrm{MeV}$, depending on the beam energy and the use of an optional ridge filter, must be rejected.

- The verification must provide an accuracy of $\pm0.1\,\mathrm{MeV}$. This comes from patch field scanning, and not the energy stacking technique [60]: when employing patch field scanning, i.e. irradiation of the same target from different directions, the patches corresponding to the respective directions must align with a sub-millimeter precision.

- (either) Synchronous verification of the energy of the particles that are used for the treatment with similar speed as the position verification. In this case, the energy of the particles that reach the patient is verified continuously i.e. for each spot (minimum time at one spot is $200\,\mathrm{\mu s}$ [28]).

- (or) Qualification of the energy of the particles in the same spill as those used for the treatment within roughly $100\,\mathrm{ms}$ (within the beam qualification time, during which the beam is anyway dumped - see 4.1.1). In this case, the energy of the particles that reach the patient is not verified. Instead, other particles, which belong to the same cycle (same injection energy, same acceleration) and are therefore assumed to have the same energy as those that hit the patient, are used for the verification.

- The energy measurement must be applicable to all particle types used for medical treatment from protons to carbon ions.

- Reach the specified performance at lowest beam intensities of 10^8 particles per second ($16\,\mathrm{pA}$) for proton beams and 4×10^6 particles per second ($3.8\,\mathrm{pA}$) for carbon ion beams.

- Reliable measurement, read-out and decision taking (interlock condition) in order to avoid unnecessary beam dumps.

2.4. Measurement interpretation and decision taking

In general, the outcome expected from the energy *verification* is two-valued (OK or not OK) in contrast to an energy *measurement*. Appropriate methods to arrive at a two-valued outcome based on (many-valued) measurement data are provided in the framework of statistical hypothesis testing [76]. This section will first give a brief overview of the concept of hypothesis testing. Then, the two types of errors that must be considered when doing hypothesis testing will be formally defined and the required levels for both in case of energy verification will be derived.

2.4.1. Statistical hypothesis testing

In this context, a hypothesis is an assumption that can be tested. The test result either rejects the hypothesis or not. The tested hypothesis is called the null hypothesis[3]. In order for the null hypothesis to be testable, it must be formulated in terms of observable parameters. A test statistic must be chosen to summarise the data, i.e. the values of all observables, to a single numerical value. The choice of a test statistic must take into account statistical assumptions between the observables such as statistical independence. Finally, the distribution of the test statistic under the null hypothesis must be derived. From the resulting distribution, a critical region must be defined which includes those values of the test statistic that do not occur (or are very unlikely to happen) in cases that fulfill the null hypothesis. To test a given set of observations, the test is applied to the data and the null hypothesis is rejected whenever the test statistic is within the critical region. Otherwise the null hypothesis is assumed to be fulfilled.

In case of energy verification, the null hypothesis is that the beam energy is correct. The observables can be the outcome of any measurement that is related to the beam energy. Then the test statistic is the distance between the observed and the expected outcome (in general this distance has no physical equivalent). From the distribution of the test statistic observed for the correct beam energy, a maximum distance can be defined beyond which the observation is considered to disagree with the the null hypothesis i.e. to indicate an incorrect beam energy.[4]

Unless the distribution of the test statistic under the null hypothesis is the delta distribution, there is a certain probability that observables obtained under the null hypothesis yield a test value that still gets rejected because it exceeds the defined maximum distance. Additionally, unless the distribution of the test statistic under the null hypothesis is infinitely far apart from its distribution under an alternative hypothesis, there is also

---

[3]The opposite of the null hypothesis is called the alternative hypothesis. The alternative hypothesis is realised whenever the null hypothesis is rejected.

[4]This general procedure also applies to the time-of-flight measurement described in chapter 3, where the distance is simply defined as the energy offset and the maximum distance is some maximum energy difference beyond which the beam is rejected.

a certain probability that observables obtained under an alternative hypothesis yield a test value that does not get rejected because it is within the defined maximum distance (see 2.4.2 and 2.4.3). Figure 2.10 illustrates both effects for a Gaussian distribution.

2.4.2. Statistical significance

The significance of a test is the probability of "false positives" (type 1 errors) i.e. the probability that observations get rejected although they have been made under the null hypothesis. In the case of energy verification, that corresponds to the probability that a correct beam energy wrongly triggers a beam dump. Hence the statistical significance directly impacts the beam availability. Unfortunately it cannot be made arbitrarily small without degrading the statistical power of the test (see 2.4.3). The significance is therefore determined by the minimum beam availability after taking into account other events which also decrease the beam availability.

2.4.3. Statistical power

The power of a test determines the probability of "true positives" i.e. the probability that observations are rejected if they have been made under an alternative hypothesis. In the case of energy verification that corresponds to the probability that an incorrect beam energy is detected. Hence the statistical power directly corresponds to the risk reduction concerning the use of incorrect energies.

The statistical power is directly related to the probability β of "false negatives" (type 2 errors) i.e. the probability that observations are not rejected although they have been made under the alternative hypothesis:

$$\text{Power} = 1 - \beta \tag{2.8}$$

In case of energy verification, β corresponds to the probability that an incorrect energy remains undetected.

2.4.4. Required performance

For the significance, a requirement can be deduced from the acceptable decrease of beam availability and the measurement rate as given by the verification requirements (see 2.3). If one of 4000 medical cycles per day may be dumped erroneously, the required significance level is 2.5×10^{-4}. The benchmarks on which the design decisions in section 4.6 are based use a significance of 1×10^{-4}. At a verification rate of $1\,\text{kHz}$ and assuming a conservative average cycle time of $10\,\text{s}$, the required significance level is approximately $(4000 \times 10\,\text{s} \times 1000\,\text{Hz})^{-1} = 2.5 \times 10^{-8}$.

The power requirement is essentially given by the risk management process, which requires the risk reduction to be "as good as reasonably possible". Consequently the power should be as high as reasonably possible.
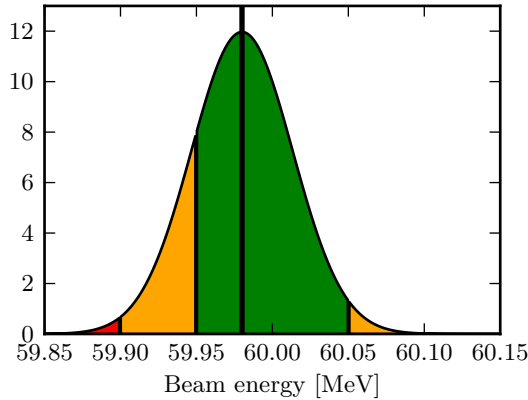
(a) A test result that does not get rejected. The measurement result is 59.98 MeV and the displayed Gaussian is the probability distribution of the unknown true value. The probability that the true value is outside ±0.1 MeV corresponds to the red area under the curve and equals 0.8 %.
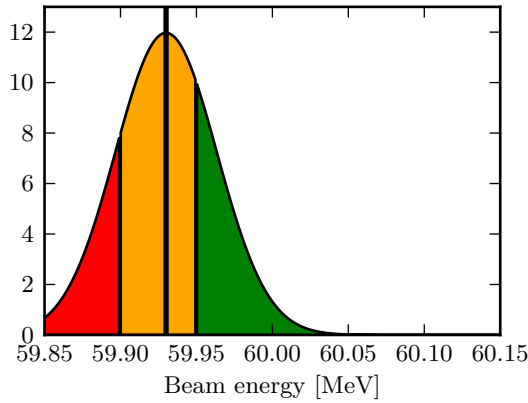
(b) A test result that does get rejected. The measurement result is 59.93 MeV, i.e. more than 0.05 MeV away from the ideal energy. Although the result is within ±0.1 MeV, the probability that the true value is outside this limit (which corresponds to the red area under the curve) is 18.4 %.

Figure 2.10.: Illustrations of positive and negative test results. For simplicity, the energy is used as test statistic. The ideal energy is 60 MeV and the energy limit is ±0.1 MeV (for acceptable energies). The RMS measurement precision is 0.033 MeV (one third of the limit), and the null hypothesis is rejected for test results outside of ±0.05 MeV from the ideal energy.

2.5. Beam generation

This section explains the steps in a cycle at MedAustron that are taken until the extraction starts. It must be noted that these steps depend on the employed extraction strategy. Therefore the steps described here are valid only for the betatron core driven 3rd order resonant extraction used at MedAustron. An understanding of these steps allows for a judgement on the validity of an energy measurement at any moment before the patient irradiation. In this document, "pre-verification" or qualification refers to a measurement that is done before the patient irradiation on a spill-to-spill basis. This is in contrast to measurements done in a synchronous manner during the treatment (synchronous verification) and to measurements done less frequently, e.g. on a daily basis (calibration). Depending on the moment in the spill at which the qualification measurement is done, its validity varies.

Figures 2.11a up to 2.12d show a simplified summary of all operations that manipulate the particle energies in the synchrotron before they enter the High Energy Beam Transfer line (HEBT). The diagrams are so-called Steinbach diagrams: the ordinate is the effective, normalised amplitude of the ion's horizontal betatron motion[5] and, for the purpose of showing the correlation between the two, the abscissa is a hybrid of the ion's energy and tune, where the origin of the tune axis is deliberately moved between the diagrams as explained below.

The beam is represented by a rectangle to show its spread in energy and amplitude via the horizontal and vertical dimensions of the rectangle respectively. The gradient of the rectangle in amplitude represents the amplitude density distribution of the particles in the beam. It is pointed out, that the maximum of that distribution is not at zero amplitude. This comes from the fact, that the covered phase space is proportional to the square of the amplitude.

The triangular shape indicated by blue lines represents an unstable region, meaning that particles which enter this region will leave the synchrotron after a certain number of revolutions. The bottom tip of the unstable region is marked by the resonance tune Q_{res}. Accordingly, the unstable region moves with the origin of the tune axis and the position of the resonance tune relative to the energy axis.

2.5.1. Injection & Acceleration

Injection This first step defines the initial energy and amplitude distribution of the particles in the synchrotron (see figure 2.11a). The markers on the ordinate axes indicate, that the beam energy at injection is $7\,\text{MeV}$ and the synchrotron lattice is configured such that particles of that energy have the nominal tune Q_{nominal}. For simplicity, the energy distribution of the particles is not detailed in the diagram, but a uniform distribution is assumed horizontally. In reality, the energy distribution is not uniform, but closer to a Gaussian shape.

---

[5]Explain betatron motion

(a) Injection (b) Ramp
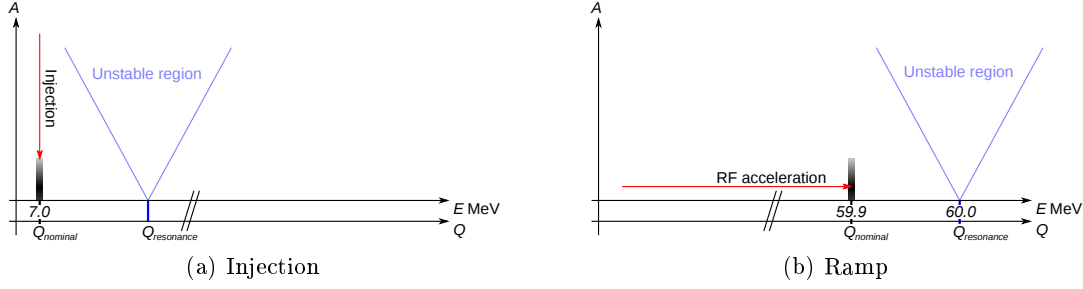
Figure 2.11.: Steinbach diagrams of injection and acceleration.

Ramp During the ramp, the particles are accelerated to an energy just below the intended extraction energy. In figure 2.11b, the extraction energy is chosen as 60 MeV and the beam energy at the end of the ramp is chosen as 59.9 MeV for illustrative purposes.

It is important to note, that the tune of the particles has not changed during the ramp i.e. it is intentionally kept constant. This is possible since the energy ramp or gain in the Radio Frequency; often refers to the Radio Frequency accelerating cavity (RF) cavity, which is responsible for the acceleration of the particles, is synchronised with the ramp of the synchrotron magnet strengths. (This fact is actually the origin of the word "synchrotron".) It is only just before the start of extraction that the tune is changed, as the tune during injection and ramp is kept at a save distance to a resonance.

2.5.2. Extraction

2.5.2.1. Particle energies before extraction

RF-Phasejump and De-bunching The RF-phasejump and the de-bunching serve several purposes at the same time:

- Increase the energy spread of the beam , i.e. the width of the energy distribution of the particles, to a value ΔE indicated in diagram 2.12a.

- Change the shape of the energy distribution of the particles to rectangular shape resembling a uniform distribution.

- As a side effect, the bunch structure of the beam is smoothened and the particles become uniformly distributed around the synchrotron.

Some details of this procedure are explained later in section 2.5.3.2. Here it suffices to know, that the only active element, i.e. the only element undergoing changes of settings, during de-bunching is the RF cavity.

Moving the beam towards resonance The ramp explained above increased the beam energy to a level located sufficiently lower than the extraction energy that even after the increase in energy spread during de-bunching, no particles enter the unstable region.

(a) De-bunching

(b) Moving towards the resonance

(c) Moving through the resonance
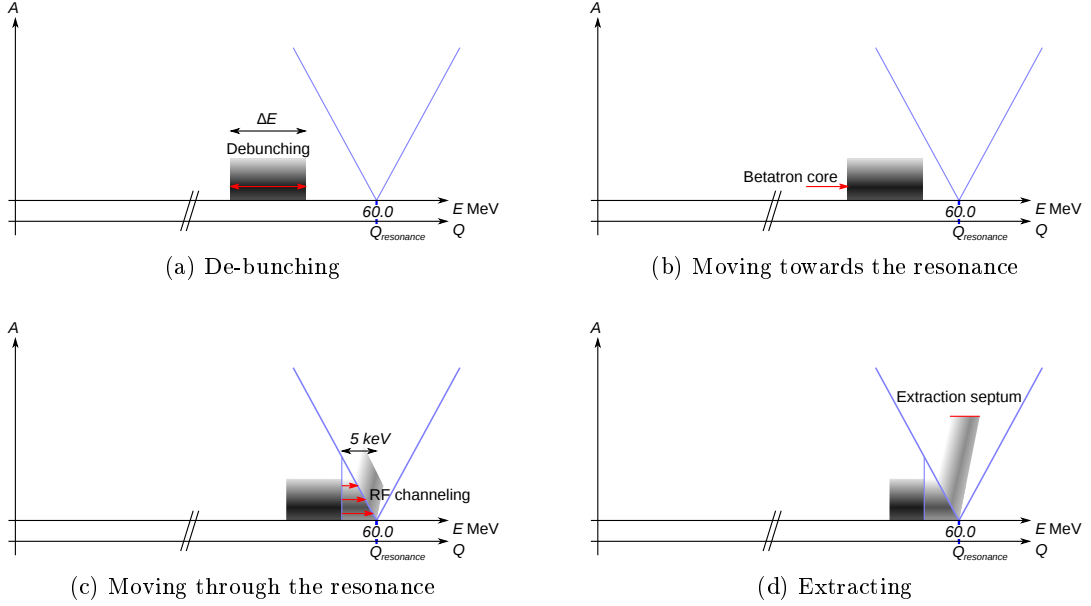
(d) Extracting

Figure 2.12.: Activities and active elements before the extraction of the ion beam

The acceleration stability or smoothness near the resonance has a significant impact on the stability of the intensity of the extracted beam. The betatron core, which is a special magnet specifically designed for that purpose, achieves a very smooth and well controlled acceleration of the beam, because it is almost unaffected by (high-frequency) power ripples.

It is important to note, that in contrast to the behaviour during the ramp, this time the lattice configuration remains constant. Therefore, the position of the resonance tune $Q_{resonance}$ in diagram 2.12b does not move relative to the energy axis and the extraction energy remains in place as well. Consequently the acceleration of the particles by the betatron core changes not only their energy, but also their tune and moves them towards the unstable region.

Together with the energy spread induced by the de-bunching, the speed of that movement, i.e. the magnitude of the acceleration induced by the betatron core, defines the duration of the extraction of the spill.

Moving the beam into the resonance & RF-Channeling   As an option, in order to further smoothen the intensity of the extracted beam, another mechanism called RF channelling can be used as the particles are approaching the unstable region. RF channelling is a special mode of operation of the RF cavity, where the frequency is intentionally offset from the beam revolution frequency. As indicated in diagram 2.12c, it typically starts 5 keV below the extraction energy. The effect of RF channelling is an additional acceleration of those particles that are just about to enter the unstable region. In the

diagram, this effect is indicated by a lower overall particle density above the threshold for RF channelling, because the particles traverse this last distance on the energy axis faster than if they were only affected by the (still active) betatron core.

The purpose of RF channelling is to decrease the sensitivity of the intensity of the extracted beam to tune ripple, i.e. small changes of the resonance tune. The additional acceleration increases the speed of the tune change $\dot{Q}$ to which the extracted intensity is proportional. At the same time tune changes due to tune ripple $\dot{Q}_{\mathrm{ripple}}$ are not affected by the accleration. Consequently the relative importance $\dot{Q}_{\mathrm{ripple}}/\dot{Q}$ and thus the influence of tune ripple on the extracted intensity is decreased. As with the de-bunching, again it suffices to know, that the active elements, during RF channelling are the betatron core and the RF cavity.

As soon as a particle enters the unstable region, its amplitude eventually starts to grow. In the diagram, this is indicated by the "refraction" of the beam at the border of the unstable region [20].

Extracting   The previous steps all served the purpose of moving the particles into the unstable region at a selectable speed and as smoothly as possible. The actual moment at which a particle leaves the synchrotron is defined by the extraction condition. This condition is determined by the first elements of the HEBT, the extraction septa, because they define the amplitude at which particles are branched off into the extraction channel[6].

In diagram 2.12d, the extraction condition is indicated by a line at a certain amplitude value. As soon as the amplitude of a particle grows beyond that line, it enters the extraction septa and the HEBT.

Although not separately indicated in the diagram, the betatron core and the RF cavity of course remain active until the entire beam is extracted.

2.5.2.2. Extraction energy

In the above explanations, the use of the term "extraction energy" has been used with care and sometimes the term "intended extraction energy" has been favoured. This choice was made to emphasize the potential difference between the two. Apart from that, a thorough understanding of the energies of the extracted particles must include more properties of their distribution than only the mean value.

As can be already understood from the above explanations, this distribution basically depends on the following parameters (in order of relevance):

1. The *position of the unstable region and the resonance tune on the energy axis*, governed by the synchrotron lattice configuration. Any change in the lattice translates into an energy shift of the extracted particles.

---

[6]In practice, the influence of the septa positions on the moment of extraction is negligible (in the order of microseconds, i.e. single turns), while the impact on the extracted beam size is much more important.

2. The *slope of the unstable region* also depends on the synchrotron lattice configuration. Changes translate into a change in scale of the energy distribution of the extracted particles.

3. The *amplitude distribution of the particles*, which is mostly defined by the injection and defines the shape of the energy distribution of the extracted particles.

4. The *extraction condition* is defined by the transverse position of the electric extraction septum. In principle, changes translate into an energy shift of the extracted particles, but in practice such changes are negligible (the influence of changes on the beam size are far more important).

2.5.2.3. Error scenarios

A pre-verification of the beam energy must ensure, that none of the parameters listed in section 2.5.2.2 is incorrect and that they do not change between the measurement and the extraction. This section explains possibilities to implement such checks. Detailed study of the feasibility of any of these methods is required prior to a decision to trust them.

Betatron hub Assuming a pre-verification of the bunched beam and knowledge of the ramp rate of the betatron core, the (actual) extraction energy could be deduced from a measurement of the ramp time and rate before the first extracted particle (see section 2.5.3.3).

Intensity change If one assumes pre-verification of the extracted beam in an alternative beam path (e.g. the chopper dump) or a combined pre-verification at the start of the extraction as described above, a shift of the resonance tune would not only result in an energy shift, but also in a temporary intensity change. Therefore an energy change subsequent to the pre-verification could be detected with a continuous measurement of the extracted beam intensity. Unfortunately there are other factors that influence the extracted beam intensity (e.g. the momentum distribution of the stored beam). Consequently in practice it may be very difficult or impossbile to separate those other factors.

2.5.3. Energy budget

The term "energy budget" expresses the fact that - when using qualification - the information about the energy of particles that impinge on the patient is not obtained by direct measurement. Instead the assumed energy of these particles is a prediction based on a measurement that is performed prior to the patient irradiation. This prediction is essentially a sum of all possible influences on the particle energy between the measurement and the irradiation. Unfortunately, it is difficult to verify the extraction condition (i.e. the resonant tune) with sufficient accuracy and precision. Therefore it is necessary to account for time-dependent influences also during the treatment.
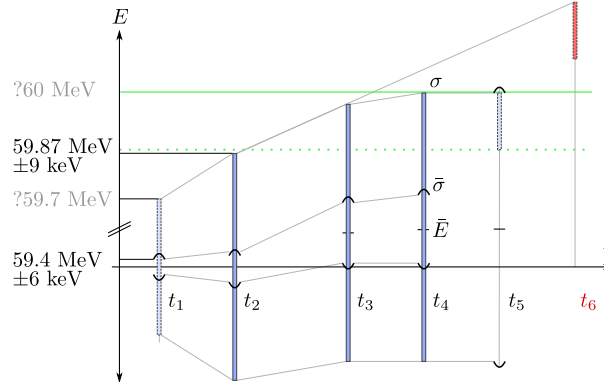
Figure 2.13.: The development of information on the energy distribution over time. The bars indicate the energy spread at a certain point in time. The centers of the bars indicate the expectation value and the brackets around the center indicate the uncertainty of the expectation value. The steps corresponding to each moment t_i are listed in table 2.2.

Figure 2.13 illustrates the possible influences on the particle energy by showing in a qualitative fashion the impact they have on the knowledge of the energy distribution properties. Those properties are the mean energy $\bar{E}$, the standard deviation of the mean $\bar{\sigma}$ and the energy spread expressed by the standard deviation of the energy distribution σ. The following subsections discuss the properties at each point in time where the properties are written with the index of the time marker (i.e. $\bar{E}_1$). Table 2.2 contains the definitions for the timer markers $t_{1\ldots5}$.

Marker	Time related to influences
t_1	Energy measurement in the synchrotron (see section 2.5.3.1)
t_2	After RF phase jump and de-bunching; before the betatron core is activated (see section 2.5.3.2)
t_3	After the betatron core has been enabled for some time; before the RF channelling is coming into effect (see section 2.5.3.3)
t_4	At the start of extraction (properties of the waiting beam)
t_5	At the patient (properties of the extracted beam)
t_6	Potential error scenario where the resonant tune is displaced

Table 2.2.: Description of the time markers in figure 2.13.

Figure 2.14 illustrates the steps of the slow extraction procedure in longitudinal energy-space. The following subsections discuss the influences of each indicated step on the energy and shall give an idea of the information loss concerning the particle energy distribution for each of the stages.
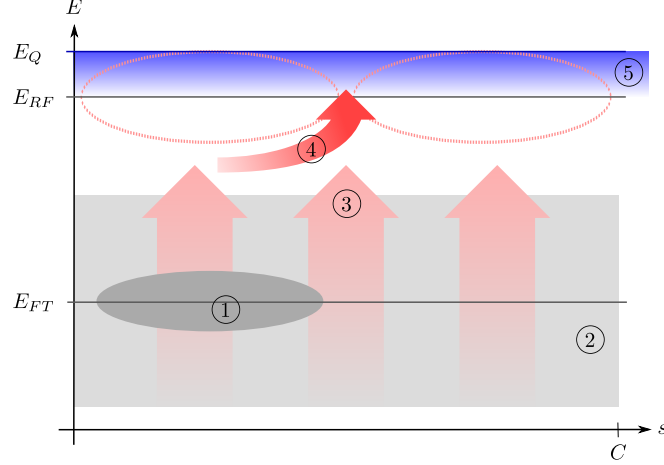
Figure 2.14.: Steps of the slow extraction procedure in longitudinal energy-space. The abscissa is the longitudinal coordinate s of the reference orbit in the synchrotron. The ordinate is the kinetic particle energy E_k. An area in the diagram corresponds to a distribution in the two coordinates, e.g. the beam. The upper limit of s is the synchrotron circumference C. Before the de-bunching, the particles are accelerated until the beam energy is E_{FT} (the flat-top energy). The bunched beam is indicated by the dark grey area 1. The light grey area 2 indicates the de-bunched beam. After de-bunching, the betatron core acceleration 3 homogeneously increases the energy of all particles. When RF channelling is used, the RF cavity is powered at a frequency that corresponds to a particle energy E_{RF}. When particles approach the RF bucket separatrix, they get accelerated along it, indicated by 4. Because of the small channel between two adjacent buckets through which the particles get accelerated, this is called RF channelling. Depending on their transverse amplitude, the particles get extracted at a certain point within the extraction band 5. High-amplitude particles get extracted already at E_{RF} while the lowest-amplitude particles only get extracted at the resonant energy E_Q.
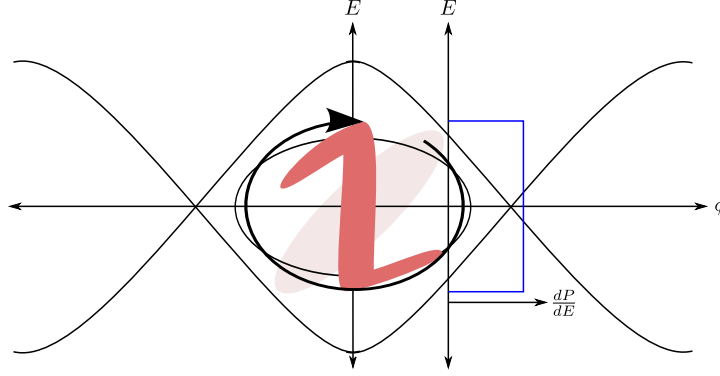
Figure 2.15.: Filamentation and energy distribution after both RF phase jumps.

2.5.3.1. Measurement

The time-of-flight measurement (see chapter 3) is done after the acceleration ramp (beginning of the "flat-top") when the beam is still bunched. The width of the energy distribution ("energy spread") is not known as the Schottky noise measurement works well enough only for unbunched beams and therefore has to performed at a later stage.

The knowledge of the energy distribution after this first measurement is characterised by the following properties:

$$\bar{E}_1 = E_{\text{ToF}} \tag{2.9}$$

$$\bar{\sigma}_1 = \sigma_{\text{ToF}} \tag{2.10}$$

$$\sigma_1 < \sigma_{\text{stable}} \tag{2.11}$$

where E_{ToF} is the measurement outcome, σ_{ToF} is the precision of the energy measurement (see the middle column of table 3.6). The energy spread remains unknown, although it is limited by the dispersion function together with the finite aperture of the machine to be below a certain value represented by σ_{stable}.

2.5.3.2. RF-Phasejump and De-bunching

The de-bunching consists of a few steps: First, an RF phase jump of 180 degree causes the energy distribution to widen. After another phase jump back to the original phase, the filamentation indicated in figure 2.15 by the Z-shaped phase-space area leads to an approximately uniform energy distribution. Finally the RF is turned off and the beam distributes equally in longitudinal direction (i.e. around the synchrotron ring).

The frequency of the RF voltage is regulated to match the mean particle energy after acceleration. An offset in the actual frequency within certain limits results in a shift of the mean energy. Therefore it is important to measure the frequency of the applied voltage separately. The uncertainty of this measurement adds to the uncertainty of the mean energy.

Alternatively to a time-of-flight measurement before the de-bunching (section 2.5.3.1), it can be performed after the second phase-jump of the RF cavity and before the RF voltage is turned off. That way, the uncertainty of the mean energy is not increased during de-bunching, but the available time may be too short to achieve the required bunch revolution frequency precision.

The intentionally introduced energy spread depends on the amount of time between the two RF phase jumps and the RF voltage. It can be verified with a Schottky noise measurement as described in section 3.5. For the standard deviation of the energy distribution, the precision of the Schottky noise measurement is added to the measurement result to get a conservative approximation of the upper energy limit.

The knowledge of the energy distribution of the de-bunched beam is characterised by the following properties:

$$\bar{E}_2 = \bar{E}_1 \tag{2.12}$$

$$\bar{\sigma}_2^2 = \bar{\sigma}_1^2 + \sigma_{\mathrm{RF}}^2 \tag{2.13}$$

$$\Delta E_2 = \Delta E_{\mathrm{Schottky}} + \sigma_{\mathrm{Schottky}} \tag{2.14}$$

where σ_{RF} is the uncertainty related to the measurement of the applied voltage frequency ("RF verification"), $\Delta E_{\mathrm{Schottky}}$ is the energy spread measured by the Schottky noise measurement and $\sigma_{\mathrm{Schottky}}$ is the uncertainty of the Schottky noise measurement. In contrast to the σ in equation (2.11), here the notation ΔE is preferred because the shape of the energy distribution changed from a normal to a uniform distribution.

The knowledge of the mean energy does not change, but the uncertainty of the RF verification adds to its uncertainty if the time-of-flight measurement is performed before the de-bunching. An upper limit of the energy spread is given by the result of the Schottky noise measurement plus the uncertainty of that measurement.

2.5.3.3. Betatron core acceleration

The acceleration by the betatron core increases the energy of all particles equally and therefore changes the mean particle energy, but leaves the energy spread constant. On the other hand, the uncertainty of the applied field strength ramp rate adds to the uncertainty of the mean particle energy.

The amount of added energy depends on the magnetic flux change rate in the core. This rate can be verified by continuous current monitoring or with an additional "sensing" coil through the betatron core. The uncertainty of that measurement integrated over the duration of betatron core acceleration adds to the mean energy uncertainty.

The knowledge of the energy distribution during betatron core acceleration is characterised by the following properties:

$$\bar{E}_3 = \bar{E}_2 + \Delta E_{\text{core}}(t) \qquad (2.15)$$

$$\bar{\sigma}_3^2 = \bar{\sigma}_2^2 + \sigma_{\text{core}}(t)^2 \qquad (2.16)$$

$$\Delta E_3 = \Delta E_2 \qquad (2.17)$$

where $E_{\text{core}}(t)$ is the mean energy increase according to the betatron acceleration and $\sigma_{\text{core}}(t)$ is the uncertainty of the betatron acceleration:

$$\Delta E_{\text{core}}(t) = \frac{1}{C_0 B\rho} \frac{L}{N} \frac{\gamma + 1}{\gamma} E_k \left[i(t) - i(t_2) \right] \qquad (2.18)$$

$$\sigma_{\text{core}}(t) = \frac{1}{C_0 B\rho} \frac{L}{N} \frac{\gamma + 1}{\gamma} E_k 2\sigma_i \qquad (2.19)$$

where C_0 is the circumference of the reference orbit, $B\rho$ is the magnetic rigidity of the particles, L is the inductance of the coils and N is the number of coils of the betatron core.

The numbers for the Proton-Ion Medical Machine Study (PIMMS) betatron core [15] are $N = 10$ and $L_{\text{max}} = 0.43\,\text{H}$. At MedAustron, the central orbit circumference is $C_0 = 77.648\,\text{m}$. For high-energy protons ($E_k = 250\,\text{MeV}$, $B\rho = 2.43\,\text{Tm}$, $\gamma = 1.27$), the above equations turn into

$$\Delta E_{\text{core}}(t) = 0.10 \left[i(t) - i(t_2) \right] \qquad (2.20)$$

$$\sigma_{\text{core}}(t) = 0.20\sigma_i \qquad (2.21)$$

In summary, the expected mean energy increases according to the betatron core acceleration and the uncertainty of the betatron core acceleration adds to the mean energy uncertainty. Because all particles are subject to the same field inside the betatron core, the energy spread is not changed during betatron core acceleration.

2.5.3.4. RF channelling

The influence of RF channelling depends on the frequency and the amplitude of the voltage applied to the cavity. Ideally, the frequency corresponds to the resonance energy of the particles with maximum betatron amplitude. Because prior to extraction the beam has an energy below the resonance energy, the RF field creates empty buckets in longitudinal phase space. Particles of an energy well below the resonance energy are outside the bucket structure and their energy is not affected.

Only when a particle approaches the empty bucket energy, it enters a "bottle neck" created by the separatrices between two empty buckets (see figure 2.14). Inside this bottle neck, the particle receives additional acceleration. This results in a lowered density of particles in that region, because they get "pushed out" towards the resonance faster than by the betatron core acceleration alone. These particles are said to be "in the channel".

When the RF frequency and voltage are well aligned with the resonance, the particles entering the channel are extracted within a few hundred turns. In time this corresponds to a value in the order of one millisecond and is therefore approximated to happen instantaneously for the purpose of the energy budget. It is assumed that the energy of a particle that enters the channel is immediately increased by an unknown value within the channel where it is extracted.

When RF channelling is used, it is therefore *impossible to derive the particle energy* at the resonance based on the moment of extraction better than the energy spread (height in longitudinal phase space) of the empty bucket. Unfortunately, the energy spread is higher than the required energy verification precision.

2.5.3.5. High-energy beam transport

Between the moment where a particle enters the extraction line and the moment where it enters the patient's body, there are a few influences on the particle energy:

- Redundant detectors for beam position, intensity and profile

- An optional ridge filter (see section 2.2.1)

- At least one vacuum window

- Possibly gas in (parts of) the treatment line

- Air between the nozzle and the patient

Since these influences can be assumed to have a reproducible effect on the particle energy, they can be accounted for during commissioning and calibration. Nevertheless, the uncertainty they introduce has to be studied using precise specifications (material and amount thereof).

2.5.3.6. Résumé

Because it would render any predictions impossible, it is assumed for the following summary, that the RF channelling mechanism is not employed. If the uncertainties mentioned in section 2.5.3.5 are neglected and it is assumed that the time-of-flight measurement is performed at the final stage of the de-bunching, i.e. just before the RF is turned off, the knowledge of the energy distribution of the particles that impinge on the patient is characterised by the following properties:

$$\bar{E}_{\text{total}}(t) = E_{\text{ToF}} + \Delta E_{\text{core}}(t) \tag{2.22}$$

$$\bar{\sigma}_{\text{total}}(t)^2 = \sigma_{\text{ToF}}^2 + \sigma_{\text{core}}(t)^2 \tag{2.23}$$

$$\Delta E_{\text{total}} = \Delta E_{\text{Schottky}} + \sigma_{\text{Schottky}} \tag{2.24}$$

When the extraction starts, the first part of the spill will be dumped in a qualification monitor which will, among other properties, measure the intensity of the extracted beam.
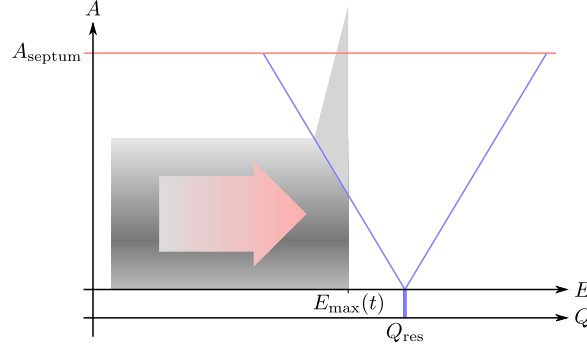
Figure 2.16.: This Steinbach diagram illustrates schematically why the particle flow rate ("intensity") of extracted particles increases during the first stage of extraction. E is the particle energy, Q is the particle tune, A is the normalised amplitude in the horizontal phase-space, Q_{res} is the resonant tune which is a function of the particle amplitude and A_{septum} indicates the extraction condition by the extraction septum. The grey levels schematically indicate particle density. The region inside the triangle formed by the resonance conditions is called the unstable region.

As indicated in figure 2.16, the first extracted particles will be high-amplitude particles, because they enter the unstable region first and subsequently cross the extraction condition applied by the extraction septum first. After the first particles got extracted, there will be an intensity ramp-up until finally the zero-amplitude particles reach their resonant tune Q_{res}.

To derive the position of the resonance condition $Q_{\mathrm{res}}(E)$, which determines the energy of the extracted particles, the temporal development of the intensity ramp must be compared with the energies of the highest-energy particles which have an energy of

$$E_{\max}(t) = \bar{E}_{\mathrm{total}}(t) + \Delta E_{\mathrm{total}} \tag{2.25}$$

To connect the resonance condition with the particle energies as in diagram 2.16, also the distribution of the normalised amplitudes A must be known. If the amplitude distribution is not known, the point in time where the intensity becomes stable can be assumed equivalent to the time when also the lowest-amplitude particles get extracted. The value of $E_{\max}(t)$ at this time corresponds to the extraction energy for a zero-amplitude particle.

2.6. Analysis of measurement methods

There are two principal options to verify the energy of the ions in the beam:

- Direct energy measurement by absorption of the particle

- Indirect energy measurement, e.g. momentum or velocity measurement, where the measured quantity is proportional to the energy with assumed knowledge of the

      particle mass/type

The direct measurement is destructive, i.e. it cannot be done in a synchronous manner during the treatment itself, except if it is done in a sampling manner leaving the bigger part of the beam alone. The momentum measurement is non-destructive and influences the beam only to a very small degree, depending on the type of instruments involved.

    In the following sub-sections, direct and indirect energy measurements will be briefly discussed and their performance in terms of energy precision will be evaluated.

2.6.1. Spectrometer

2.6.1.1. Measurement principle

A spectrometer measurement is based on the deflection of moving charges in a magnetic field. It is a non-destructive measurement. Depending on the magnetic field level and the charge and momentum of the particle, the deflection angle varies. Using measurements of the magnetic field and the deflection angle and assuming the particle charge and mass, the momentum and the particle energy can be computed. Instead of deflection angle measurements, also a set of collimations can be used, that allows only particles of the desired energy to pass, effectively acting as an energy filter.

    The measurement is a momentum measurement based on the following relation

$$p = \frac{BLq}{\theta} \tag{2.26}$$

    where p is the particle momentum, B the magnetic field, L is the length of the dipole (more precisely: the arc length of the particle's path inside the magnetic field), q is the particle charge and θ is the deflection angle.

Performance   Uncertainties in the determination of the dipole length are deliberately ignored and the charge is naturally constant. The propagation of relative uncertainties follows as

$$\left(\frac{\Delta p}{p}\right)^2 = \left(\frac{\Delta B}{B}\right)^2 + \left(\frac{\Delta \theta}{\theta}\right)^2 \tag{2.27}$$

Relating the momentum to the kinetic energy by

$$E_k = \sqrt{(pc)^2 + E_0^2} - E_0 \tag{2.28}$$

where c is the speed of light and $E_0 = m_0 c^2$ is the mass-equivalent energy, results in the following propagation of uncertainty

$$\frac{\Delta E_k}{E_k} = \frac{\gamma + 1}{\gamma} \left| \frac{\Delta p}{p} \right| \tag{2.29}$$

where γ is the relativistic Lorentz factor, and E_k is the kinetic energy of the particle. It follows

$$\frac{\Delta E_k}{E_k} = \frac{\gamma + 1}{\gamma} \sqrt{\left(\frac{\Delta B}{B}\right)^2 + \left(\frac{\Delta \theta}{\theta}\right)^2} \tag{2.30}$$

Particle type	Particle energy	B	ΔB_{max}
Proton	$60\,\text{MeV}$	$0.27\,\text{T}$	$0.2\,\text{mT}$
Proton	$250\,\text{MeV}$	$0.57\,\text{T}$	$0.4\,\text{mT}$
Carbon ion	$120\,\text{MeV}/\text{n}$	$0.76\,\text{T}$	$0.3\,\text{mT}$
Carbon ion	$400\,\text{MeV}/\text{n}$	$1.49\,\text{T}$	$0.3\,\text{mT}$

Table 2.3.: Accuracy requirements for a measurement of the magnetic field of a bending dipole for low and high particle energies. At a perfect deflection angle, the given ΔB_{max} corresponds to an energy deviation equal to the required energy precision given in section 2.3.

As can be seen from table 2.3, the most demanding case for the measurement of the magnetic field is a low energy ($60\,\text{MeV}$) proton beam. For the deflection angle measurement, the most demanding case is the high energy ($400\,\text{MeV}/\text{n}$) carbon beam because it has the largest β. The assumed dipole length is $L = 1.6772\,\text{m}$ and the deflection angle is $\theta = 22.5\,°$. From these two cases and by equally sharing the required relative accuracies among both measurements follows:

$$\Delta B \leqslant 0.16\,\text{mT} \tag{2.31}$$
$$\Delta \theta \leqslant 10.1\,'' \tag{2.32}$$

To measure the deflection angle, four position measurements are necessary. The required precision of those measurements depends on their location relative to each other.

General advantages

- Non-destructive measurement

- Independent of beam intensity (above a minimum threshold for the beam position measurements)

- Very few elementary measurements are needed: in case of collimation, only the field probe, otherwise the field probe plus four beam position measurements

General drawbacks and challenges

- All dipole fields along the angle measurement (e.g. also correctors) have to be taken into account

- Multiple high-precision beam position measurements (or collimators) are necessary

- Indirect measurement (implicitly assumes the particle mass/type)

2.6.1.2. Synchrotron as spectrometer

The synchrotron can be used as a spectromenter by measuring the magnetic dipole field in the synchrotron. The main drawback of this measurement is, that to achieve the required energy verification precision, the dipole field integrated over the entire orbit has to be known within about 0.1 mT. This means, that the influence of the corrector dipoles must not be neglected. Additionally, the necessary beam position measurements can only be performed as long as the beam is bunched. Therefore, this measurement can only be used for verification of the bunched beam.

Specific advantages

- Measurement of the reference dipole is for free (i.e. done anyway)

- Good precision of the deflection angle due to the large lever arm (several orbit circumferences)

Specific challenges and drawbacks

- All corrector dipole fields need to be measured and taken into account

- Only applicable for pre-verification (beam position monitors need bunched beam)

2.6.1.3. Transfer line as spectrometer

Another option is to measure the magnetic field in one or more of the beam transfer line dipoles or the scanner dipoles. Together with information on the beam angle obtained by multiple collimations or measurements the beam energy can be calculated.

The main drawback here is the difficulty of the beam position measurement. Because of the necessary precision , collimation is only an option at focal points and it becomes difficult for changing beam sizes. For the four beam position measurements needed (see section 2.6.1.1), only non-perturbing instruments can be used. The precision requirement depends on the distance from each other. Assuming 4 m distance between the detectors on each side of a main dipole leads to a required precision of the beam positions measurements of ± 0.11 mm.

PSI Villigen At the Paul Scherrer Institut (PSI), the beam energy is measured with Hall probes in one magnet of the beam line and in the 90 ° bending dipole of the gantry [67]. Daily depth-dose measurements check the performance of the machine and the relation to the magnetic field measurements.

The beam position information necessary to derive the energy from magnetic field measurements is obtained by the beam position measurement in the nozzle and by collimators at focal points in the upstream parts of the beam line [59]. This information somehow contradicts the fact that the value of the dispersion function, as plotted in Pedroni et al. [67, figure 8-4], is approximately zero and beam energy offsets should not be visible to the nozzle position monitors.

In practice, the beam energy does not have to be computed, but interlock conditions can be set directly on Hall probe and beam position measurements to stay within certain limits.

- Precision: n/a (Gantry 1 Hall probe: $\pm 2 \, \text{mT}$)

MDACC Houston   A Hall probe field measurement in the final bending magnet of the gantry triggers an interlock upon a field deviation above $6 \, \text{mT}$, which corresponds to approximately $1.4 \, \text{MeV}$ particle energy deviation [39]. The results of the acceptance tests, which included all 94 energies commissioned for medical purpose, have been compared to the results obtained during clinical commissioning, where 11 out of 94 energies have been measured. The comparison showed an agreement in range within $1 \, \text{mm}$.

- Precision: $\pm 1.4 \, \text{MeV}$

Specific advantages

- Magnetic field measurement of transfer line or gantry dipoles is common practice

- Verification synchronous with the treatment

Specific challenges and drawbacks

- Precision requirements for the necessary beam position measurement are tight and difficult to meet

2.6.2. Time-of-flight

2.6.2.1. Measurement principle

Since the particles at the foreseen energies are still significantly below the speed of light, a measurement of the particle velocity allows for the deduction of momentum and energy. Again the measurement is effectively a momentum measurement based on the relation between the particle momentum p and the velocity v:

$$p = m_0 \gamma v \qquad (2.33)$$

where m_0 is the rest-mass of the particle and γ is the relativistic Lorentz factor.

Performance   The relative uncertainty of the particle momentum is:

$$\left| \frac{\Delta p}{p} \right| = \gamma^2 \left| \frac{\Delta v}{v} \right| \qquad (2.34)$$

Using the velocity $v = 2\pi r f$ with the circle radius r and the revolution frequency f and relation (2.29) gives

$$\frac{\Delta E_k}{E_k} = \gamma(\gamma + 1)\sqrt{\left(\frac{\Delta f}{f}\right)^2 + \left(\frac{\Delta r}{r}\right)^2} \tag{2.35}$$

To provide an example, the numbers for a Carbon ion beam at $400\,\text{MeV/n}$, which is the most demanding case, are put in. The required energy precision is taken from table 2.3. The circumference of the reference orbit is $C = 77.648\,\text{m}$ and the revolution frequency is $f = 2.76\,\text{MHz}$. This results in the following requirement

$$0.0003 \geqslant 3.5\sqrt{\left(\frac{\Delta f}{2.76\,\text{MHz}}\right)^2 + \left(\frac{\Delta C}{77.648\,\text{m}}\right)^2} \tag{2.36}$$

Equally distributing the demanded maximum uncertainty on the measurements of the revolution frequency and the circumference leads to the following requirements

$$\Delta f \leqslant 170\,\text{Hz} \tag{2.37}$$

$$\Delta C \leqslant 4.7\,\text{mm} \tag{2.38}$$

In the case that the revolution frequency can be determined precisely, this results in the following requirements

$$\Delta f \approx 0\,\text{Hz} \tag{2.39}$$

$$\Delta C \leqslant 6.7\,\text{mm} \tag{2.40}$$

The closed orbit circumference can not be measured directly, but has to be computed from beam position measurements distributed over the synchrotron. The relation between the above requirement and the beam position measurements is described in section 3.2.4.

If the time of flight is not computed from the revolution frequency but measured directly, assuming a drift distance of $10\,\text{m}$ and once more the most demanding case of a high energy $(400\,\text{MeV/n})$ carbon beam, equation (2.35) becomes

$$0.0003 \geqslant 3.5\sqrt{\left(\frac{\Delta t}{47\,\text{ns}}\right)^2 + \left(\frac{\Delta d}{10\,\text{m}}\right)^2} \tag{2.41}$$

Again distributing the demanded maximum uncertainty between the time measurement and the distance information results in the following requirements

$$\Delta t \leqslant 2.9\,\text{ps} \tag{2.42}$$

$$\Delta d \leqslant 0.6\,\text{mm} \tag{2.43}$$

General advantages

- Non-destructive measurement

- Independent of beam intensity (above a minimum threshold)

General drawbacks and challenges

- Indirect measurement (implicitly assumes the particle mass/type)

2.6.2.2. Revolution period

The revolution time can be measured either by pick-up instruments or by evaluating the frequency used by the RF cavity. The orbit circumference must be computed from beam position measurements and orbit excursions must be considered.

The main drawback here is, that the circumference of the beam orbit must be known precisely. The limited number of measurements make assumptions about the orbit between them necessary. Together with the precision of the measurements, this is the main limiting factor for the achievable energy verification precision. Chapter (3) contains a detailed analysis of the performance that is theoretically achievable at MedAustron or a similar machine.

LLUPTF Loma Linda The beam energy monitoring system [60] uses eight Beam Position Monitors (BPMs), two of which are connected to revolution frequency counters. The beam position readings are obtained "averaging-by-eye" with an estimated uncertainty of ± 0.05 mm (which must be seen relative to the effective radius of about 3.2 m). The two revolution frequency measurements are compared with an accepted tolerance of 50 Hz. The frequency observed during repeated measurements on separate days was identical to within $\pm$ 1 kHz.

For determination of the nominal orbit radius, a custom water scanner detector is used to measure the depth-dose and obtain the beam range. The beam energy is then derived from range-energy tables [47]. The average difference between the energies reported by the beam energy monitoring system and those measured with the water scanner is -0.33 MeV and the largest difference is 0.72 MeV, which corresponds to a range difference of 0.98 mm. The evaluation of different range-energy tables [64] yielded energy differences up to 1.71 MeV, which corresponds to a range difference of 3.84 mm.

Measurements of relative energy accuracy have been performed to analyse how well deviations of the revolution frequency or the radial offset (i.e. non-standard orbits) can be determined. It turns out that the relative energy accuracy for this application is ± 0.11 MeV. The authors conclude, that the absolute energy accuracy would not allow for patch field arrangements. However, that relative energy accuracy would be sufficient to support energy stacking.

- Precision: ± 0.72 MeV

MDACC Houston   The synchrotron at the MD Anderson Cancer Center (MDACC) has comissioned 94 separate beam energies [39]. The beam energy is checked before extraction by measuring the revolution frequency and the orbit position. A measurement of the beam orbit position to within $\pm 1\,\mathrm{mm}$ was found to assure proton range uncertainties of below $0.025\,\mathrm{g/cm^2}$ (corresponding to $0.25\,\mathrm{mm}$ depth in water).

- Precision: $\pm 0.25\,\mathrm{mm}$ (range in water)

Specific advantages

- Very precise time information can be taken from the RF

Specific drawbacks and challenges

- Only applicable for pre-verification (needs bunched beam)

2.6.2.3. Time-of-flight measurement in the beam transfer line

The idea here is to use the moment of beam activation or, if the beam is bunched, the bunch structure with two beam pick-ups located after the chopper and with a certain distance between them. Detectors capable of singe-particle counting can be used also during the treatment for a continuous beam.

The main drawback is the required time resolution as mentioned in section 2.6.2.1 equation (2.43) of about $3\,\mathrm{ps}$. Current technology provided resolutions of at least one order of magnitude worse [88, 58].

Specific advantages

- Confined measurement

Specific challenges and drawbacks

- The necessary time resolution for reasonable drift distances is not yet achievable

- The drift distance must also be verified precisely, comprising orbit excursions

- A detector reacting on single particles is necessary

2.6.3. Calorimeter

2.6.3.1. Measurement principle

Calorimetry implies the absorption of the particle energy in a bulk of material followed by the measurement of the deposited energy. It is therefore a destructive measurement. In the energy range given by table 2.3, the deposited energy causes either excitation or ionisation of the target material. At high energies, also Čerenkov light can be measured.

It is of great importance to understand, that a calorimetric measurement is inherently different from all other measurements presented in this analysis from a statistical point of view because it is a direct particle energy measurement. In the discussion of calorimeter performance below, the properties mentioned are referring to event-to-event measurements, i.e. single-particle energy measurements. That said, it is clear, that the uncertainty of the mean particle energy improves with the number of measured particle energies following the well-known relation

$$\sigma_E \equiv \sigma_{\bar{E}_{\mathrm{p}}} = \frac{\sigma_{E_{\mathrm{p}}}}{\sqrt{N}} \tag{2.44}$$

where σ_E is the uncertainty of the beam energy, which is equivalent to the uncertainty of the mean particle energy $\sigma_{\bar{E}_{\mathrm{p}}}$. $\sigma_{E_{\mathrm{p}}}$ is the uncertainty of the particle energy and N is the total number of measured particles. For simplicity, the identity $\sigma = \sigma_{E_{\mathrm{p}}}$ will be used in the following.

The number of particles extracted in a time of $100\,\mathrm{ms}$ at lowest beam intensity (given in section 2.3) results in the following approximations for the factor $1/\sqrt{N}$.

$$\text{Protons} \qquad\qquad \Rightarrow \qquad \frac{1}{\sqrt{N}} \approx 3 \times 10^{-4} \tag{2.45}$$

$$\text{Carbon ions} \qquad\qquad \Rightarrow \qquad \frac{1}{\sqrt{N}} \approx 1.6 \times 10^{-3} \tag{2.46}$$

Performance The performance of a calorimeter, quantified by the uncertainty of its measurement is a combination of several different sources [92]:

Signal quantum fluctuations The uncertainty induced by signal quantum fluctuations is inverse proportional to the number of generated quanta (photons, electron-hole pairs, etc.). These fluctuations obey the rules of Poisson statistics, thus for linear calorimeters their influence can be described by the following equation:

$$\frac{\sigma_E}{E} = \frac{a}{\sqrt{E}} \tag{2.47}$$

The value of a is a common way to express the energy resolution of a calorimeter. Equation (2.47) expresses the fact, that the relative precision of the energy measurement improves with increasing energy. E.g. the deposition of $1\,\mathrm{MeV}$ of energy in Germanium, where the generation of one electron-hole pair requires $2.9\,\mathrm{eV}$, results in 350000 quanta and the uncertainty of this number is $\sigma_{\mathrm{q}} = 1/\sqrt{N} \approx 0.17\,\%$.

Sampling fluctuations The uncertainty induced by sampling fluctuations naturally exists only in sampling calorimeters and for them dominates the overall performance. Sampling calorimeters are different from homogeneous calorimeters in that only parts of the energy absorbing material is instrumented. Therefore, they record only a part of the total particle energy called the sampling fraction f_{samp}. It goes beyond the scope of this

document to deduce the influence of sampling fluctuations. However, to approximate their influence, the following relation is cited from Wigmans [92]:

$$a_{\mathrm{samp}} \approx 2.7\,\% \times \sqrt{\frac{d}{f_{\mathrm{samp}}}} \tag{2.48}$$

where d is the thickness of the active layers in mm and f_{samp} is the sampling fraction for minimum ionising particles.

Instrumental effects The uncertainty induced by instrumental effects is often caused by electronic noise. Because the signal in linear calorimeters grows proportional to the energy E, the influence of electronic noise scales with $1/E$.

Shower leakage In general, lateral leakage has a weaker influence on the calorimeter performance than longitudinal leakage, because if a particle leaks without showering, the entire energy is lost, whereas lateral leakage causes only a certain part of the shower to be lost.

Albedo (back-splash) leakage becomes significant mainly for low energies. It can have a negative influence on upstream detectors if it causes particles to traverse them the opposite way.

Fluctuations in shower composition These fluctuations are relevant only at highest energies, where nuclear reactions cannot be excluded. They are caused by energy that is absorbed in such reactions (e.g. to release nuclei).

Radiation damage Typically, calorimeters are used for energy measurements of decaying particles generated in a precedent collision. In the application at hand, the level of radiation is much higher than usual, because the detector absorbs the accelerated beam. Therefore, radiation damage or rather radiation hardness is the dominating criterion for the choice of a calorimeter. The radiation damage of a calorimeter has different aspects, the most important of which shall be briefly explained:

Ionising radiation Depending on the type of calorimeter, ionising radiation causes different types of damage. For scintillators, it causes a deterioration of emission and transmission properties; in hydrocarbon materials, it causes out-gassing, which changes the composition of the material; in gaseous detectors, it causes depositions on anode or cathode, which causes a reduced gain or discharges; and in semiconductors, it causes increased leakage current and a degradation of the signal-to-noise ratio.

Dose rate effects For calorimeters that exhibit recovery capabilities, the period of time over which a certain dose is spread, is crucial for the amount of damage it causes. Often, it is difficult to evaluate long-term dose rate effects, simply because the needed time for testing is not available.

Curing   Certain calorimeter materials exhibit the capability to fully recover, even on a time-scale of a few hours (e.g. BGO). This often requires special curing procedures like thermal annealing or optical bleaching.

Induced radioactivity   Over long periods of time, long-lived radioactive nuclides can accumulate in the detectors. This increases the general noise level that must be accounted for and it complicates detector maintenance.

General advantages

- Direct measurement of the particle energy

- Single-particle measurement are independent of the beam intensity (for any but statistical reasons)

- Measurement confined to one detector

General challenges and drawbacks

- Destructive measurement; no synchronous verification

- New device: no (published) previous results from ion beam therapy facilities

2.6.3.2. Scintillators

The scintillator-based calorimeters most often used in high-energy physics are designed for energies in the order of GeV and above and in most cases, their radiation hardness does not meet the requirements of the application at hand. The CMS electromagnetic calorimeter made of $PbWO_4$ scintillating crystals is required to withstand radiation doses between 4 (Barrel) and $100\,kGy$ (end-caps) in 10 years of operation [8], which is orders of magnitude lower than what is required here.

2.6.3.3. Semiconductors

Some semiconductor counters can achieve a resolution of down to $150\,eV$ FWHM. However, their radiation hardness is too low for the application at hand. Chemical Vapor Deposition (CVD) diamond detectors have a worse energy resolution than other semiconductors because of the larger energy gap, but for the same reason are much more radiation hard.

Specific advantages

- Simple mechanical design

Specific challenges and drawbacks

- Probably needs replacement of the irradiated detector components on a yearly basis

2.6.3.4. Čerenkov light calorimeters

Traditional Čerenkov light calorimeters are made of lead-glass. These detectors are susceptible to radiation damage [92, p. 401] and are therefore inappropriate for the targeted application.

2.6.4. Particle range

2.6.4.1. Measurement principle

A measurement of the particle range is generally done by dumping the beam into several instrumented layers of material. With detectors that are capable of measuring the beam intensity or the number of stopped particles at their position it is possible to reconstruct the particle range distribution.

Since the particle energy relates only to statistical measures of the range distribution, the collection of a representative sample of range measurements is inherently necessary.

This is a destructive measurement and therefore cannot be done during the treatment itself, but only as a pre-verification method.

Performance   The performance is governed by the ability to measure low beam intensities with thin detectors in a short time. The precision of the measured particle range approximately equals the water-equivalent thickness of the material between two active layers. Since the amount and type of material is determined by the type of detector used, the specific characteristics will be described in the measurement sections below (2.6.4.2, 2.6.4.3).

The range that each layer corresponds to relies on the assumption, that the beam direction is perpendicular to the layers. It is intuitive, that a different beam angle causes a difference in the ranges at which the active layers are positioned and therefore a difference in the recorded particle range. It turns out, that for an unexpectedly deep detector of 30 cm, the beam angle that would cause a range difference equal to the required range accuracy of 0.25 mm is 2.3°. This is a few times above the maximum expected beam angle and therefore acceptable.

General advantages

- Direct measurement of the particle range

- Measurement confined to one detector

General challenges and drawbacks

- Measurement dependent on beam intensity (the energy is computed from statistical properties of the measurement)

- Destructive measurement

- Measurement (insignificantly) dependent on beam direction/angle

2.6.4.2. Multilayer Faraday cup

A multilayer Faraday cup measures the current induced by particles (charges) stopped in each layer. In order to reliably identify the Bragg peak position, the lower range limit of the current measurement has to be at least 20 times lower than the total beam current [27]. The lowest foreseen intensity of 4×10^6 particles for carbon ion beams is equivalent to a current of $2.8\,\mathrm{pA}$ (see section 2.3). The lower range limit of the employed amplifiers must thus be below approximately $190\,\mathrm{fA}$. Reliable current measurements with this sensitivity over long periods of time are very difficult if not impossible [14].

PSI Villigen   A Multi-Layer Faraday Cup (MLFC) consisting of 64 copper sheets separated by Kapton foils has been used [27]. There are two variants of the detector: the Optis MLFC is optimised for high accuracy at small ranges while the Gantry MLFC provides a slightly more uniform accuracy over all ranges. Both detectors cover about the same beam energy range of 68 to $252\,\mathrm{MeV}$. The best accuracy achieved with the Optis MLFC is $0.05\,\mathrm{mm}$ water-equivalent range. For high ranges, the accuracy becomes worse with about $1.5\,\mathrm{mm}$ water-equivalent range accuracy for above $300\,\mathrm{mm}$ range in the Optis MLFC.

To reach the given accuracies, an iterative routine has been developed. Due to the slow implementation, the evaluation could only be done off-line, i.e. not synchronous with the measurement. The currents are processed by logarithmic amplifiers with an integration time of $20\,\mathrm{ms}$. The lower range limit of the amplifiers is $10\,\mathrm{pA}$. It has been remarked, that for low beam currents of about $200\,\mathrm{pA}$, current read-out errors begin to degrade the achievable accuracy.

- Precision: 0.05–1.5 mm water-equivalent (w.-eq.) range

- Speed: offline (20 ms per current read-out)

HCL Cambridge Massachusetts   A MLFC consisting of 66 copper layers has been used [40] with 64 active channels. The insulators in between consist of two Kapton sheets. The unobstructed area is $7.6 \times 7.6\,\mathrm{cm}^2$. The average areal density per layer is $0.474\,\mathrm{g/cm^2}$. Measurements have shown, that secondary electron production has no effect. If a charge is kicked across an interface either from Kapton to copper or vice versa, no net charge flows through the meters. The nominal sensitivity of the analogue-to-digital converters is $2.44\,\mathrm{pC/count}$ with a range of ± 2047 counts. Each channel has been calibrated to $\pm 0.2\,\%$. The overall systematic error in the measurement points is estimated to $\pm 3\,\%$.

- Precision: 4.74 mm (w.-eq. thickness per layer calculated from average density)

NCC Koyang   Kwon et al. [50] have developed a MLFC consisting of 30 layers. Each layer is an aluminium plate insulated by Kapton foil. The achieved energy resolution is less than $2.5\,\mathrm{MeV}$ and it is stated, that a lower resolution is only a matter of thinner layers.

- Precision: $\pm 2.5\,\mathrm{MeV}$

Specific advantages

- Simple and robust mechanical layout

- Very accurate devices already exist (but only for much higher beam intensities)

Specific challenges and drawbacks

- Beam current at lowest intensity is too small for this measurement

2.6.4.3. Stack of secondary electron monitors

Considering the output current, Secondary Emission Monitors (SEMs) are between ionisation chambers and Faraday cups. Compared to ionisation chambers, their current output is about three orders of magnitude lower and their absolute precision is about a factor of 2 lower [36]. For low intensity beams (like the one used for treatment), a physical amplification process (e.g. exploiting a Micro-Channel Plate (MCP)) is necessary to get a useful signal [35].

Specific advantages

- Simple and robust mechanical layout

Specific challenges and drawbacks

- Output current too low at low beam intensity, would need additional amplification

- No reports on use for range measurement

2.6.5. Depth-dose distribution

2.6.5.1. Measurement principle

Similar to a measurement of the particle range, a depth-dose distribution measurement is generally done by dumping the beam into several instrumented layers of material. In contrast to a particle range measurement but similar to a calorimeter, a depth-dose measurement uses detectors, that are capable of measuring the deposited dose at their position. From multiple measurements at different depths, it is possible to reconstruct the depth-dose distribution. In contrast to calorimetry, where the total deposited energy is measured, this principle relies on the measurement of small fractions of the energy deposit at predefined locations.

A depth-dose distribution measurement must not be confused with a sampling calorimeter. The latter uses merely the knowledge of its sampling fraction and layer thickness to conclude the particle energy and the corresponding uncertainty. Whereas the former uses assumptions on the expected shape of the measured distribution to fit this model to the measurements and conclude the particle energy from the fittest parameters.

Naturally, all candidates for calorimetry can also be used in this fashion. But the most widely used dosimeters are ionisation chambers, which can not be used as homogeneous calorimeters in the targeted energy range for practical reasons. A comprehensive overview of all dosimeter types can be found in Podgorsak [69].

Performance   The performance of this detector principle is determined by the number, location and precision of the dose measurements. Because of the additional dose information compared to a pure range measurement, the same energy resolution can be achieved with fewer layers. Figure 2.17 shows an example for a depth-dose distribution of protons of an initial energy of 250 MeV (green line). The measurements (blue dots) are simulated with a relative uncertainty of 5 %, which is a conservative guess, well above the relative uncertainties between 2.0 and 2.6 % for standard dosimetry [65, p. 57 ff.] . The range is obtained from the measurement by fitting an appropriate function describing the dose distribution to the measurements.
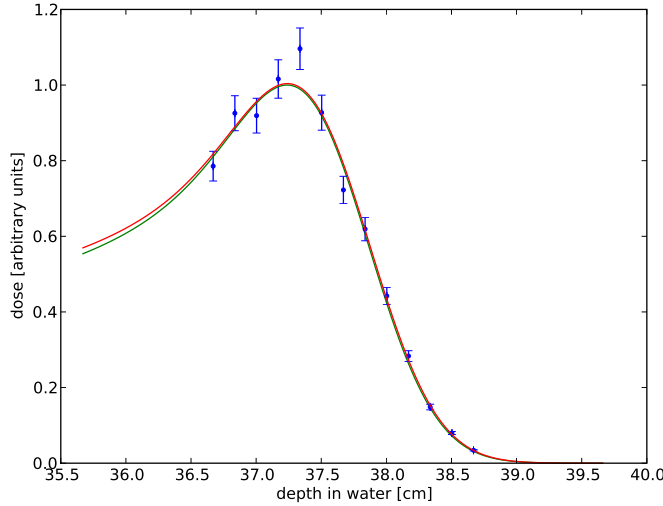

Figure 2.17.: Schematic illustration of a depth-dose measurement of 250 MeV protons in water. In this example, there are 13 active layers distributed over 2 cm. The indicated relative error of the dose measurement is 5 %. The red line is the true distribution and the green line is a fit from the measurements indicated as blue dots. The difference of the simulated and the reconstructed range in the example is 0.1 mm.

The example in figure 2.17 shows highest-energy protons. The depth-dose distribution of carbon ions and low-energy protons are narrower. Table 2.4 lists the values for range straggling and the FWHM of the Bragg peak for protons and carbon ions for comparison.

It has been tried to determine the optimal configuration on terms of number and position of dose measurements by repeated simulation like the one shown in figure 2.17.

Particle type	Energy	Range straggling	Bragg peak (FWHM)
Proton	60 MeV		∼ 6 mm
Proton	250 MeV	15.6 mm	27 mm
Carbon ion	120 MeV/n	1.4 mm	∼ 6 mm
Carbon ion	400 MeV/n	10.6 mm	9 mm

Table 2.4.: Values for range straggling and Bragg peak FWHM for protons and carbon ions in water at lowest and highest foreseen energy.

The resulting performance plot for the reconstruction of the range of 60 and 250 MeV protons in water is shown in figure 2.18.

As with a pure range measurement, the range that each active layers position corresponds to relies on the assumption, that the beam direction is perpendicular to the layers. It is intuitive, that a different beam angle causes a difference in the ranges at which the active layers are positioned and therefore a difference in the recorded depth-dose distribution. It turns out that, for an unexpectedly deep detector of 60 cm, the beam angle that would causes a range difference equal to the required range accuracy of 0.25 mm is 1.7 °, a value which is a few times above the maximum expected beam angle and therefore acceptable.

General advantages

- Measurement can be similar to phantom measurement used for medical verification (e.g. during commissioning)

- Direct measurement of the particle range

- Measurement confined to one detector

General challenges and drawbacks

- Measurement dependent on beam intensity (the energy is computed from statistical properties of the measurement)

- Destructive measurement

- Measurement (insignificantly) dependent on beam direction/angle

2.6.5.2. Multilayer ionisation chamber

From the many devices for Bragg peak measurement that are documented in literature or even commercially available [73, 46], only those with multiple sensitive layers can be taken into account. Any method that involves either movement of one sensitive layer within the phantom or that requires repeated reconfiguration of a range shifter for each measurement is inherently too slow.
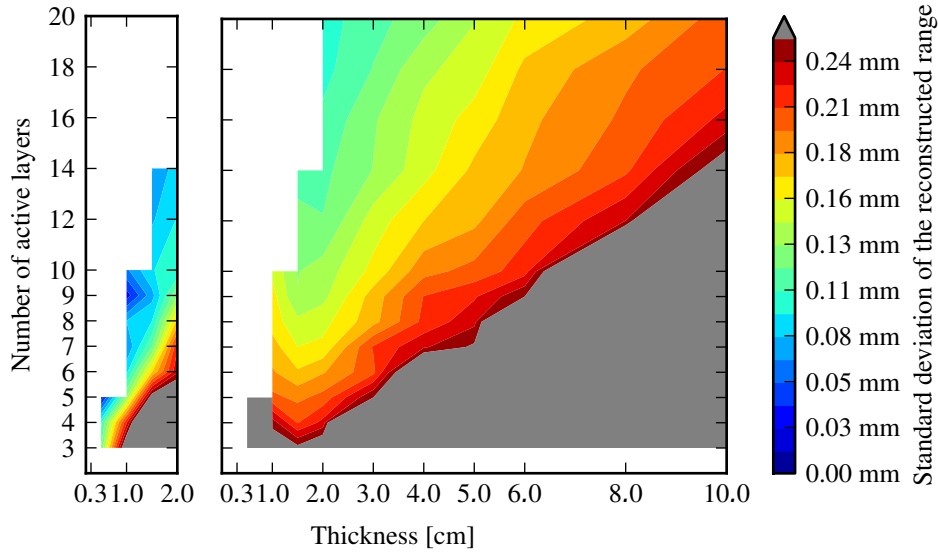
Figure 2.18.: Performance of range reconstruction from depth-dose measurements for 60 (left) and 250 MeV (right) protons. The colour indicates the standard deviation of the distribution of reconstructed ranges for different numbers of detectors (ordinate) distributed over different distances (abscissa, in cm). Values above 0.25 mm, which is the range accuracy requirement, are coloured in grey. The active layers are distributed such that the expected range was in the centre of all layers. Like before, the simulated dose measurements had a relative error of 5 %.

Characteristics Table 2.5 gives an idea of exemplary signal amplitudes in terms of generated charge. The numbers apply for 0.25 mm of air, the lowest beam intensity for each particle type (see 2.3), a collection time of 100 ms and are rounded down to two significant digits.

The amount of generated charges is calculated by integrating the energy deposit of the beam in air as given by the SRIM computer program [95] and dividing it by the average ionisation energy of air. From these numbers follows the required sensitivity of the electric amplifier used for the read-out.

Particle type	Particle energy	Ionisation medium	Generated charge
Proton	250 MeV	Air	11 pC
Proton	80 keV	Air	2400 pC
Carbon ion	400 MeV/n	Air	12 pC
Carbon ion	333 keV/n	Air	950 pC

Table 2.5.: Generation of charge by protons and carbon ions at highest respective incident energy and at the maximum LET in air. The lowest foreseen beam intensities are used for each particle type: 10^8 particles per second for protons and 4×10^6 particles for carbon ions.

INFN Torino The Magic Cube [22] is a detector consisting of 12 strip ionisation chambers interleaved with water-equivalent slabs. Each chamber has a sensitive area of $24 \times 24 \, \text{cm}^2$ and is segmented into 64 strips that can be read out separately, giving a total number of 768 channels for the whole detector. The chambers can be filled with either air or nitrogen. The device is capable of recording a three-dimensional image of the dose distribution i.e. including the incident beam angle. The ionisation chamber readout time used was 1 ms, but the electronics is said to support down to 160 µs.

Since no explicit data on the range accuracy could be found, it is estimated to be less than 1 mm, which is the water-equivalent thickness of each ionisation chamber for 270 MeV carbon ions on the LET plateau.

- Precision: < 1 mm (w.-eq. thickness of layer)

- Speed: 1 ms (160 µs)

GSI Darmstadt An active multi-plane phantom [89] consisting of 60 ionisation chambers interleaved with PMMA slabs has been developed. The active area of the detector is $9.6 \times 9.6 \, \text{cm}^2$. The ionisation chambers are made of aluminised Mylar foils in the centre of a twofold 3 mm gap active gap which can be operated at maximum $\pm 1200 \, \text{V}$. The PMMA slabs between the ionisation chambers are 5 mm thick. The total thickness of the layers is 36.2 cm which is enough to stop carbon beam up to approximately 450 MeV/n.

- Precision: < 5 mm (thickness of PMMA layers)

- Speed: n/a

PSI Villigen   A multilayer ionisation chamber for routine quality assurance measurements has been developed [53]. It consists of 128 ionisation chambers with 1 mm spacing between anode and cathode. The cathodes are 1 mm thick Aluminium-Magnesium alloy plates that are also used as energy shifters.

The sensitive area is $10{\times}10\,\mathrm{cm}^2$. The water-equivalent thickness of one layer is 2.27 mm summing up to 290.8 mm for the whole device.

- Precision: $< 2.27\,\mathrm{mm}$ (water-equivalent thickness per layer)

- Speed: 1 ms

Specific advantages

- This type of measurement is common practice in ion beam therapy during calibration and commissioning.

2.6.5.3. Plastic scintillator stack

If no passive absorbers are used, this can also be designed as a calorimetric measurement (see section 2.6.3).

PSI Villigen   A detector system for proton radiography has been developed [68]. The system comprises a stack of 3 mm thick plastic scintillator tiles. The electronics is able to process a rate of up to 10^6 protons per second. The layer thickness matches the expected combined effect of range straggling and beam momentum band in the experiment.

Specific advantages

- Self-supporting detector material

- Material resembles human tissue

Specific challenges and drawbacks

- Cannot handle high-intensity beams

- Insufficient radiation hardness

2.6.5.4. CVD diamond stack

If no passive absorbers are used, this can also be designed as a calorimetric measurement (see section 2.6.3).

GSI Darmstadt   CVD diamond dosimeters have been used to record depth-dose distributions [74]. The documented measurement is based on single-particle counting and achieves a counting efficiency of $100 \pm 7\,\%$ for carbon ions with an initial energy of $399\,\mathrm{MeV/n}$ impinging on a $483\,\mathrm{\mu m}$ thick single-crystal CVD detector at a fluency of $10^7\,\mathrm{particles/cm^2}$. The particle range measurement has been based on a single layer with a varying number of PMMA slabs in front.

Specific advantages

- Linear behaviour as a function of dose

- High resolution in time

Specific challenges and drawbacks

- Effects of ions stopped in the detector volume, e.g. regarding material damage and resolution, are not well known

- The technology is not mature

2.6.6. Positron emission tomography

Positron Emission Tomography (PET) range verification for proton treatments is possible and the precision of the range measurement has been shown [49] to be at $1\,\mathrm{mm}$ standard deviation for an offline measurement inside a phantom. In vivo measurements suffer from additional challenges like blood perfusion, motion and variations in tissue composition.

The range verification precision requirement cited in section 2.3 cannot be achieved.

3. Time-of-flight Measurement

3.1. Measurement principle

The fundamental measurement principle of the energy measurement presented here is that of a time-of-flight measurement in a synchrotron. That is, from measurements of the particle trajectory and the time it takes the particle to travel along that trajectory, the particle velocity is computed. With the particle rest mass m_0, which depends on the particle type, the kinetic particle energy E_k is

$$E_k = m_0 c^2 \left(\gamma - 1 \right) \tag{3.1}$$

with the speed of light in vacuum c and the well-known relativistic factors

$$\gamma = \frac{1}{\sqrt{1 - \beta^2}} \qquad \text{and} \qquad \beta = \frac{v}{c} \tag{3.2}$$

The time t it takes the particle to travel along the circumference C of a closed orbit equals the inverse of the revolution frequency f. With the velocity

$$v = \frac{C}{t} = Cf \tag{3.3}$$

the equation for the kinetic energy becomes

$$E_k = \frac{mc^2}{\sqrt{1 - C^2 f^2 / c^2}} - mc^2 \tag{3.4}$$

3.1.1. Beam energy

The above equations hold for single particles. They do not necessarily apply for an ensemble of particles, like a bunch in a beam: due to Jensen's inequality [48], the kinetic energy calculated from the average circumference and the average frequency is an underestimation of the average kinetic particle energy (beam energy): Because equation (3.1) is a convex function, Jensen's inequality states:

$$E_k \left(\langle \beta \rangle \right) \leq \langle E_k \left(\beta \right) \rangle \tag{3.5}$$

An upper bound for the difference between the two sides is given by [83]:

$$\Delta_{\text{Jensen}} = \langle E_k \left(\beta \right) \rangle - E_k \left(\langle \beta \rangle \right) \leq E_k \left(\beta_{\text{min}} \right) + E_k \left(\beta_{\text{max}} \right) - 2 E_k \left(\frac{\beta_{\text{min}} + \beta_{\text{max}}}{2} \right) \tag{3.6}$$

Particle type	Beam energy	$\Delta_{\text{Jensen}}/E_k \leq$
Protons	60 MeV	0.96×10^{-5}
Protons	250 MeV	1.25×10^{-5}
Carbon ions	120 MeV/n	1.08×10^{-5}
Carbon ions	400 MeV/n	1.37×10^{-5}

Table 3.1.: Upper bounds for the relative underestimation of the beam energy due to Jensen's inequality for different particle types and energies.

Assuming a full nominal momentum spread of $dp/p = 0.0004$ [20, p. 325] for all particle types and energies, the values of the upper bound for the foreseen edge cases (i.e. lowest and highest kinetic energy) are listed in table 3.1.

The relative underestimation is roughly $\mathcal{O}(10^{-5})$, which is about two orders of magnitude below the requirement for the measurement precision given in section 2.3. Since this is a systematic error, it can be compensated for during calibration. Therefore equation (3.5) will be approximated as an equality in the following.

3.2. Orbit circumference

The circumference of a closed orbit in a synchrotron is a function of the circumference of the reference orbit and the transverse displacement of the closed orbit w.r.t. the reference orbit. The circumference of the reference orbit depends only on the geometry and alignment of the lattice magnets.[1] Therefore it is assumed constant over time. Major uncertainties introduced by the dipole geometry and alignment can be eliminated by repeated measurements during commissioning. The relative time variation of the reference orbit circumference caused by the Earth tides [12] is

$$\frac{\Delta C}{C} \approx 4 \times 10^{-8} \quad \Rightarrow \quad \Delta C \approx 3\,\mu\text{m} \tag{3.7}$$

which can be neglected in this application. On the other hand, variations due to singular events, such as subsidences or repair and maintenance work, can and should be accounted for by re-evaluation the reference orbit circumference after the event.

3.2.1. Vertical displacement

Figure 3.1 illustrates the situation of a closed orbit displaced vertically from the reference orbit. The length of one section of the displaced orbit is

$$\ell^{\star} = \sqrt{\ell^2 + \Delta y^2} = \ell\sqrt{1 + \left(\frac{\Delta y}{\ell}\right)^2} \approx \ell\left[1 + \frac{1}{2}\left(\frac{\Delta y}{\ell}\right)^2\right] = \ell + \frac{\Delta y^2}{2\ell} \tag{3.8}$$

---

[1]In particular the reference orbit is independent of magnet current settings. They are trimmed to reproduce the reference orbit.
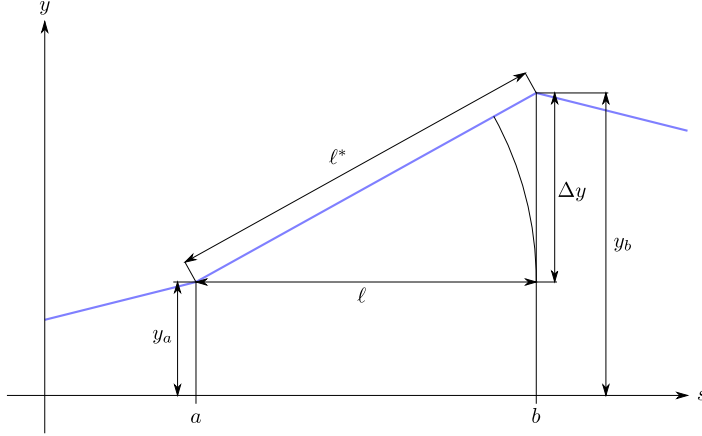
Figure 3.1.: Schematic illustration of one section of a vertically displaced closed orbit (blue line). The abscissa corresponds to the reference orbit. The vertical displacement y is a function of the longitudinal coordinate s on the reference orbit.

Number of quadrupole magnets	24
Orbit margin	$10\,\text{mm}$
Circumference of the design orbit	$77.648\,\text{m}$

Table 3.2.: Preliminary numbers of the MedAustron synchrotron (assumed) used to estimate the maximum influence of vertical closed orbit displacement on the closed orbit circumference.

where ℓ is the length of the section along the reference orbit and $\Delta y = y_b - y_a$ is the change in vertical displacement. The approximation is a binomial approximation under the assumption that $(\Delta y/\ell)^2 \ll 1$. The total circumference C of the closed orbit then evaluates to

$$C = C_0 + \sum_{i=1}^{N} \frac{\Delta y_i^2}{2\ell_i} \tag{3.9}$$

where C_0 is the circumference of the reference orbit. Since the reference orbit is first defined during synchrotron commissioning, its circumference is assumed to be equal to the design orbit circumference in the following. The elements responsible for a vertical deflection of the beam are the quadrupole magnets, thus N is the number of quadrupoles. An upper bound for the deflection is provided by the orbit margin. To estimate the maximum influence of vertical orbit displacement on the orbit circumference, preliminary numbers of the MedAustron synchrotron are presented in table 3.2.

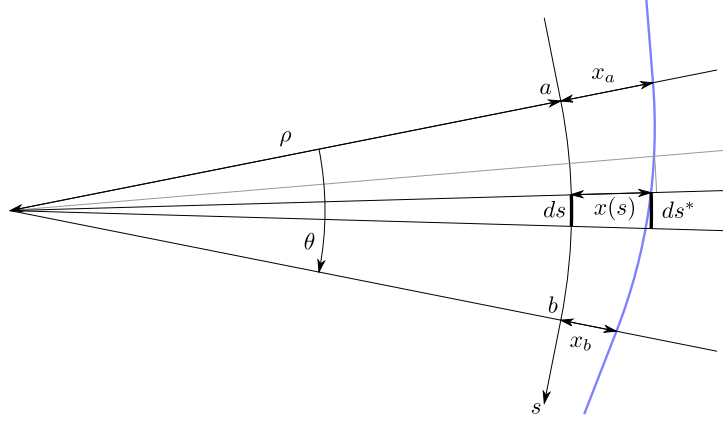The total maximum circumference change $\Delta C = C - C_0$ due to vertical displacement results as

Figure 3.2.: Curved section of a horizontally displaced closed orbit (blue line) in a dipole magnet. The bending radius of the reference orbit is ρ and the bending angle is θ. The horizontal displacement x is a function of the longitudinal coordinate s on the reference orbit. On the displaced closed orbit, the longitudinal coordinate is denoted as $s^\star$.

$$\max\left(\Delta C\right) \approx N\frac{\Delta y_{\max}^2}{2\ell} \approx N^2\frac{\Delta y_{\max}^2}{2C_0} \approx 1.5\,\mathrm{mm} \tag{3.10}$$

To simplify the sum, approximately equal quadrupole spacing $\ell = C_0/N$ is assumed.

3.2.2. Horizontal displacement

Inside a dipole field the situation is slightly more complicated because a horizontal displacement effectively changes the arc radius of the orbit and therefore has a significantly greater influence on the arc length than a vertical displacement. Figure 3.2 shows the geometry of a closed orbit, which is horizontally displaced with respect to the reference orbit, inside a dipole magnet. The arc length along the reference orbit is $\ell = \theta\rho$, i.e. the bending angle times the bending radius. It can also be written as

$$\ell = \int_0^\theta \rho \,\mathrm{d}\theta = \int_a^b \,\mathrm{d}s \tag{3.11}$$

where a is the beginning and b the end of the curved section in the longitudinal coordinate s of the reference orbit, thus $b - a = \ell$. The corresponding differential of the displaced closed orbit $\mathrm{d}s^\star$ has to account for the varying bending radius $\rho^\star = \rho + x(s)$ (see A.1 for details):

$$\mathrm{d}s^\star = \sqrt{\rho^{\star 2} + \left(\frac{\mathrm{d}\rho^\star}{\mathrm{d}\theta}\right)^2}\,\mathrm{d}\theta = \sqrt{(\rho+x)^2 + \left(\frac{\mathrm{d}x}{\mathrm{d}s}\rho\right)^2}\,\mathrm{d}\theta = \sqrt{\left(\frac{\rho+x}{\rho}\right)^2 + \left(\frac{\mathrm{d}x}{\mathrm{d}s}\right)^2}\,\mathrm{d}s \tag{3.12}$$

As a first approximation, a linear interpolation of the horizontal closed orbit displacement $x(s)$ is used:

$$x(s) \approx x_a + \frac{x_b - x_a}{b - a}(s - a) \tag{3.13}$$

Symmetrisation around $s = 0$ will later simplify the integration:

$$x(s) \approx \frac{x_a + x_b}{2} + \frac{x_b - x_a}{b - a}\left(s - \frac{a+b}{2}\right) \tag{3.14}$$

From the assumption that the change in horizontal displacement $\Delta x = x_b - x_a$ is much smaller than the arc length on the reference orbit ($\Delta x \ll \ell$) follows:

$$\frac{\mathrm{d}x}{\mathrm{d}s} = \frac{\Delta x}{\ell} \ll 1 \tag{3.15}$$

It is further assumed that the displacement is small compared to the bending radius ($x \ll \rho$), which gives

$$\frac{\rho + x}{\rho} \approx 1 \tag{3.16}$$

With those two assumptions, the arc length along the displaced orbit becomes (see A.2):

$$\ell^\star = \int_{\ell^\star} \mathrm{d}s^\star = \ell + \int_a^b \left(\frac{x}{\rho}\right)\mathrm{d}s + \frac{1}{2}\left(\frac{\mathrm{d}x}{\mathrm{d}s}\right)^2 \int_a^b \left(\frac{\rho}{\rho + x}\right)\mathrm{d}s \tag{3.17}$$

Substituting equation (3.14) for x inside the integrals yields

$$\ell^\star = \ell + \left(\frac{x_a + x_b}{2\rho}\right)\ell + \frac{\rho\Delta x}{2\ell}\log\left(\frac{\rho + x_b}{\rho + x_a}\right) \tag{3.18}$$

Rewriting the logarithm and truncating after the first term of the series expansion (see A.3) finally gives

$$\ell^\star = \ell + \theta\bar{x} + \frac{\rho\Delta x}{2\ell}\frac{\Delta x}{\rho + x_a} \approx \ell + \theta\bar{x} + \frac{\Delta x^2}{2\ell} \tag{3.19}$$

where θ is the bending angle and $\bar{x} = (x_a + x_b)/2$ is the central displacement within the section. Compared with the corresponding equation for the vertical displacement (3.8), the only difference is the additional term $\theta\bar{x}$, which depends on the bending angle. This additional term is obviously only non-zero in curved sections. The total circumference of the displaced closed orbit from equation (3.9) can now be completed with the contributions from equation (3.19) to

$$C = C_0 + \sum_{i=1}^{N} \theta_i \bar{x}_i + \sum_{i=1}^{N} \frac{\Delta x_i^2 + \Delta y_i^2}{2\ell_i} \tag{3.20}$$

The maximum influence of the last term is approximately twice the maximum influence of a vertical displacement alone as in equation (3.10). Using a similar approach for the second ("bending") term and assuming a constant horizontal displacement that equals the orbit margin ($x_{\max} \approx 10\,\text{mm}$), yields

$$\max\left(\sum_{i=1}^{N} \theta_i \bar{x}_i\right) = x_{\max} \sum_{i=1}^{N} \theta_i = 2\pi x_{\max} \approx 62.8\,\text{mm} \tag{3.21}$$

The second and third term in equation (3.20) cannot be at maximum simultaneously and summing their respective maximum influence does not make sense. Therefore the total maximum circumference change as given by the orbit margin can be approximated to

$$\max(\Delta C) \approx 62.8\,\text{mm} + 1.5\,\text{mm} = 64.3\,\text{mm} \tag{3.22}$$

which is the sum of equation (3.21) and equation (3.10).

3.2.3. Measurement of the transverse displacement

The transverse displacement of the closed orbit from the reference orbit is measured by Beam Position Monitors (BPMs). Figure 3.3 shows the location of the main dipoles (green) and the horizontal BPMs (small black rectangles).

Since the shift is not measured directly at the borders of each magnet, it has to be interpolated from the beam position measurements. Without detailed knowledge of the synchrotron lattice, the easiest approximation is to do a linear interpolation between the measurements and compute the central displacement $\bar{x}_i$ in each dipole as well as the horizontal and vertical change of displacement from that interpolation.

Figure 3.4 shows the horizontal offset of an exemplary closed orbit that has been simulated by assigning random errors to the lattice magnets within their specifications. It also shows the linear interpolation between the beam position measurements. In principle the available lattice knowledge provides constraints that would allow for a more realistic interpolation, but the linear interpolation serves well as an ad-hoc approximation, is easier to realise and – as is shown below – achieves sufficient precision.

3.2.4. Circumference uncertainty

By applying the laws of propagation of uncertainty to equation (3.20), the influence of the beam position monitor precision on the uncertainty σ_C of the circumference measurement can be derived as
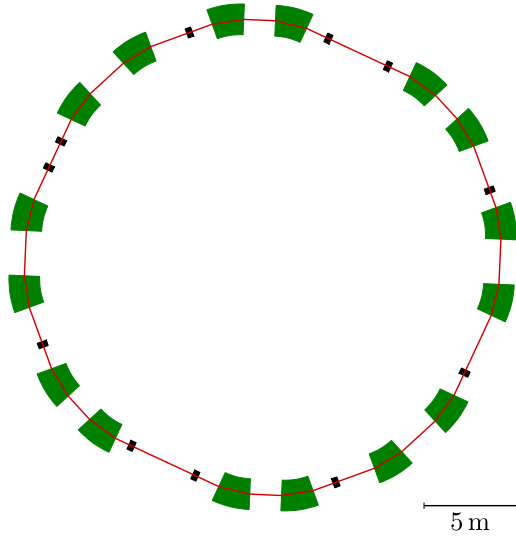
Figure 3.3.: The MedAustron synchrotron with the basic elements involved in a measurement of the orbit circumference: the main dipoles are coloured in green and the horizontal beam position monitors are coloured in black. The reference orbit is indicated as a red line. The horizontal closed orbit displacement x_i from the reference orbit at each beam position monitor location can be computed from alignment data and the output of the monitor.
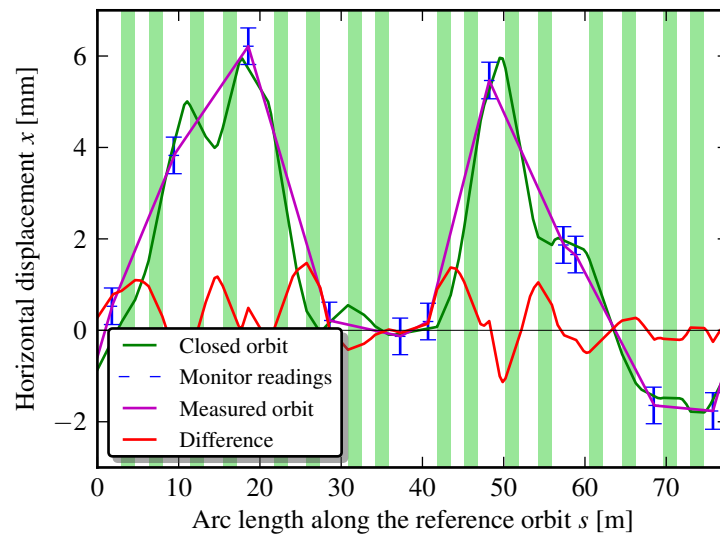
Figure 3.4.: Example for a circumference measurement with BPMs. The circumference offset of the closed orbit (green line) related to the reference orbit is 9.3 mm. The circumference offset of the orbit computed from the measured beam positions (blue line) is 11.4 mm. The red line is the difference between the two. The positions and lengths of the main ring dipoles are indicated by the light green bars.

$$\sigma_C^2 = \sum_{i=1}^{N} \left[\left(\frac{\partial C}{\partial x_i} \right)^2 \sigma_x^2 + \left(\frac{\partial C}{\partial y_i} \right)^2 \sigma_y^2 \right]$$

$$= \sum_{i=1}^{N} \left[\left(\frac{\theta_i + \theta_{i+1}}{2} + \frac{\Delta x_i}{\ell_i} - \frac{\Delta x_{i+1}}{\ell_{i+1}} \right)^2 \sigma_x^2 + \left(\frac{\Delta y_i}{\ell_i} - \frac{\Delta y_{i+1}}{\ell_{i+1}} \right)^2 \sigma_y^2 \right] \qquad (3.23)$$

where σ_x is the measurement uncertainty of the horizontal displacement and σ_y is the measurement uncertainty of the vertical displacement. To approximate this uncertainty, similar estimates as for the total influence approximations (3.10) and (3.21) are applied:

$$\Delta x_i = -\Delta x_{i+1} = \Delta x_{\max} = 20\,\mathrm{mm}$$
$$\Delta y_i = -\Delta y_{i+1} = \Delta y_{\max} = 20\,\mathrm{mm}$$
$$\Delta \ell_i = \Delta \ell_{i+1} = \frac{C_0}{N_{\mathrm{quads}}} = 3.24\,\mathrm{m}$$

Without dipoles ($\theta = 0$), the maximum variance σ_C^2 would become

$$\max \left(\sigma_{C,\mathrm{straight}}^2 \right) \approx 3.7 \times 10^{-3} \left(\sigma_x^2 + \sigma_y^2 \right) \qquad (3.24)$$

To estimate the summands inside curved sections, a theoretical ring consisting only of main dipoles with a maximum orbit deflection at each dipole border is assumed. From figure 3.3 it can be seen that at MedAustron the number of main dipoles is 16. The maximum additional variance of such a ring would be

$$\max \left(\sigma_{C,\mathrm{dipoles}}^2 \right) \approx N_{\mathrm{dipoles}} \left(\frac{2\pi}{N_{\mathrm{dipoles}}} + \frac{2\Delta x_{\max}}{\ell_{\mathrm{dipoles}}} \right)^2 \sigma_x^2 \approx 2.7762\,\sigma_x^2 \qquad (3.25)$$

Due to the linear interpolation between beam position monitors, the σ_x and σ_y correspond to the horizontal and vertical BPM precision, respectively. With the assumption that the two are approximately equal, the maximum uncertainty of the closed orbit circumference measurement can be conservatively estimated to

$$\max \left(\sigma_C \right) \approx 1.67\,\sigma_{xy} \qquad (3.26)$$

For a more realistic approximation, the error of the orbit interpolation, the uncertainty of the reference orbit circumference, the dipole lengths and the uncertainties introduced by alignment must be taken into account.

For a cross-check a simulation of 1000 different closed orbits, that were each fitted to sets of random lattice errors within the specifications of the magnets [20], has been performed (see Figure 3.5). The beam position monitor errors were also assigned random values from the same specifications. The standard deviation of reconstructed circumferences ($\sigma_C = 0.54\,\mathrm{mm}$) confirms equation (3.26) as an upper limit. The simulation
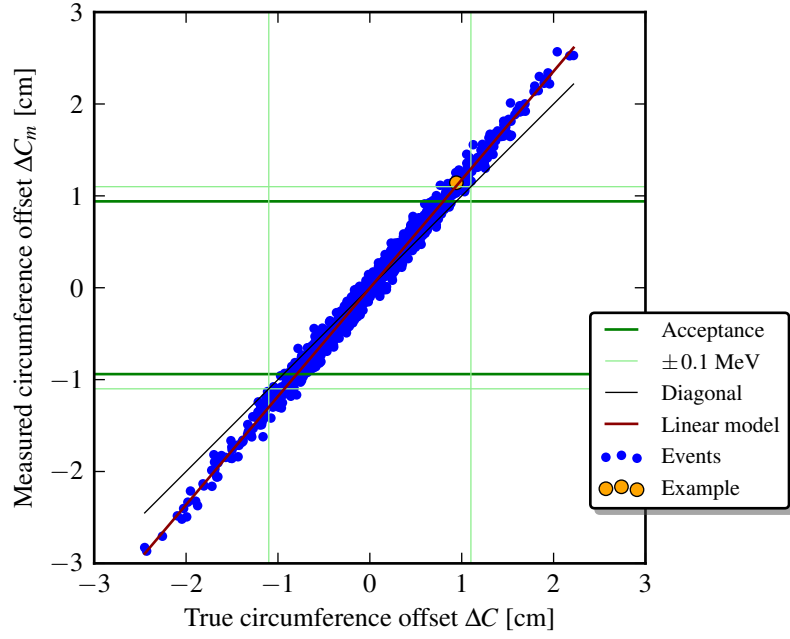
Figure 3.5.: Scatter plot of 1000 differently displaced closed orbits with the difference ΔC between the closed orbit circumference and the reference orbit circumference on the horizontal axis and the difference ΔC_m between the orbit circumference computed from simulated beam position measurements and the circumference of the reference orbit on the vertical axis. The orange dot represents the example shown in figure (3.4) The distribution clearly shows a linear relation between the two. Linear regression returns a scaling factor of 1.181.
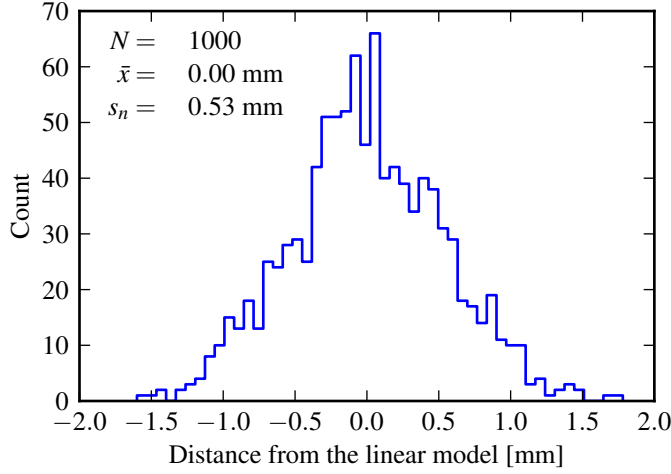
Figure 3.6.: Distribution of the orbit circumferences computed from simulated beam position measurements around the linear model shown in figure 3.5.

also revealed a systematic error in the reconstructed circumference, which leads to an overestimation of the circumference change:

$$\Delta C_{\text{computed}} \approx 1.18 \times \Delta C_{\text{simulated}} \qquad (3.27)$$

This overestimation can be explained with the locations of the beam position monitors relative to the quadrupoles. It turns out that the BPMs are always located in the longer straight sections (see figure 3.3), all of which contain focusing quadrupoles only. In the shorter straight sections, which contain the defocusing quadrupoles, the displacement of the closed orbit is eventually smaller then elsewhere, but there are no BPMs. Therefore, the average displacement at the BPM locations is higher than the overall average displacement, which leads to an overestimated circumference change when it is reconstructed from the BPM measurements. Since this overestimation only tightens the energy constraints (i.e. the reconstructed circumference is more "off" than the actual one), the measurement is a conservative indicator. Figure 3.6 shows the distribution of the simulated orbit circumference measurements around the linear model given by equation (3.27).

3.2.5. Radio-frequency feedback loops

It is an interesting thought experiment to look at the impact of a change in orbit length on the low-level Radio Frequency; often refers to the Radio Frequency accelerating cavity (RF) feedback loops. It turns out that changes of the orbit circumference are "seen" by the phase loop and/or radial loop of the RF beam control loops and eventually compensated by a change in the applied frequency.

Variable name	Symbol
Revolution frequency	f_{rev}
Sampling frequency	f_{s}
Counter frequency	f_{c}
True/expected signal frequency	$\hat{f}$
Measured signal frequency	f
Frequency resolution	δf
Mean measured signal frequency of N measurements	$\bar{f}$
Resolution of the mean frequency	$\delta\bar{f}$
Frequency bandwidth	B_f
Bandwidth resolution	δB_f

Table 3.3.: Overview of the frequency variable names used throughout section 3.3.

Of course, this does not supersede the circumference measurement described above, because it is the purpose of this thesis to describe a method of energy qualification independent of assumptions concerning the correct functioning of any other accelerator part (such as the RF beam control loops).

3.3. Revolution frequency

The easiest way to obtain the revolution frequency would be to read it from the RF beam control loops. If the closed phase and radial loop [38] are working correctly, the returned frequency equals the beam revolution frequency (i.e. the central particle revolution frequency). Although this is an entirely valid approach, it might be advantageous to use a second and redundant means of frequency measurement to reduce the risk of obtaining an incorrect value.

The revolution frequency can directly be deduced from the signal of a pick-up. There are several ways to do so, two of which will be discussed in this section:

- a Fourier transform of the recorded signal allows to identify the revolution frequency or

- a radio frequency counter measures the time between two occurrences of a trigger condition in the signal.

Both methods and their respective performance will be briefly discussed.

The frequency measurement performed for the energy calibration of the SPS at CERN [91] unfortunately can not be used for a fast energy measurement ($\mathcal{O}(1\,\mathrm{ms})$) because it requires several tune and frequency measurements at different chromaticity settings and is thus by far too slow. On the other hand, the method may be useful for calibration purposes at MedAustron.

Table 3.3 lists the names of different frequency variables used in the following subsections.
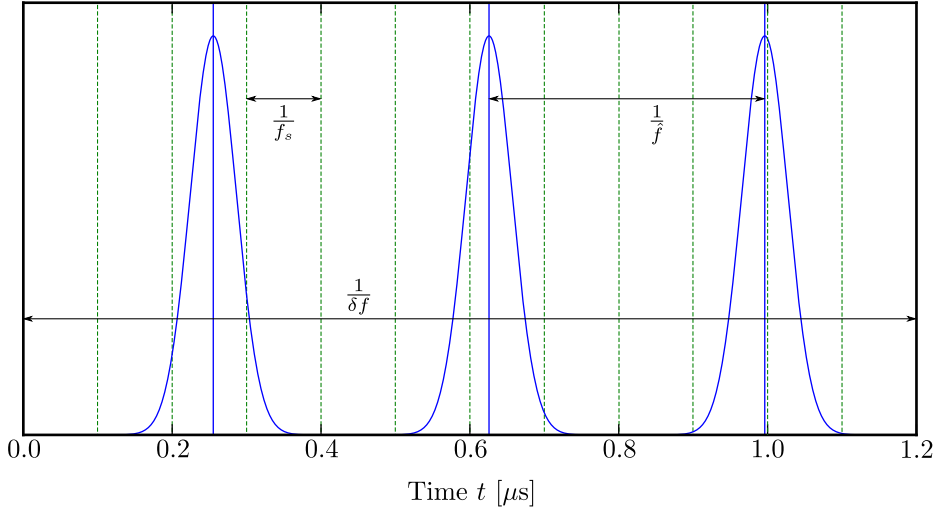
Figure 3.7.: Illustration of an analogue signal (e.g. as recorded by a pick-up) in time domain. In this domain, frequencies are indicated as reciprocal values of time durations.

3.3.1. Fourier transform

A few requirements must be met to determine the revolution frequency via an analysis of the beam pick-up signal using a Fourier transform (more specifically: a discrete Fourier transform). The sampling frequency f_{s} (i.e. the frequency at which samples of the signal are recorded) must be more than twice the maximum expected signal frequency $\max(\hat{f})$ to avoid ambiguities in the transformation result (Nyquist–Shannon sampling theorem):

$$f_{\mathrm{s}} > 2\,\max(\hat{f}) \tag{3.28}$$

The frequency resolution δf is determined by the total observation period T (also called the record length) during which samples are recorded. To achieve the resolution δf, the observation period must be equal to the inverse resolution (or greater):

$$T \geq \frac{1}{\delta f} \tag{3.29}$$

This time has to be spent after the synchrotron ramp, but before the beam is debunched (see section 2.5.3). Using a higher harmonic of f of degree n improves the frequency resolution by a factor of $1/n$ and therefore can allow for an n times shorter sampling period. However, the strength of higher harmonics depends strongly on the signal shape, which may change between measurements. Therefore it is safer to rely on the first harmonic for the purpose of energy verification.

Figure 3.7 shows a Gaussian-shaped signal in time domain, which represents an exemplary longitudinal profile recorded by a pick-up. The repetition rate of the signal corresponds to the revolution frequency, if there is only one bunch in the machine:
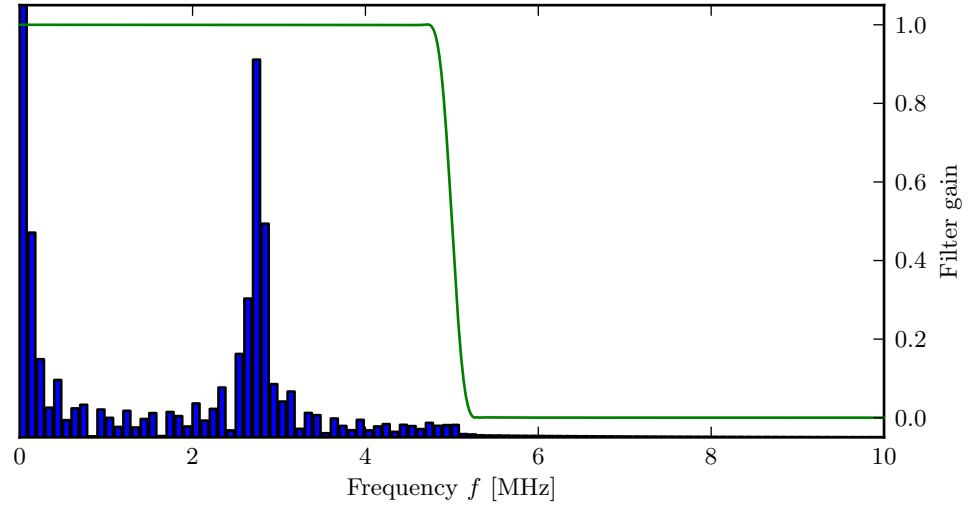
Figure 3.8.: Illustration of a sampled signal in frequency domain together with the transfer function of the digital low-pass filter used in this example. The same signal frequency as in figure 3.7 is used, but the sampling frequency is doubled and the record length increased. The first harmonic can be clearly identified at 2.7 MHz.

$$\hat{f} = f_{\text{rev}} = 2.7 \, \text{MHz} \tag{3.30}$$

The dashed vertical lines indicate the sampling times, where the distance between two samples is determined by the sampling frequency:

$$f_{\text{s}} = 10 \, \text{MHz} \tag{3.31}$$

The record length indicated as the horizontal extension of the plot determines the frequency resolution:

$$\delta f = \frac{1}{T} = \frac{1}{1.2 \, \mu\text{s}} \approx 0.8 \, \text{MHz} \tag{3.32}$$

Depending on the sampling frequency, a discrete Fourier transform exhibits a property called "aliasing". Aliasing is a type of disturbance that manifests as unwanted components (peaks) in the frequency domain. This distortion can be eliminated by applying a low-pass filter to the signal before computing the transform. Figure 3.9 shows a block diagram of the processing chain.

Figure 3.8 shows an exemplary transfer function of a low-pass filter together with a bar chart of the frequency components as returned by the fast Fourier transform. The analogue input signal for this example is identical to the signal shown in figure 3.7, but the sampling time is increased to 10 µs in order to achieve a frequency resolution of
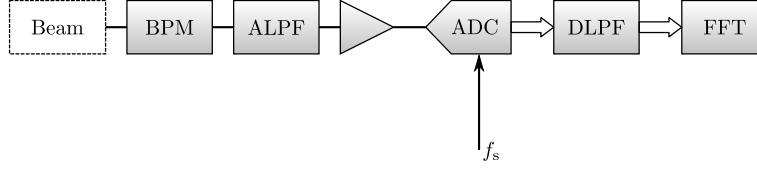
Figure 3.9.: Schematic block diagram of the signal processing chain to retrieve the Fourier transform. The beam signal is "picked-up" e.g. by the sum signal of a Beam Position Monitor (BPM). Then an Analogue low-pass filter (ALPF) removes higher frequency components to prevent distortions. The filtered signal is then amplified and sampled in an Analogue-to-digital converter (ADC) at the sampling frequency f_s. The subsequent Digital low-pass filter (DLPF) complements the previous analogue filter and damps remainders of frequencies above the maximum expected frequency. Finally, the Fast Fourier Transform (FFT) is computed from the set of filtered samples.

$$\delta f = \frac{1}{T} = \frac{1}{10\,\mu\mathrm{s}} = 0.1\,\mathrm{MHz} \tag{3.33}$$

Only the lower half band of frequencies is plotted i.e. $f_\mathrm{s} = 20\,\mathrm{MHz}$. The low-pass filter is configured for a cut-off at $5\,\mathrm{MHz}$ and an (arbitrary) transition width of $500\,\mathrm{kHz}$.

3.3.2. RF counter

The working principle of the RF counter measurement is illustrated in figure 3.10. As soon as the recorded signal (which corresponds to the longitudinal profile of the bunch) fulfils a trigger condition (e.g. surpasses a trigger level), a fast RF counter is started and increased at a certain counter frequency f_c until a second trigger occurs which stops the measurement. The measured signal frequency is then given by

$$f = \frac{f_\mathrm{c}}{n} \tag{3.34}$$

where n is the number of counts between the two triggers. If there is only one bunch in the machine, this is also the measured revolution frequency. For the measurement to be useful, it is required that $n \gg 1$ and thus $f_\mathrm{c} \gg \hat{f}$. The error of this measurement is determined by the value and jitter of f_c. Taking trigger errors into account (as illustrated by the rightmost peak in figure 3.10), results in the following approximation of the absolute error of the measured frequency:

$$\Delta f^2 = \left(\frac{\Delta f_\mathrm{c}}{n}\right)^2 + \left(\frac{f_\mathrm{c}}{n^2}\right)^2 (1 + \Delta\tau f_\mathrm{c})^2 \tag{3.35}$$

where the first term is the counter jitter $\Delta f_\mathrm{c}/n$. Inside the brackets, the two terms represent the digitalisation or "phase" of the signal with respect to the counter on the one hand and the trigger error on the other hand, where $\Delta\tau$ is the introduced trigger
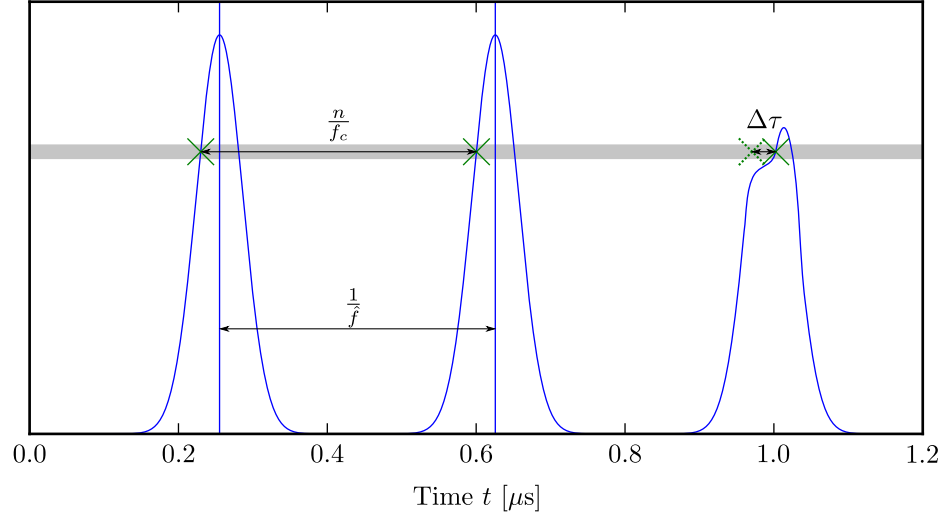
Figure 3.10.: Working principle of the radio-frequency counter measurement. The counter is characterised by a trigger level (grey bar) and a counting frequency f_c. The measurement evaluates the counts n between two trigger occurrences. Anomalies in the signal shape as illustrated by the third peak cause a measurement error of $\Delta\tau$. f_0 is the signal frequency.

shift. Fluctuations in the pulse height can be compensated with a constant fraction discriminator and therefore do not contribute to $\Delta\tau$, but deformed pulses of the same height cannot be compensated in this manner.

One such measurement (i.e. one turn of the bunch) may not provide the required precision for several reasons. The most important are changing signal shapes and subsequently shifted triggers and the limited maximum counter frequency.

Averaging over a period T, corresponding to $N = T\hat{f}$ measurements, allows for a determination of the mean frequency $\bar{f}$ that is more precise than each single measurement. If the involved errors are assumed to be normally distributed, the error of the mean frequency is given by

$$\Delta\bar{f}^2 = \frac{1}{N}\Delta f^2 = \frac{f}{T}\left[\left(\frac{\Delta f_c}{f_c}\right)^2 + \left(\frac{f}{f_c}\right)^2(1 + \Delta\tau f_c)^2\right] \qquad (3.36)$$

where the approximation $N \approx Tf$ was used and n was replaced by f_c/f. To compare it with the observation period (3.29) of the Fourier transform measurement, equation (3.36) can be rewritten to

$$T \geq \frac{f}{\Delta\bar{f}^2}\left[\left(\frac{\Delta f_c}{f_c}\right)^2 + \left(\frac{f}{f_c}\right)^2(1 + \Delta\tau f_c)^2\right] \qquad (3.37)$$

Under the assumption that the absolute error of the Fourier transform measurement is approximately equal its resolution, direct comparison with equation (3.29) allows to

Particle type	Energy	Counter jitter	Trigger jitter
Protons	60 MeV	25 ‰	17.7 ns
Protons	250 MeV	18 ‰	6.5 ns
Carbon	120 MeV/n	42 ‰	22.2 ns
Carbon	400 MeV/n	11 ‰	2.9 ns

Table 3.4.: Maximum values of the relative jitter of an RF counter and the associated trigger below which the RF counter measurement outperforms the Fourier transform measurement. The counter frequency is assumed to be 1 GHz, which seems to be a common value. Higher counter frequencies increase the given limits only a little.

investigate under which conditions the RF counter measurement method is advantageous (i.e. faster than the Fourier transform method at the same precision). If regarded independently, the maximum trigger jitter the maximum counter jitter are:

$$\Delta\tau < \sqrt{\frac{\Delta f}{f} - \frac{1}{f_c}} \qquad (3.38)$$

$$\frac{\Delta f_c}{f_c} < \sqrt{\frac{\Delta f}{f} - \left(\frac{f}{f_c}\right)^2} \qquad (3.39)$$

Obviously it depends on the specific requirements which method suits best. Table 3.4 lists the maximum relative counter jitter and the trigger jitter values below which the RF counter measurement method outperforms the Fourier transform method described in section 3.3.1.

3.4. Measurement performance

The performance of the measurement described above is completely characterised by the following properties, which are discussed in subsequent subsections:

- Energy measurement accuracy

- Energy measurement precision

- Energy measurement resolution

- Temporal measurement resolution (i.e. measurement speed)

These are in contrast to the properties of the measurement method and procedure, like availability, reliability and maintainability, which are discussed in section 1.4.

3.4.1. Energy accuracy

The accuracy of the described time-of-flight measurement is determined by the accuracy of the parameters presented in table 3.5. At least the reference orbit circumference C_0 is subject to calibration. Therefore the achieved energy accuracy will be equivalent to the calibration accuracy. The calibration accuracy obviously depends on the calibration procedure, which will be elaborated at a later time.

Parameter name	Symbol
Reference orbit circumference	C_0
Magnetic length of the dipoles	ℓ
Bending radius of the dipoles for the reference orbit	ρ_0
Beam position measurement ($i = 1 \dots N$)	x_i
Radio-frequency	f

Table 3.5.: Parameters whose accuracy determines the accuracy of the energy measurement.

Although *no value for the energy accuracy can be given at this time*, it is expected that sufficient accuracy can be achieved by calibration with treatment verification devices (e.g. water phantom measurement).

3.4.2. Energy precision

The precision of the described time-of-flight measurement is determined by the precision of

- the circumference measurement and

- the revolution frequency measurement.

The relation between the precision of these two measurements and the energy precision is given in first order by propagation of uncertainty:

$$\Delta E_k^2 = \left| \frac{\partial E_k}{\partial C} \right|^2 \Delta C^2 + \left| \frac{\partial E_k}{\partial f} \right|^2 \Delta f^2 \tag{3.40}$$

With equations (3.1 to 3.3), the partial derivatives can be evaluated to

$$\frac{\partial E_k}{\partial C} = \frac{\partial E_k}{\partial v} \frac{\partial v}{\partial C} = mc\gamma^3 \beta f \qquad \text{and} \qquad \frac{\partial E_k}{\partial f} = \frac{\partial E_k}{\partial v} \frac{\partial v}{\partial f} = mc\gamma^3 \beta C \tag{3.41}$$

Substituting them in equation (3.40) and taking the square root yields

$$\Delta E_k = mc\gamma^3 \beta \sqrt{f^2 \Delta C^2 + C^2 \Delta f^2} \tag{3.42}$$

For easier comparison between the different energies, this can be rewritten for relative errors as
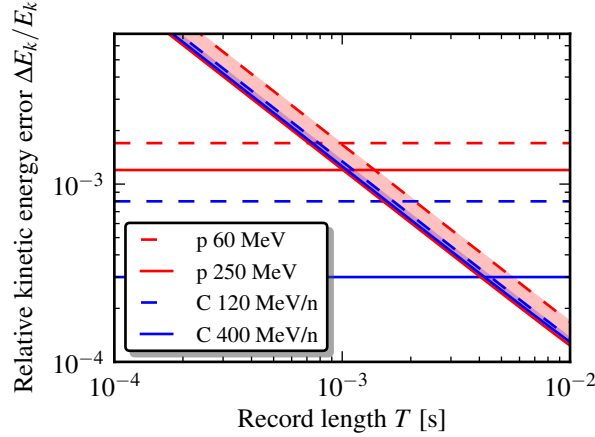
Figure 3.11.: Diagram showing the relation between sampling time of a Fourier transform radio-frequency measurement and the relative precision of the kinetic energy measurement with $\Delta f = 1/T$ as per equation (3.29) and $\sigma_{xy} = 0.4\,\text{mm}$. The red zone indicates the different proton energies while the blue zone indicates the different carbon energies. The horizontal lines indicate the preliminary energy verification requirements for the energy limits of both protons and carbon ions.

$$\frac{\Delta E_k}{E_k} = \gamma\,(\gamma + 1)\sqrt{\frac{\Delta C^2}{C^2} + \frac{\Delta f^2}{f^2}} \tag{3.43}$$

Finally substituting the approximations for the uncertainties of the circumference and frequency measurement found earlier, i.e. (3.26) and (3.29) respectively, yields

$$\frac{\Delta E_k}{E_k} = \gamma\,(\gamma + 1)\sqrt{\frac{(1.67\Delta x)^2}{C^2} + \frac{1}{T^2 f^2}} \tag{3.44}$$

where Δx is the uncertainty of the beam position measurements (both horizontal and vertical) and T is the record length used for the Fourier transform.

3.4.3. Energy and temporal resolution

Both, the energy resolution and the temporal resolution of the time-of-flight measurement are determined by the duration of the measurement. The influence of the BPM resolution on the energy resolution is small compared to the frequency resolution.

An exceptionally long duration of the frequency measurement slows down each cylce and can therefore prolong the treatment duration. The diagram in figure 3.11 shows the influence of the record length of the frequency measurement on the relative energy error as given by equation (3.44). From the crossings of the horizontal lines, which indicate

the requirements for the energy limits of both protons and carbon ions, the necessary record length to achieve the required precision reads to

$$T \geq 1\,\mathrm{ms} \tag{3.45}$$

for protons. To achieve the required precision for high energy carbon ions, $4.4\,\mathrm{ms}$ record length are necessary.

3.5. Energy spread

The measurement described so far does not measure all the particle energies, but rather the beam energy. To describe the significance of the beam energy with respect to the particle energies, the energy distribution needs to be known. The most important measure for the energy distribution apart from the location given by the mean energy, is the width given by the energy spread.

In a synchrotron, one possibility to measure the energy spread is by means of a Schottky noise measurement [19]. This measurement achieves useful precision only for an unbunched beam. Because the beam energy measurement requires a bunched beam, the two measurements can not be performed in parallel.

The Schottky noise measurement determines the bandwidth B_f of the revolution frequencies of the particles is the beam

$$B_f = n f_\mathrm{rev} \eta \frac{\Delta p}{p} \tag{3.46}$$

where n is the harmonic of which the bandwidth is being measured, f_rev is the average revolution frequency and $\eta = 1/\gamma_t^2 - 1/\gamma^2$ with the machine parameter γ_t.

The error of this measurement concerning the energy spread is determined by the highest usable harmonic and the performance of the FFT. At MedAustron, the highest harmonic n that contains enough power to be measured, is $n = 4$ and the FFT performance is assumed (recent design) to provide a bandwidth resolution of $\Delta B_f = 250\,\mathrm{Hz}$.

3.6. Résumé

Putting in the numbers for the energy limits of protons and carbon ions, yields the performance results presented in table 3.6 under the following assumptions:

- Beam position monitor uncertainty (horizontal and vertical) $\Delta x = 0.4\,\mathrm{mm}$

- Revolution frequency measurement by Fourier transform

- Pick-up signal sampling frequency $f_\mathrm{s} > 5.6\,\mathrm{MHz}$

- Pick-up signal observation period $T = 5\,\mathrm{ms}$
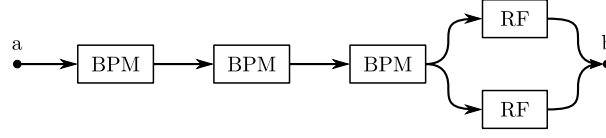
- Schottky noise harmonic $n = 4$

Figure 3.12.: Chain of components that contribute to the total availability of the system. Point a indicates the start of the measurement and point b indicates the successfully obtained beam energy. Each step to the next component in the chain can only be successful if the connecting component is available.

- Schottky noise bandwidth resolution $\Delta B_f = 250\,\mathrm{Hz}$

Particle type	Energy	ToF precision	Schottky precision
Protons	$60\,\mathrm{MeV}$	$22\,\mathrm{keV}$	$9\,\mathrm{keV}$
Protons	$250\,\mathrm{MeV}$	$67\,\mathrm{keV}$	$32\,\mathrm{keV}$
Carbon ions	$120\,\mathrm{MeV/n}$	$35\,\mathrm{keV/n}$	$15\,\mathrm{keV/n}$
Carbon ions	$400\,\mathrm{MeV/n}$	$113\,\mathrm{keV/n}$	$66\,\mathrm{keV/n}$

Table 3.6.: Measurement performances for different particles and kinetic energies achieved by the measurement methods described in section 3.1.

3.7. Availability and risk assessment

3.7.1. System modelling

Figure 3.12 shows a simplified model of a system for energy verification in a synchrotron using a time-of-flight measurement. It should be emphasised that the beam position measurements are indicated as serial components while the RF measurements are redundant (if more than one is implemented). This is because each of the them delivers the full required measurement performance, while the circumference measurement performance may suffer severely even with only one failing BPM as indicated in table 3.7.

To derive the availability of the system from the availability of its components, it suffices to apply the basic laws of probability theory. Assuming that the availability of each component is independent yields the following equation:

$$A_{\mathrm{total}} = \left[1 - (1 - A_{\mathrm{RF}})^N\right] A_{\mathrm{BPM}}^M \tag{3.47}$$

where A_{RF} is the availability of each single frequency measurement according to equation (1.1), N is the number of redundant frequency measurements, A_{BPM} is the availability of each BPM and M is the number of BPMs. At MedAustron, the number of horizontal BPMs is $M = 11$. If one or two vertical BPMs fail, the performance of the closed orbit circumference measurement remains acceptable. Such failures are therefore ignored in this model.

3.7.2. Numbers

It has been hinted already above, that in order to calculate the availability of the synchrotron energy verification that can realistically be expected, the following information is required:

- Availability of the horizontal BPMs A_{BPM} (because each single failure leads to a system failure, eventual dependencies between them are not important)

- Availability of the frequency measurement A_{RF}

- In case of redundant frequency measurements, number and conditional availability of each measurement.

∩	0	1	2	3	4	5	6	7	8	9	10	11
0	0.54	0.64	3.48	2.12	**4.42**	0.66	0.65	3.31	0.57	0.57	3.38	0.62
1			5.07	1.98	4.45	0.80	0.77	3.38	0.65	0.63	3.37	1.50
2				6.94	1.96	3.50	3.56	6.25	3.52	3.39	2.36	3.51
3					**7.67**	1.96	2.05	3.88	2.23	2.19	3.58	2.04
4						6.33	4.40	2.65	4.34	4.48	7.55	4.46
5							1.79	3.28	0.65	0.67	3.49	0.77
6								4.76	0.63	0.63	3.41	0.76
7									3.85	3.20	1.68	3.36
8										2.38	3.27	0.61
9											3.95	0.59
10												5.05

Table 3.7.: Circumference measurement performance in terms of uncertainty in millimeters as a function of failed horizontal BPMs. The columns and rows are the BPM indices from 1 to 11. The index 0 denotes the situation where all BPMs are working (top left cell) or where only one BPM failed (top row). The values are results from a simulation of 1000 closed orbit measurements with random errors within their specifications on all magnetic elements.

4. Depth-dose Measurement

In contrast to the time-of-flight measurement described in chapter 3, which is based on measurements of collective properties like the beam position and the bunch revolution frequency, the measurement principle developed during this thesis and described in this chapter is capable of exploiting single-particle properties. In that respect it is similar to calorimeters commonly used in high-energy physics experiments. On the other hand there are two points which set it apart from usual calorimeters and require reconsideration of some of the common calorimetry concepts:

- The position and angle of all incoming particles is effectively the same, as they originate from a particle beam rather than a collision or a decay.

- For one measurement, all particles are drawn from the same narrow ($\Delta E/E \approx 4\,\text{‰}$) energy distribution.

- The expected outcome is not an energy, but a decision.

The second point deserves some emphasis. It is evident once the ultimate purpose of any measurement proposed here is considered. That is, a decision whether a given set of data indicates a correct or an incorrect ion beam energy. As it will be pointed out in detail in section 2.4, the detector developed and described in the following is not designed to measure the energy of any given beam. Instead it compares the detector response of the beam produced during medical operation (of which the energy needs to be verified) to a previously recorded detector response (e.g. recorded and verified during commissioning with a dosimeter inside a water phantom). If the comparison fails, i.e. if the observed energy does not match the expected energy, the beam is rejected. Hence, it is not necessary to know the value of the incorrect energy if it can be recognised as being incorrect otherwise.

Other than any measurement done prior to extraction - like the time-of-flight measurement from chapter 3 - the measurement described here concerns the extracted beam. Hence, it does not need to make assumptions about energy changes during extraction and can even detect unexpected behaviour during the extraction.

4.1. Location

To decide on a suitable detector technology, it must be clear under which circumstances the detector has to operate. While some are quiet common, like room temperature and atmospheric pressure, others are rather unusual, like maximum detector size and radiation. It turned out that at MedAustron, the hardest requirements are those of

limited available space and radiation hardness. Both depend on the location at which a device may be integrated into the particle accelerator.

4.1.1. Available space

The most obvious location for a destructive measurement in the High Energy Beam Transfer line (HEBT) is the chopper dump. At the beginning of each extraction the beam is dumped there for the first 100 ms to qualify the beam profile and intensity[1], but also to await stable beam conditions. Therefore, although the measurement is destructive, no additional beam is lost.

The chopper system allows switching the beam on and off rapidly (the maximum switch time is $300\,\mu$s). Its purpose is to accurately control irradiation times, but also to switch off the beam in case of errors. As shown in figure 4.1, it consists of four fast kicker magnets and a dump. The design is fail-safe, because the power-off state of the kicker magnets corresponds to a beam dump.

In the power-on state, the kicker magnets guide the beam around the dump by a horizontal shift of about 14 mm as indicated by the dashed line in figure 4.1b. The fixed size of this shift results in a limitation for the horizontal dimensions of a detector system placed in front of the dump. It must not extend more than 7 mm from the undeflected beam axis in the direction of the passing beam. Vertically, no such limitation exists.

It is proposed that the detector replaces the first part of the chopper dump. Since it requires more space due to the lower density of detector elements compared to the dump material, the total length must be increased. This position features the advantage that one device can be used for all four irradiation rooms.

The already mentioned limit in horizontal space of maximum 7 mm off the beam axis rules out the use of traditional calorimeter materials, because they would not be able to confine the beam particles' scattering sufficiently, especially at high beam energies, rendering an energy measurement impossible.

4.1.2. Radiation Hardness

The critical quantity when regarding radiation hardness is the integrated dose deposited in the active detector volume because this determines the frequency at which the detector or parts thereof must be replaced to guarantee continuous performance. Of course, low maintainance solutions (frequencies in the order of months or years) are favourable.

The integrated dose depends on several parameters:

- The number of particles per measurement

- The number of measurements per year

---

[1] The qualification monitor qualifies the beam profile and intensity after the extraction has started and before the beam is directed around the chopper dump and towards the patient. Unlike the energy verification, the qualification monitor is only a redundant addition to the nozzle monitors which serve the same purpose.
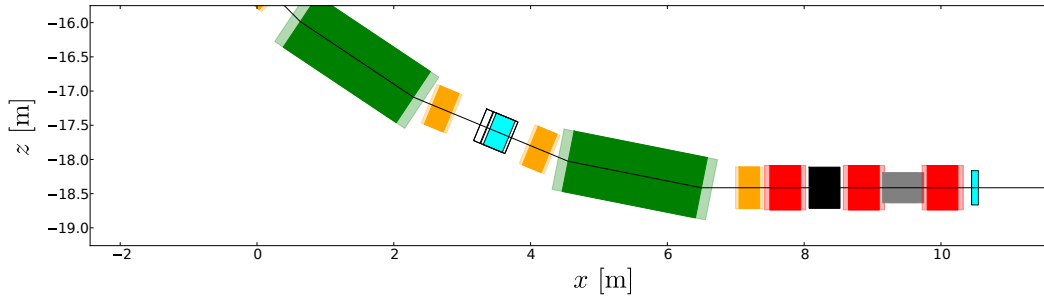
(a) Section of the HEBT layout. The two large green rectangles indicate dipole magnets. The four smaller orange rectangles correspond to the fast kicker magnets of the chopper system (only a small corner is displayed of the first kicker in the top left corner). The cyan rectangle indicates the chopper dump. The red rectangles indicate quadrupole magnets..
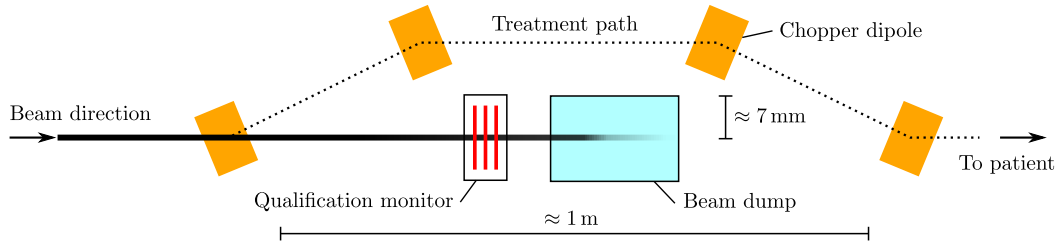
(b) Schematic layout of the chopper system with alternating beam paths and rough indications of dimensions (not to scale).

Figure 4.1.: Chopper region in the MedAustron HEBT.

Fitted horizontal geometric emittance (energy independent)	
Horizontal Beta function	2.433 m
Horizontal full beam width	4 mm
Normalised vertical RMS emittance for protons	$0.519\,\pi$ mm mrad
Normalised vertical RMS emittance for carbon ions	$0.748\,\pi$ mm mrad
Vertical RMS geometric emittance for 60 MeV protons	$1.43\,\pi$ mm mrad
Vertical RMS geometric emittance for 250 MeV protons	$0.668\,\pi$ mm mrad
Vertical RMS geometric emittance for 120 MeV/n carbon ions	$1.43\,\pi$ mm mrad
Vertical RMS geometric emittance for 400 MeV/n carbon ions	$0.733\,\pi$ mm mrad
Vertical Beta function	1.363 m
Vertical RMS beam width for protons	$0.538 - 0.788$ mm
Vertical RMS beam width for carbon ions	$0.564 - 0.788$ mm

Table 4.1.: Beam profile on the MedAustron chopper dump [29].

- The beam profile, i.e. the transverse distribution of the incident particles

- The configuration of passive detector elements (e.g. the number and size of range shifter steps)

Naturally, without a detailed design of the detector, the expected annual dose can only be an approximation. Due to the extraction mechanism used at MedAustron (see section 2.5.2), the beam in the horizontal phase-space has the shape of a "bar-of-charge" (i.e. approximately uniform) with a geometric emittance that is independet of energy and particle. In the vertical plane the beam profile is approximately Gaussian and varies in size depending on the particle type and energy due to adiabatic damping. Table 4.1 lists the beam profile characteristics on the chopper dump. As a speciality, the MedAustron accelerator will also be operated with protons at an energy of 800 MeV, but in this case the chopper is activated at all times and no beam dumps are foreseen. Nevertheless, the detector must withstand occasional single shots at this energy in case of unplanned beam dumps.

The number of particles that hit the chopper dump per year during medical operation is estimated to 2.1×10^{14} protons and ten times less carbon ions.

For the approximation of the radiation, it is assumed that on average all energies are used equally often. Figure 4.2 shows the resulting annual dose distribution on the chopper dump. The maximum dose of about $7\,\mathrm{MGy/year}$ is deposited at the location of the Bragg peak of the lowest particle energy since particles with higher energies also deposit energy in the entrance channel. If a range shifter is used to always shift the Bragg peak to the same detector position, the dose maxima (shown in figure 4.3) are effectively integrated and the resulting worst-case dose is about 26 MGy/year. Both of the given dose values are upper limits assumed in order to guide the decision for a detector technology. The expected dose in the detector depends to a large extent on the final detector design and will therefore be evaluated later (see section 4.6.11).
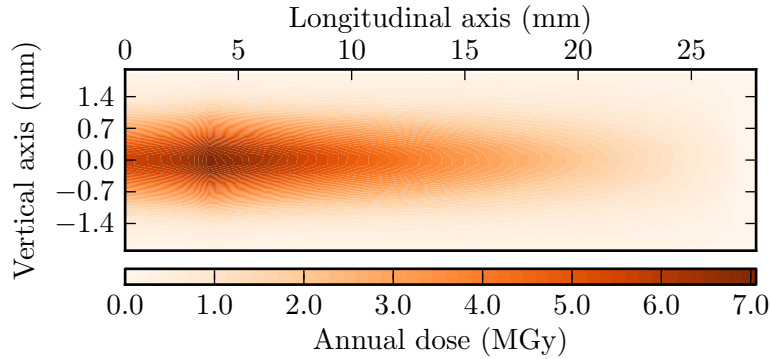
Figure 4.2.: Vertical cut through the center ($x = 0\,\mathrm{mm}$) of the chopper dump showing the dose deposited during one year of irradiation. The Gaussian beam profile on the vertical axis is clearly visible. The dose maximum is located close to the entrance channel on the left which is shared by all particles. The dose decreases with increasing depth because the number of particles with the required range decreases, but also due to transverse blow-up of the beam.

4.2. Diamond detectors

4.2.1. Rationale

The requirements on the detector material do not only include an extraordinary radiation hardness, but also measurement speed and ease of mechanical handling. A few promising candidates are:

- Water calorimeters, measuring the temperature change induced by the ion beam in a water tank, are obviously too slow for energy verification.

- Low-temperature calorimeters as well as organic liquids require significant engineering effort and maintenance which is not acceptable in a commercial, low maintenance environment like MedAustron.

- Most of the more common high-energy physics calorimeters, even the most radiation hard inorganic crystals (e.g. $PbWO_4$), do not provide the required radiation hardness (as they are designed for secondary particles and not for primary beam particles).

- The only remaining option are ionisation detectors.

While gaseous detectors are superior regarding radiation hardness, solid-state detectors require less space and provide a higher sampling ratio and thus better energy resolution. Among solid-state detectors, silicon devices achieve unprecedented energy resolution due
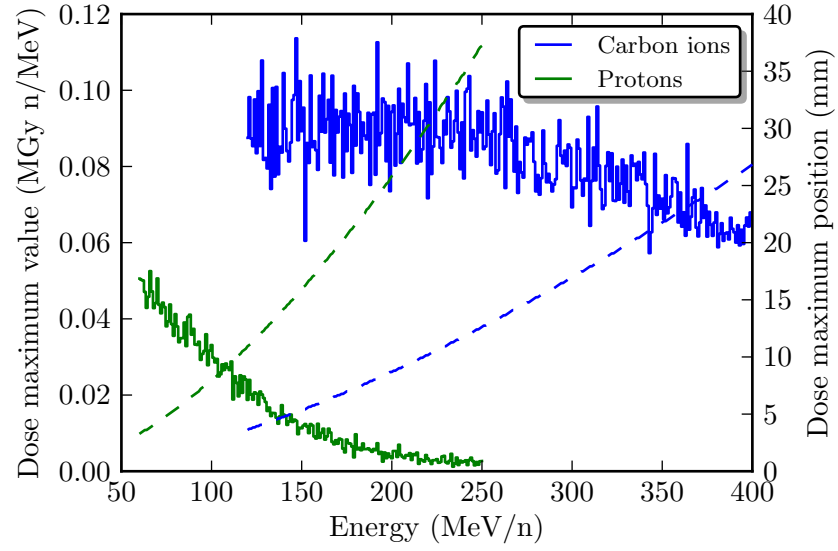
Figure 4.3.: Value and position of the dose maximum for both particle types and various energies. The difference between protons and carbon ions is due to the sharper Bragg peak of the carbon ions and the stronger beam blow up for protons. The dashed lines indicate the position of the Bragg peak (right vertical axis) while the solid lines indicate the dose (i.e. the peak height) at those positions. The fluctuations are due to the limited simulation volume and the binning of the positions, where the latter effect is more important for carbon ions as the peak width is in the same order of magnitude as the bin width.

to their small band-gap, but suffer greatly from radiation damage effects. A material with a higher band-gap, and thus more favourable balance between radiation hardness and energy resolution, is diamond. The difference in radiation hardness between silicon and diamond sensors is approximately a factor of 3.6 [26].

Table 4.2 summarizes the most important parameters of Chemical Vapor Deposition (CVD) diamonds [57]. The average energy to create an e-h pair is low compared to the deposited energy (by about 5 orders of magnitude), which results in a large number of generated charge carriers (see section 4.2.2 below). The high thermal conductivity combined with the small lattice constant[2] are crucial for the radiation hardness since energy deposited to the lattice can be distributed easily and at the same time it needs a high energy density to damage the lattice. A maximum acceptable integrated dose can not be given universally, because it depends on the intended application (e.g. a detector used merely to provide a trigger when a particle goes through is more radiation hard than a detector used to quantify the deposited energy). The electrical properties like high resistivity, low capacitance and high carrier mobility allow for a fast readout in the order of nanoseconds [41] and are responsible for a good Charge Collection Efficiency (CCE) (see section 4.2.3 below).

Property	Diamond
Band gap	$5.45\,\mathrm{eV}$
Energy to create e-h pair	$13\,\mathrm{eV}$
Electron mobility	$4500\,\mathrm{cm^2/V\,s}$
Hole mobility	$2750\,\mathrm{cm^2/V\,s}$
Breakdown field	$10^7\,\mathrm{Vm}$
Resistivity	$\gtrsim 10^{13}\,\Omega\,\mathrm{cm}$
Dielectric constant	5.7
Thermal conductivity	$20\,\mathrm{W/cm\,K}$
Lattice constant	$3.57\,\mathrm{\AA}$

Table 4.2.: The most important parameters of single-crystal CVD diamonds [70].

4.2.2. Charge generation

At the energies used for ion beam therapy, ions lose energy in a medium primarily through interactions with atomic lattice electrons, in particular excitation and ionisation. Inelastic nuclear interactions become relevant only at the highest energies used for ion beam therapy, i.e. $250\,\mathrm{MeV}$ protons or $400\,\mathrm{MeV/n}$ carbon ions, releasing secondary particles, in particular neutrons [21]. The energy transferred by elastic nuclear collisions becomes relevant only at proton energies below $20\,\mathrm{keV}$ [47]. Thus, when accounting for primary and secondary particles, over $99.9\,\%$ of the total energy deposited by protons and car-

---

[2]The smaller the lattice constant, the higher is the threshold energy of defect formation [52] and thus the higher the radiation hardness.
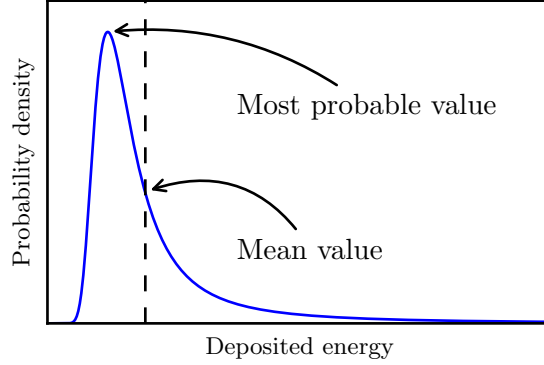
Figure 4.4.: Shape of the Landau distribution. A mean value only exists for a truncated Landau distribution (the mean value indicated in the plot is evaluated inside the plotted region). Without a cut, the mean of the Landau distribution is not well defined.

bon ions[3] is converted to ionisation energy in the target medium. This conversion from kinetic energy to ionisation energy and consequently to generated charge forms the basis of the working principle of any solid-state ionisation chamber.

The Bethe equation and its several corrections [61] allow to quantify this energy conversion by describing the *mean* differential energy loss, or stopping power, of a charged particle in matter as a function of its kinetic energy. Due to the long-tailed asymmetric Landau distribution [51, 37] this mean value can be misleading for thin layers of material, as it is considerably above the most probable energy deposit (see figure 4.4).

Since the amount of generated charge is directly proportional to the deposited energy, it also follows the Landau distribution. The proportional factor between deposited energy and generated charge is determined by the average energy consumed to create an electron-hole pair (see table 4.2). Although the energy to create an electron-hole pair is a stochastic quantity itself with the band gap being the lower limit, the high number of processes makes the related variance effectively negligible for the energies and layer thickness concerned in this work.

In summary, the number of generated charges can be computed by simply dividing the deposited energy by the average energy needed to create an electron-hole pair and it follows a Landau distribution .

---

[3] At low energies (60 MeV protons or 120 MeV/n carbon ions), the stopping power is directly going into ionisation energy, while at high energies (250 MeV protons or 400 MeV/n carbon ions), the stopping power is partly due to inelastic nuclear interactions yielding secondary particles, but also the secondaries are stopped in the medium and cause ionisation.

4.2.3. Charge collection

After the electron-hole pairs have been generated, they must be separated in an electric field in order to measure them. Their drift in the electric field induces a current and the electric signal is obtained by measuring this current [85]. Therefore the signal depends on the drift length of the charge carriers, which is limited by their lifetime and velocity. For spectroscopy, i.e. to determine the deposited energy, the total generated charge must be obtained by integrating the signal. If the lifetime of the charge carriers is much longer than their drift time in the sensitive volume, the integrated current is equal to the number of generated electron-hole pairs. In this ideal case, the CCE defined as the ratio between collected and generated charge ($CCE = Q_{collected}/Q_{generated}$) is 100 %. To achieve this goal, the charge carrier lifetime and drift velocity must be sufficiently high.

The drift velocity increases as a function of the electric field strength E (i.e. the applied voltage), but the collected charge saturates at high E ($\approx 0.3\,\mathrm{V}/\mu\mathrm{m}$) due to scattering processes. The proportional factor between the field strength and the observed drift velocity is called "mobility". It is differentiated between electron mobility and hole mobility as two distinct material properties (see table 4.2).

The charge carrier lifetime on the other hand is limited by two processes: charge trapping[4] and recombination [71]. Due to the wide band-gap, direct band-to-band recombination is negligible in diamond and the lifetime is limited mainly by trapping and trap assisted recombination. The trapping time (and consequently the charge carrier lifetime) depends on the type and density of defects in the sensitive volume and on the thermal velocity of the carriers.

Among the different types of artificial diamond available today, single-crystal CVD diamonds are the only ones to achieve close to 100 % CCE [17] due to the highest mobilities and least defects. Therefore only this type is suitable for spectroscopy.

4.2.4. Radiation damage effects and annealing

Unfortunately, not the entire deposited energy is converted to ionisation energy, but a small fraction (below 0.1 %, see section 4.2.2) is absorbed in inelastic interactions with the nuclei of the diamond lattice. Despite the high displacement energy ($43\,\mathrm{eV}$ compared to $13 - 20\,\mathrm{eV}$ for silicon), a small probability remains that radiation causes local damage of the lattice structure. These lattice defects can act as traps for free charge carriers (electrons or holes), capturing them for a duration which depends on the energy level of the trap and the temperature of the detector. The emission rate per volume is proportional to the inverse trapping duration and given by

$$r_{re} = s n_f \exp\left(-\frac{E_a}{kT}\right)$$

---

[4]Lattice defects (e.g. vacancies or impurities) locally introduce additional energy levels into the band gap. If such an energy level is close to the conduction band, it is practically not occupied at room temperature and can trap an otherwise mobile charge. A trapped charge can be thermally re-emitted after some time depending on the temperature and the energy level of the trap.

where s is typically in the range of $10^{12}\,\text{s}^{-1}$ to $10^{14}\,\text{s}^{-1}$ for diamond, n_f is the density of occupied traps, E_a is the "depth" of the trap, i.e. the distance to the conduction or the valence band, k is the Boltzmann constant and T is the temperature. The generated traps can have two effects:

- As explained in the previous subsection, the charge trapping leads to a degraded CCE and leads to incorrect measurement results. The influence of traps on the CCE is especially visible after some time without irradiation because in the latter case, the lattice is in equilibrium and the traps next to the conduction band are unoccupied. To counteract the influence of traps, they can be filled at the beginning of the detector operation by "priming", i.e. homogeneous irradiation of the sensitive volume with moderately ionising radiation [23].

- Apart from trapping generated free charge carriers and assisting recombination, traps can cause internal inhomogeneous polarisation of the sensitive volume. This polarisation is induced by the non-uniform space charge due to the external electric field, i.e. the probability of an electron to get trapped near the anode is much higher than near the cathode when assuming uniform production of electron-hole pairs. The resulting polarisation is a function of trap density, applied voltage, signal rate and time. It can significantly reduce the CCE above a total applied dose in the order of MGy, but can largely be avoided by a frequently changing detector polarity [82].

Fortunately, the degradation due to lattice displacements can almost entirely be recovered by high-temperature annealing [71]. Contrary to silicon detectors, diamond detectors do not show an increase in leakage current with continued irradiation and can thus be operated at high voltages continuously without cooling or special treatment.

4.2.5. Signal processing

The signal processing of a diamond detector when targeting high-precision energy measurements (as opposed to trigger functions - also when used in a detector array to achieve position resolution) is done by charge sensitive electronics, i.e. the detector is DC coupled to a low noise charge sensitive amplifier fully integrating the detector current. For an example of further processing see [71, section 6.3.1]. The electronic noise of the system is decisive for the achieved energy resolution. Also, lower noise improves the radiation hardness, because an acceptable Signal-to-Noise Ratio (SNR) can be maintained as signal levels decrease. Noise levels within a few hundred e^- – corresponding to a SNR of the order of 10^3 – have been reported [71, 86]. To evaluate the noise contribution, detailed knowledge of the electronics must be provided e.g. to be used in a SPICE simulation. To limit the scope of this thesis, the detector performance shall be estimated by signal equivalent noise measures given in the next subsection.

4.2.6. Achievable energy precision

The per-event energy precision of the detector is a function of the statistical fluctuations of the charge generation process, the uncertainty related to the CCE and the electronic noise of the signal processing. For single crystal diamond layers of 0.5 mm thickness in terms of signal equivalent noise, a precision of 20.5 keV has been reported for 5.5 MeV alpha particles [71] (equivalent to $5.2\,\mathrm{keV/n}$ or 0.4 %) and a precision of 140 keV has been reported for 22.8 MeV carbon ions [41] (equivalent to $11.7\,\mathrm{keV/n}$ or 0.6 %). Both measurements do not regard the Minimum Ionising Particle (MIP), but neither will a detector used for energy verification. The simulations described in this chapter use a relative energy error of 1 % in all cases.

4.3. Simulation

4.3.1. Simulation tool-chain

The detector design described in section 4.5 and the following is the result of several design iterations. At each step, the detector performance has been evaluated based on simulations. These simulations have been performed using two Monte Carlo codes developed at CERN, namely Fluka [34, 16] and Geant4 [9]. These codes were used via a dedicated detector simulation framework developed by the author. This framework is written in Python [87] and specifically tailored for the simulation and processing of a single layer-stack style detector.

The rationale for implementing such a framework was to provide a plug-in system for data processing and visualisation. It enforces a unified data interface among all tasks and minimises duplication of "bookkeeping" code (parsing configuration and command line parameters, accessing data, error handling, logging system) by moving this code into the framework and thus separating it from the data processing. Each of the plug-ins provides one function for data processing and one for data visualisation. Apart from the mentioned bookkeeping tasks, the implemented framework also has the ability to configure and run (even in parallel on machines with multiple processors) multiple Fluka and Geant4 simulation jobs. Finally it also manages the configuration of the plotting environment Matplotlib [44].

The storage format for simulation results was chosen to be HDF5 [42], a standardised file format specifically designed for large structured numerical datasets and optimised for fast access. The PyTables [10] module for Python fully exploits these advantages, i.e. fast access to huge datasets or subsets thereof, using and providing the Numpy [13, 31] conventions for indexing and in-memory data.

The Fluka runs are configured via an input file template filled with parameters from the framework configuration. To precisely simulate the beam conditions (i.e. the beam profile in horizontal and vertical plane as well as the particle energy distribution), a custom source routine has been implemented in Fortran. The simulation framework spawns a Fluka sub-process for each configuration and waits for its completion before accessing the results. Afterwards, the Fluka output is parsed into a Python format for

	Duration	Protons	Carbon ions
Qualification	50 ms	5×10^6	2×10^5
Verification (1 %)	1 ms	1000	40

Table 4.3.: Maximum number of particles available per measurement at minimum beam intensity corresponding to the requirements listed in section 2.3.

further processing.

For the Geant4 simulations, a separate C++ application had to be written since Geant4 is a tool-kit and not itself an application. The implemented Geant4 application sets up the geometry and provides macro interfaces (Geant4 Messengers) to configure the detector parameters in detail. It also contains a realistic model of the beam conditions, i.e. beam profile and energy spread. The results returned by the Geant4 routines are immediately written to HDF5 files, skipping one conversion step compared to the Fluka runs. The Geant4 physics list used was "QGSP_BIC_EMY", which is also used by the hadrontherapy application deployed with Geant4 [24].

4.3.2. Simulation volume

The number of incoming primary particles has a significant impact on the precision of the obtained measurement result. On the one hand, more particles improve the measurement precision. On the other hand, if less particles are necessary, a decision can be taken faster and more particles of each spill are left to be used for treatment purposes. In order to be able to characterise the statistical performance of a single measurement, it is necessary to simulate a large number (at least 1000) of measurements. The number of particles per measurement is determined by the measurement type.

A qualification measurement (see section 2.3 for the difference between qualification and verification) can absorb the entire available beam intensity during a small part of the cycle. In this case, the minimum number of primary particles per measurement can be computed from the measurement duration and the minimum beam intensity (see table 4.3).

In case of synchronous verification (see section 4.7), the measurement may absorb only a small fraction of the total beam intensity. In that case one measurement per spot would be desirable. Table 4.3 lists the number of particles available for each measurement if 1 % of the total beam intensity is sacrificed for energy verification.

The number of simulated primary particles per energy and particle type is the product of the particles per measurement and the number of measurements. As mentioned above, the number of measurements must be large enough to provide sufficient statistics regarding the measurement performance, i.e. since the targeted statistical error is in the range of per mill, at least a 1000 measurements must be simulated. If the total number of simulated particles is summarised in a single measurement, no information about the per-measurement statistical properties (e.g. the variance of the measured mean value)

can be obtained. In order to minimise simulation times, measurements have been simulated with fewer particles per measurement than available when the achieved performance matched the energy verification requirements 2.3 nonetheless and the sample sizes were determined by starting with the full number of available particles and only a few measurements (e.g. 100) and then reducing the number of particles per measurement while increasing the number of measurements (see section 4.6.10 for the used sample sizes). For detailed studies, simulation times can be optimised by simulating only a fraction (e.g. one tenth) of the events and "bootstrapping"[5] the required number of measurements.

4.4. Statistical tests

4.4.1. General detector concept

In order to identify or develop an adequate test statistic, an understanding of the general concept of the proposed detector and the data it generates is necessary. Figure 4.5 sketches the basic data components:

- A *score* is the energy deposited in a single layer due to a single primary particle.

- An *event* is a set of scores recorded in all layers due to a single primary particle. The number of scores contained in one event is equal to the number of layers in the detector.

- A *sample* is a set of events (each containing a set of scores as described above) recorded during a certain period of time called the sampling period. The number of events contained in one sample is called the *sample size*. The sample size is equal to the number of primary particles that traverse the detector during one sampling period. Consequently, the total number of scores in a sample is equal to the number of primary particles times the number of layers.

The result of the energy verification is obtained by testing (i.e. comparing to an expectation) a sample recorded during one qualification period using one of the tests described in the following subsection.

4.4.2. Reference sample

When the distribution of a one-sample test statistic (like the sample mean) under the null hypothesis is not known, a two-sample test statistic must be used. A two-sample test statistic uses a first or "reference" sample that has been recorded under the null hypothesis and compares this sample to a second "tested" sample.

---

[5]In this context, bootstrapping means that the measurements - which consist of a certain small number of events - are assembled by randomly picking events, i.e. the data recorded for a single primary particle, from a large "pool" of events. Consequently, events are re-used multiple times in different measurements, but each measurement will be independent because it uses a different subset of the event pool.
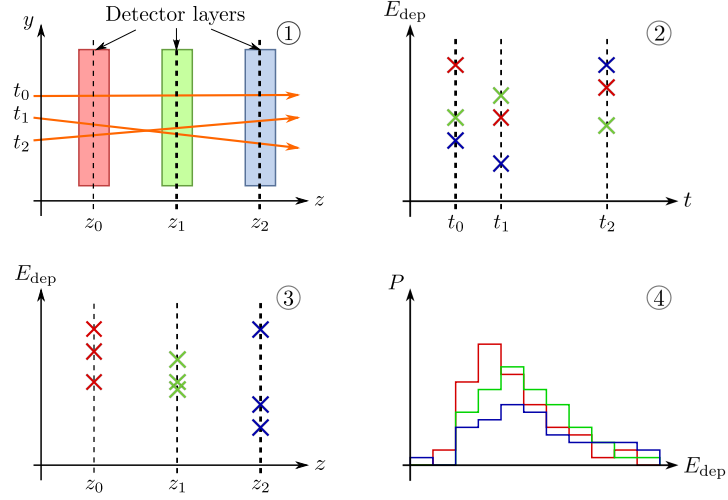
Figure 4.5.: Measurement data representations of the depth-dose measurement. Plot 1 (upper left) schematically shows three detector layers with arbitrary spacing (absorbers are not shown) and three events (particles of different energy crossing the layers), indicated by orange arrows. The three events happen at three different times t_0, t_1 and t_2 (the times each refer to one event/arrow, not to positions on the vertial axis). The propagation time between detector layers can be neglected. Plot 2 (upper right) shows the score (i.e. the deposited energy E_{dep}) in each layer for each event as a function of the time the event was recorded. The colour of each cross associates the score with the layer that recorded it. Plot 3 (lower left) summarises the events and shows the scores ordered by layer. Plot 4 (lower right) represents the same data as subfigure 3 but contains more events. It shows the score distributions per layer as histograms, which are more readable for a large number of events.
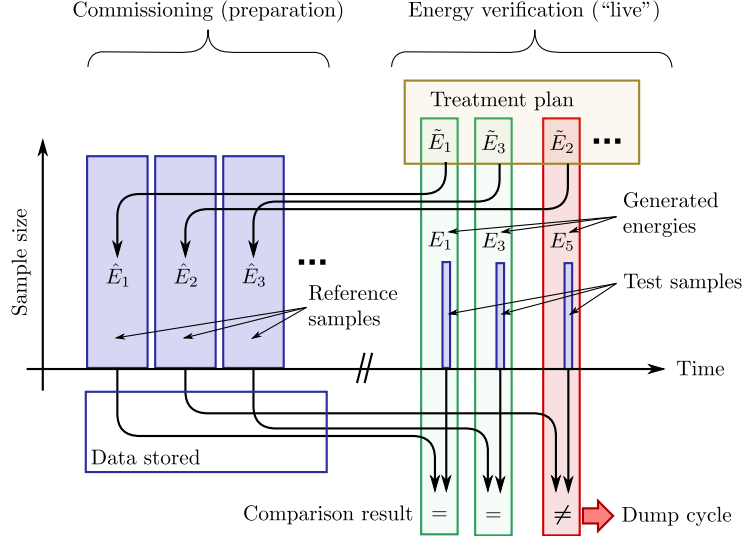
Figure 4.6.: Testing of samples against reference samples recorded during commissioning. For each beam energy E_i, a reference sample must be recorded. During energy verification, the newly recorded test samples are compared to the reference sample associated with the intended beam energy $\tilde{E}_i$. If the two samples do not match, the beam is rejected.

Figure 4.6 shows schematically how a two-sample test can be used for energy verification. Each tested sample recorded during the "live" energy verification process is compared to one reference sample recorded during commissioning. The reference sample should have at least the same size as the tested sample. In practice they should be about a factor of 10 larger in order to improve the test performance (see section 4.6.10). For each beam energy and particle type that needs to be verified, a dedicated reference sample must be recorded beforehand.

4.4.3. Derived samples

Sometimes a statistical test can not be applied to a sample directly (see 4.4.4.2 and 4.4.4.3), but may only be applied to a parameter derived from the sample e.g. the sample mean. In order to determine the propability distribution of the derived parameter for one specific case (energy & particle type), the reference sample must be partitioned in several smaller sub-samples of the same size as the tested sample and the derived parameter must be computed for each sub-sample. The resulting set of parameters (one for each sub-sample) is called the *derived sample* . The number of sub-samples is therefore equal to the *derived sample size* .

If the size of the tested sample is N_t and the size of the reference sample is N_r, the distribution of a derived parameter of the tested sample is determined by partitioning the reference sample into sub-samples of size N_t. The derived reference sample size n_r is

then given by

$$n_r = \frac{N_r}{N_t}$$

and the derived tested sample size is $n_t = N_t/N_t = 1$, i.e. this is simply the value of the parameter computed from the tested sample.

4.4.4. Statistical tests

4.4.4.1. Bragg fit

The obvious approach to data interpretation is, to fit a Bragg curve to the observed dose data. The resulting fit parameters (i.e. the parameters describing the Bragg curve - this may be one or more parameters depending on the parametrisation of the Bragg curve) are then compared to the expected values (i.e. they are tested). If the parameters do not match, the sample is rejected. Unfortunately, this test fails to detect energy errors within the required energy precision (see 2.3) for all but the most idealised situations because the Bragg curve is reproduced by the dose *means* which exhibit strong stochastic fluctuations for small samples due to the Landau distribution of the scores (see 4.5.1 for details).

4.4.4.2. Student's t test

A more general approach is to test the mean energy deposited in each layer against an expectation value determined from a reference sample (see sections 4.4.2 and 4.4.3). Since the mean is undefined for the Landau distribution, the median could be used instead, because it turns out that the distribution of the sample median is Gaussian distributed if each layer could be regarded independently. The Huber-M-estimator is also distributed normally and even shows a more narrow distribution – hence yielding better results than the median – but again only for independent layers. Both options have been included in the comparison of tests in section 4.6.1.

Establishing a test statistic across multiple layers, e.g. by summing the median deviations and testing against a χ^2 distribution, fails because the layers can not be considered statistically independent.

4.4.4.3. Hotelling's T^2 test

Hotelling's T^2 statistic is a natural extension of Student's t statistic to multiple dimensions, accounting for correlations between them, i.e. the assumption of statistical independence is not necessary anymore. The multivariate two-sample T^2 test [75] rejects the null hypothesis whenever

$$T^2 = \frac{n_t n_r}{n_t + n_r} (\bar{\mathbf{y}}_t - \bar{\mathbf{y}}_r)^T \mathbf{S}_{\mathbf{pl}}^{-1} (\bar{\mathbf{y}}_t - \bar{\mathbf{y}}_r) \geq T^2_{\alpha,p,n_t+n_r-2}. \tag{4.1}$$

As above, the indices t and r denote properties of the test sample and the reference sample respectively, n_t and n_r are the derived sample sizes (see section 4.4.3), $\bar{\mathbf{y}}_t$ and

$\bar{\mathbf{y}}_r$ are vectors containing the per-layer means and $\mathbf{S_{pl}}$ is an unbiased estimator of the common population covariance matrix. For $n_t = 1$, $\mathbf{S_{pl}}$ reduces to the sample covariance of the derived reference sample:

$$\mathbf{S}_r = \frac{1}{n_r - 1} \sum_{i=1}^{n_r} (\mathbf{y}_{r,i} - \bar{\mathbf{y}}_r)(\mathbf{y}_{r,i} - \bar{\mathbf{y}}_r)^T$$

The critical value T^2_{α,p,n_t+n_r-2} for the significance α and p dimensions can be obtained after transformation to an F statistic using

$$\frac{n_t + n_r - p - 1}{(n_t + n_r - 2)p} T^2 = F_{p,n_t+n_r-p-1}$$

which has implementations in most common statistical program libraries (e.g. `scipy.stats.f` in the Scipy Python module).

Similar to Student's t test, this test applies only to normally distributed parameters, i.e. to the medians or Huber-Ms of the deposited energies. Again, both options have been included in the comparison of tests in section 4.6.1.

4.4.4.4. Mann-Whitney-Wilcoxon test

The fact that only derived samples (see section 4.4.3) can be used with the Hotelling's T^2 test indicates a certain degree of information loss involved, as the derived samples are significantly smaller than the original samples. This information loss can be avoided by using a test which does not have the normality requirement. A few possible candidates have been investigated:

- The Kolmogorov-Smirnov test [6]

- Kuiper's test (basically a modification of the Kolmogorov-Smirnov) [7]

- The Mann-Whitney-Wilcoxon (MWW) test [93]

All three are non-parametric tests, rendering them robust against the special properties of the Landau distribution. The first two are based on distance measures between two empirical cumulative distribution functions. Since they turned out to be less powerful than the MWW test, only the latter will be explained here.

The basic idea of the MWW test is the following: When performing a common ranking of all scores of both samples, under the null hypothesis (i.e. if the energies of the two compared samples match) the sum of ranks of each sample is only a function of the sample size (e.g. it is approximately equal for equal sample sizes). The test statistic U is defined as the number of times - after a common ranking of both samples - the scores from one sample precede those from the other sample [55]. For large samples, U can be computed as

$$U_i = R_i - \frac{n_i(n_i + 1)}{2}$$

where R_i is the rank-sum of sample i and n_i is the sample size. Then each U_i is normally distributed with the following properties:

$$\mu_U = \frac{n_t n_r}{2} \quad \text{and} \quad \sigma_U = \sqrt{\frac{n_t n_r (n_t + n_r + 1)}{12}}$$

and the critical value for a given significance can be computed from the normal distribution. The test performance is compared to other tests in section 4.6.1.

4.4.4.5. Multivariate extensions of the MWW test

Unfortunately there is no obvious way to generalise the rank-sum to multiple dimensions. First a data-depth based approach[6] [54] for ranking has been tried based on the likelihood depth. The obtained power was rather disappointing not to mention the computational cost of this approach even for the most efficient depth definitions. A projection-type extension[7] of the MWW [93] finally revealed a significant improvement in terms of statistical power. The main downside was that the projection vector changes with each test sample and therefore the entire (much larger) reference sample has to be projected on each measurement, which needs significant computational effort.

It was found that this downside can be avoided by using a fixed projection vector. This vector can be obtained by "bootstrapping" samples of the size of the tested sample from the reference sample and using the mean projection vector of those samples, i.e. computing the projection vector for each bootstrapped sample and taking the mean. That way, the projection of the reference sample can be prepared and only the new measurements need to be projected before ranking them.

This approach can be further improved by a Principal Component Analysis (PCA)[8] of the reference sample and a projection of the compared samples onto the principal component. The common approach to such an analysis is to diagonalise the covariance matrix and take the eigenvector corresponding to the largest eigenvalue. For data that is not normally distributed or contains outliers, the classical covariance might be inappropriate. There are many ways around this problem that either avoid computing the covariance altogether [43] or use a different estimator. For the application at hand, the covariance has been replaced by the Minimum-Covariance Determinant (MCD) estimator, a robust

---

[6] Data-depth can be intuitively understood as the "depth" of each (multi-dimensional) data point (i.e. event) within the event "cloud" formed by all data points. A simple example is the distance of each point to the centre of mass of the cloud. Naturally, this works well only for spherical distributions. The likelihood depth is a more general approach based on the kernel density estimation of the data points.

[7] The multi-dimensional data points of each sample are projected onto a line connecting the medians of the two compared samples, effectively converting them to one-dimensional samples. In one dimension, the original MWW test can be used.

[8] PCA is a method to determine the axis along which a given dataset has the maximum variance. This axis, which can be any line in n-dimensional hyperspace for an n-dimensional dataset, is called the principal component. In 3-dimensional space this can be intuitively understood by imagening a dataset distributed within an ellipsoid of unknown orientation. A PCA then finds the principal axis of the ellipsoid, i.e. the line along which the ellipsoid has the largest extensions.
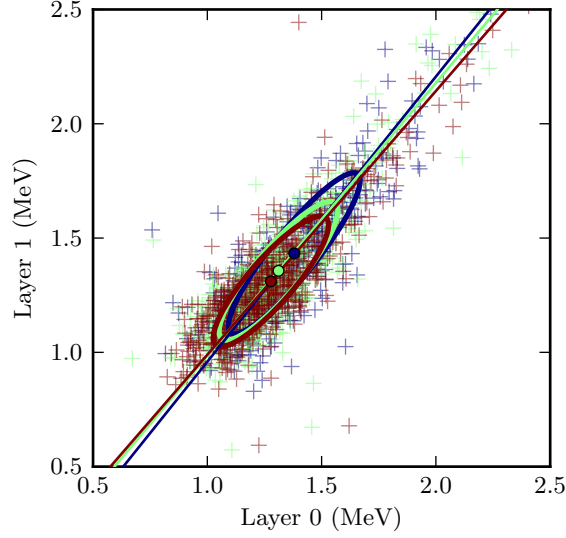
Figure 4.7.: Signal distribution for two layers and three close-by energies: 250 MeV protons in green, 249.52 MeV protons in blue and 250.48 MeV protons in red. Indicated are the estimated covariances (ellipses) and principal components (lines).

alternative of the classical covariance. This estimator is defined as the covariance of the most compact subset of the original sample, where the compactness is determined by the covariance determinant. For the sample sizes at hand, an efficient algorithm implementing this search has been used [77]. Figure 4.7 shows three two-dimensional (for two layers) signal distributions for three different but close-by energies together with the covariances estimated using the MCD and the identified principal component. It is clear from the figure, that the energy difference causes a shift along the principal component, making it an ideal projection axis for one-dimensional tests. Although the figure shows the principal components of all three displayed samples, in practice only the principal component of the reference sample is used as the axis of projection. The extended test first shifts the observed data according to the obtained location (of the null hypothesis, i.e. the reference sample) and then projects it onto the principal component (again, of the null hypothesis). Finally, a one-dimensional MWW test as described in the previous section determines the test result.

The multivariate extension of the MWW test by projection onto the principal component of the reference sample enables the use of this test with detectors containing multiple layers and - similar to what the comparison in section 4.6.1 is showing - renders it the most powerful test in these situations.
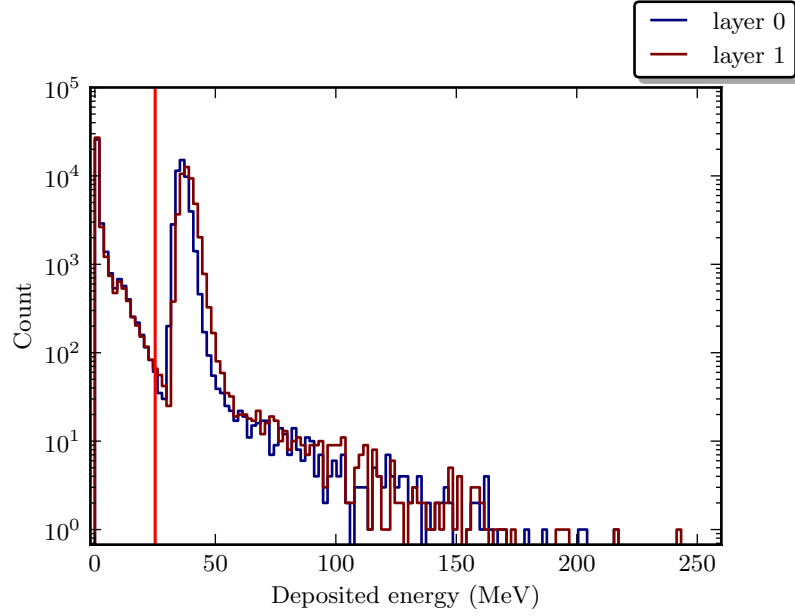
Figure 4.8.: Simulated energy deposits in two consecutive diamond layers by 80 000 high energy carbon ions after traversing a range shifter. The red vertical line indicates the low energy cut. The deposited energies below this cut are attributed purely to secondary particles and therefore almost identical.

4.4.4.6. Nearest-neighbour test

To complete the survey of test candidates, a true multivariate non-parametric two-sample test based on nearest neighbours [78] has been evaluated, but yielded only unsatisfying results.

4.4.5. Low energy cut

In order to improve the test performance, scores (deposited energies) originating from secondary radiation can be ignored. Figure 4.8 shows the score distribution generated by $400\,\text{MeV/n}$ carbon ions in two consecutive diamond layers without any passive absorber in between, after traversing $25.9\,\text{mm}$ of a tungsten range shifter. The distribution above $25\,\text{MeV}$ reproduces the expected Landau distribution of the primary particles, while the distribution below $25\,\text{MeV}$ does not match the Landau shape. The pronounced maximum at low energies and the fact that this part is almost identical in both layers (while the Landau dsitribution has slightly shifted) suggests, that the low energy scores are due to secondary particles. A cut of the scores below $25\,\text{MeV}$ removes the larger part of the noise and therefore improves the power of the test . Although the contribution of secondary particles there is much smaller, the cut can be maintained at lower beam energies, because their Landau distribution is also located above the cut. Naturally, the

cut level must be defined for each particle type separately due to the dependence of the stopping power on the particle weight. For protons, a similar cut has been used at 0.5 MeV (see figure 4.10 for reference; the advantage of the cut is even more visible for 250 MeV protons due to the larger "background").

4.5. Iterative development of the design

The final detector design has been developed through iteration of detector designs starting from a very simple configuration by slowly adding details and increasing realism. The most simple simulation geometry has been realised with Fluka. It simulates the local dose in a homogeneous detector by scoring the deposited dose in a segmented water volume. This geometry already allowed to gain first insights into the distribution of deposited energies described in section 4.5.1. Additionally it was used to obtain a first estimate of the expected annual averaged over all beam energies.

As a next step, the detector material was changed from water to carbon. Then the segmentation resolution was increased while monitoring the distribution of deposited energies. Their location and scales and their sensitivity to beam energy changes as a function of the segmentation gave a first rough idea of the number and thickness of necessary detector layers.

4.5.1. Bragg-peak test revisited

The first approach to a depth-dose measurement was to fit a semi-analytical Bragg-peak model to the simulated measurement data (see section 4.4.4.1) The idea was to start with thin detector layers and to understand the energy deposition behaviour. With that understanding, an appropriate (i.e. statistically powerful) data interpretation can be developed. Then, while monitoring the performance, the layer thickness can be increased and/or passive layers can be inserted.

Figure 4.9 shows the deposited energies in a stack of thin layers by 1000 primary particles from a 60 MeV proton beam. A Bragg curve has been fitted into the mean values of the deposited energy. Remarkable are the large standard deviations (the light green error bars) compared to the small inter-quartile distances especially in the first layers. This is due to the long tails of the Landau distribution for energy deposition in thin layers. Figure 4.10 shows the per-layer histograms of the deposited energy for the same simulation, clearly showing the properties of the Landau distribution. However the above explanation fails when regarding the last layers (layer 5 and onwards), where the distribution is no longer Landau-shaped as the particle energies are so low that the layer thickness is no longer thin compared to the remaining particle range (which is a requirement for the validity of the Landau distribution). Also the large ratio of particles never reaching this layer (the magenta line indicates the decreasing transmission probability) contribute to the large standard deviation. Their energy deposition is zero in more than half of the events and they form a special type of outliers.

It is well-known [93] that in situations where a large amount of outliers is expected,

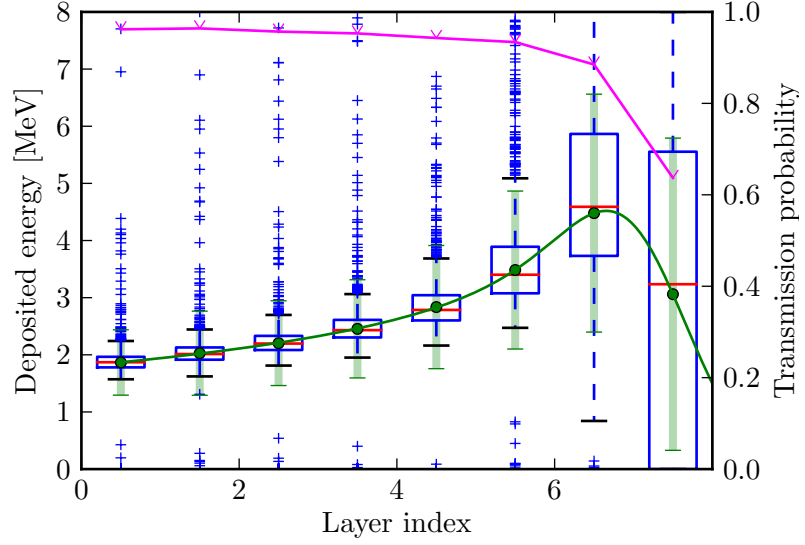Figure 4.9.: Single-particle energy deposits of 60 MeV protons in a stack of 250 μm thin diamond layers after traversing a tungsten absorber of 2.7 mm thickness. The box-plots indicate the energy deposit distributions in each layer: the box extends from the lower to the upper quartile values with a red line at the median; the whiskers (vertical dashed lines) extend from each side of the box to the most extreme data point within 1.5 times the interquartile range; fliers (values outside the whiskers) are indicated by crosses. The dots represent the mean values described by the fitted Bragg curve. The magenta line shows the ratio of the number of primary particles reaching each layer to the initial number of primary particles, i.e. the transmission probability up to a given layer.
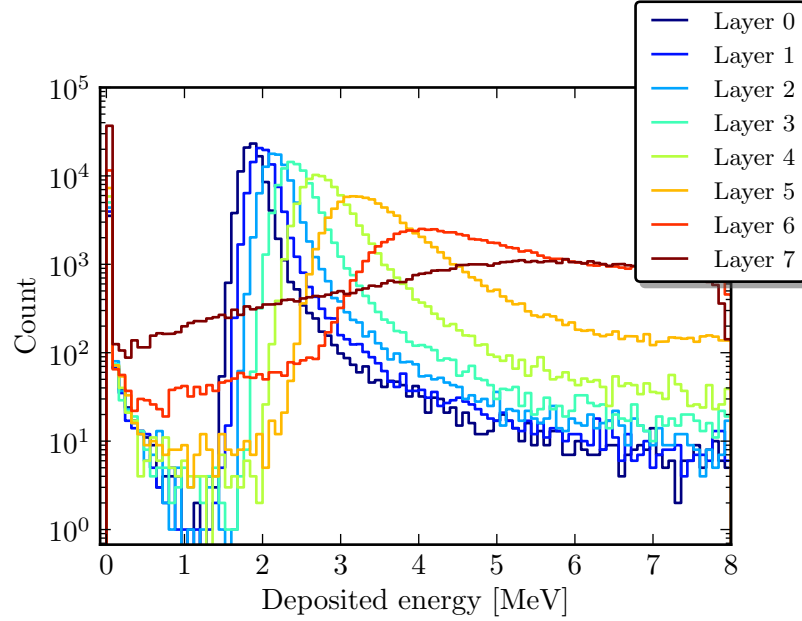
Figure 4.10.: Per-layer histograms of deposited energy for the same simulation run as displayed in figure 4.9, but for 100 times more events.

the classical estimators for location and scale (i.e. the mean and standard deviation) are inappropriate due to their sensitivity to outliers. Additionally, the asymmetry of the underlying distribution distorts the classical estimators. Unfortunately, the Bragg-curve shape is no longer maintained when using other estimates such as the median and a fit of the Bragg curve becomes impossible.

An alternative strategy to fitting the Bragg curve is statistical testing of the measured quantities. Instead of a fit, the measurement outcome is compared to the expected outcome for the expected energy e.g. it could be tested whether the mean deposited energies lie on the expected Bragg curve. This has the advantages, that it is computationally cheaper and that fit instabilities are avoided. Also this approach is more general and can also be applied to other location estimates with the only difference that the expected values do not lie on a Bragg curve. Empirically, the expected locations can be determined using a reference sample. Using this method, different estimators can be compared. In addition to testing the result of each layer independently, correlations between the layers can further improve the test performance because they take into account additional information. Section 2.4 contains an overview of some of the most promising methods.

4.5.2. Range shifter

As a next step, the geometry was refined by separating the layers from each other (in vacuum) to obtain a spaced stack of detectors. As expected, for relatively large layer
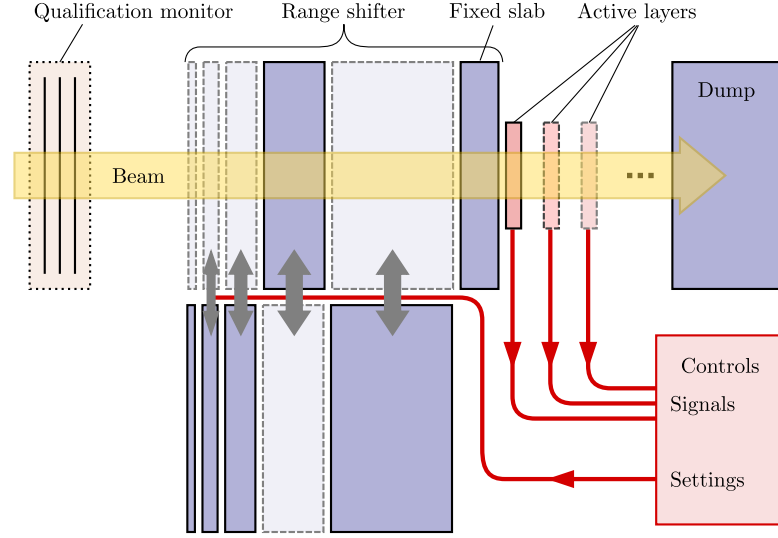
Figure 4.11.: Schematic layout of the detector with a range shifter. The range shifter settings determine how much material the particles have to traverse before reaching the detector layers. Only one layer is drawn with solid lines and the others with dashed lines, since additional layers are optional (see section 4.6.2). The order of the range shifter slabs is chosen such as to have the absorbers as close to the detector as possible. Therefore, the fixed part of the range shifter is closest to the detector.

surfaces, the distance between the layers did not change the detector performance. To further improve the design, the minimum number of necessary (active) layers had to be determined. The number of active layers can be decreased by gradually replacing active layers with passive ones. The most important active layers, i.e. those that contribute most to the overall detector performance, are the layers in the region of the dose peak because their signal is most sensitive to small energy deviations. Consequently, the layers in the flat dose region before the peak can be replaced by passive absorbers until the only remaining active layers are those on the peak region. The stack of passive absorbers that precedes the active layers is called a "range shifter", as it effectively shifts the dose peak into a region of a few active layers by using more or less passive layers depending on the particle range.

The number of necessary range shifter steps must be chosen such that the performance remains stable throughout the entire energy spectrum of all particle types. The choice of range shifter setting is a function of the range of the tested particles in the range shifter material. Therefore, the lower and upper boundary of range-shifter settings is dictated by lowest and highest particle range when regarding all particle types (R_{min} and R_{max} respectively), which is the range of protons at $60\,\mathrm{MeV}$ and $250\,\mathrm{MeV}$ respectively ($3.2\,\mathrm{cm}$ and $38.0\,\mathrm{cm}$ respectively).

The minimum range shifter thickness S_{min} is given by the largest value at which the test performance for 60 MeV protons is still acceptable, and the maximum range shifter thickness S_{max} is given by the smallest value at which the test performance for 250 MeV protons is already acceptable. Together with the number of range shifter slabs p, the following relation determines the thickness of the range shifter S at a given particle range R:

$$S = S_{\mathrm{min}} + \frac{S_{\mathrm{max}} - S_{\mathrm{min}}}{2^p - 1} \times \mathrm{trunc}\left(2^p \frac{R - R_{\mathrm{min}}}{R_{\mathrm{max}} - R_{\mathrm{min}}}\right) \tag{4.2}$$

The numerical values depend on the choice of range shifter material and will be given for the finally proposed design in section 4.6. The constant term S_{min} corresponds to the thickness of a fixed range shifter which is the last slab before the first active layer and never removed from the beam path. Figure 4.11 shows a schematic layout of the detector when using a range shifter. The slabs of increasing thickness can be moved in and out of the beam path depending in the range shifter setting.

4.5.3. Read-out noise & threshold

The read-out of the diamond detectors has not been simulated in detail. Instead of simulating the number of generated electrons and their electronic processing before converting the signal back to a value for the deposited energy, the noise contribution has simply been emulated by adding random energy errors to the deposited energies as explained in section 4.2.6.

In practice this means that after simulating the energy deposition using the Monte-Carlo code as explained in section 4.3, the resulting scores $\hat{y}$ were each multiplied by an independent random factor. These factors were generated using a constant random seed (to maintain reproducibility) and then calling the `numpy.random.randn` method [63] for the shape of the scores and multiplying the resulting values X by the Root Mean Square (RMS) σ_{rel} of the desired relative energy error. Hence the final scores are:

$$y = \hat{y} \times (1 + \sigma_{\mathrm{rel}} X)$$

The threshold commonly used to suppress electronic noise is anyway overrun by the low energy cut explained in section 4.4.5, which surpasses the noise level of 1 % by at least an order of magnitude.

4.6. Design decisions & benchmarks

The parameters of the final detector design are summarised in table 4.4. The selection criterion for the optimum parameter values is the detector performance in terms of statistical power. From the number of parameters it is obvious that a global optimisation is not practical. In the following, the chosen parameter values will be presented together with an evaluation of the alternatives if applicable and a short rationale for the choice.

Test method	Mann-Whitney-Wilcoxon
Number of active layers	2
Active layer thickness	$0.25\,\mathrm{mm}$
Active layer surface	$5 \times 5\,\mathrm{mm}^2$
Range shifter material	Tungsten
Range shifter slabs	7 (1 fixed)
Fixed range shifter thickness	$3.2\,\mathrm{mm}$
Minimum slab thickness	$528.6\,\mathrm{um}$
Range shifter distance	$1\,\mathrm{mm}$
Reference sample size	75000 (proton), 15000 (carbon)
Test sample size	5500 (proton), 800 (carbon)

Table 4.4.: Final design parameters.

Test	Power	Relative speed
Student's t of sample medians	16.5 %	$\approx 6^9$
Student's t of sample Huber Ms	48.0 %	≈ 3
Hotelling's T^2 of sample medians	17.0 %	≈ 1
Hotelling's T^2 of sample Huber Ms	49.5 %	≈ 3
Kolmogorov-Smirnov	64.0 %	≈ 4
Kuiper's	43.0 %	≈ 2
Mann-Whitney-Wilcoxon	85.5 %	1

Table 4.5.: Comparison of the performance of several robust statistical tests applied to energy deposits in a single layer. Hotelling's T^2 test has been applied to data from two layers, as for one layer it would be identical to Student's t test.

4.6.1. Test method

The selection criteria regarding the test method is the statistical performance in terms of power at a given significance. In order for the significance to be meaningful, the uniformity of the test results under the null hypothesis must be given. Table 4.5 provides a comparison of the statistical tests described in section 4.4.4 in terms of statistical power and computational effort. In order to emphasise the power differences, only half the test sample size is used (i.e. 400 events). All tests have been applied to the same set of test samples and reference samples simulated for a $400\,\mathrm{MeV/n}$ carbon beam. The computational effort is quantified relative to the MWW for a constant projection vector. The given numbers can only provide a very rough idea and should serve merely illustrative purposes, since the actual effort can be highly implementation-dependent. From the comparison, the clear winner is the MWW.
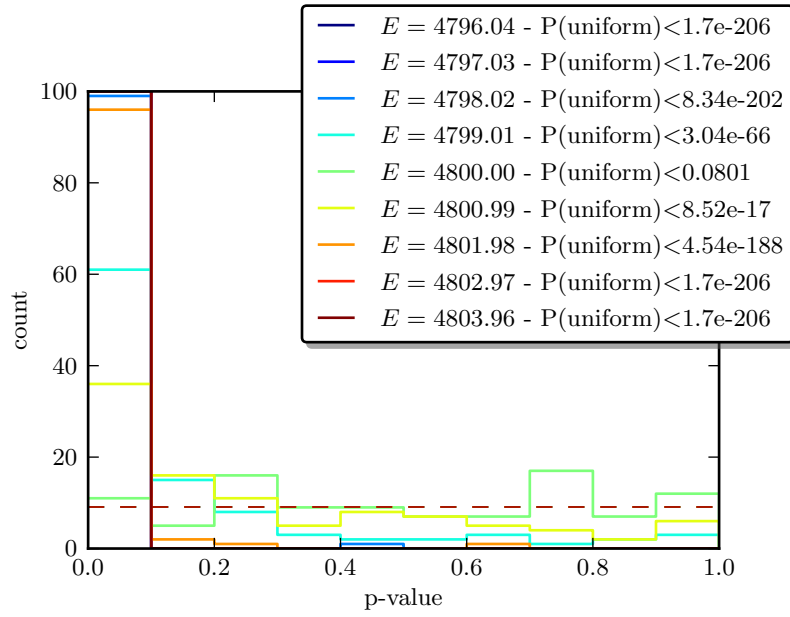
Figure 4.12.: *p*-value histrograms for different beam energy offsets from a high energy carbon ion beam corresponding to the performance plot in figure 4.17b. The correct energy must result in a uniform distribution in order for the significance to be predictable. The probabilities in the legend show the results of a χ^2 test for uniformity.
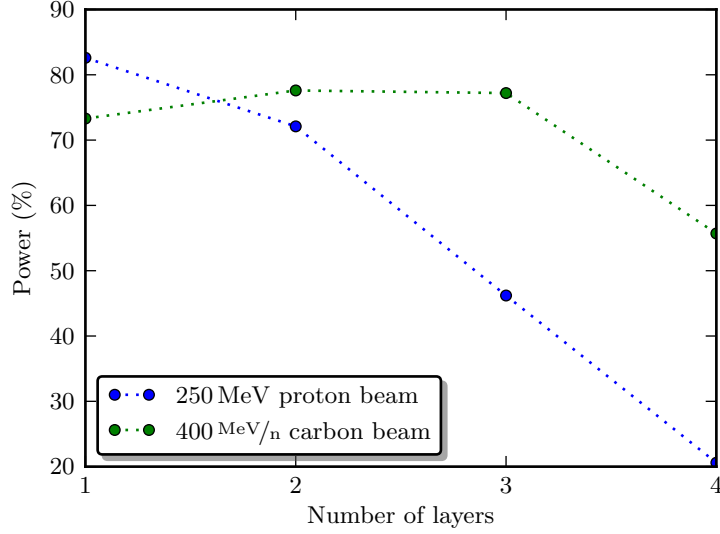
Figure 4.13.: Simulated power of energy verification as a function of the number of active layers. To emphasise the differences between different settings, the power was reduced by using only half the foreseen sample size (see section 4.6.10) for the simulation results shown in this plot.

4.6.2. Number of layers

The number of active layers has been chosen to be as low as possible. A single layer suffices to achieve the required performance and additional layers can even reduce the performance due to the increased scattering and particle losses (see figure 4.13). Nevertheless, a second layer provides redundant information and therefore increases the availability of the detector. The other parameters have been chosen such that the required performance is achieved with one operating layer.

4.6.3. Layer thickness

The layer thickness has been chosen to conform with commercial off-the-shelf components. Typically diamond detectors are available with $0.5\,\mathrm{mm}$ or $0.25\,\mathrm{mm}$ thickness. Thinner detectors are cheaper and the performance in the intended application is comparable or better. Table 4.6 shows the simulated performance for both thicknesses and high energy proton and carbon ion beams.

Active layer thickness	0.25 mm	0.5 mm
250 MeV proton beam	82.6 %	88.6 %
400 MeV/n carbon ion beam	80.6 %	73.3 %

Table 4.6.: Simulated power of energy verification for layers of 0.5 mm or 0.25 mm thickness and proton and carbon ions beams.
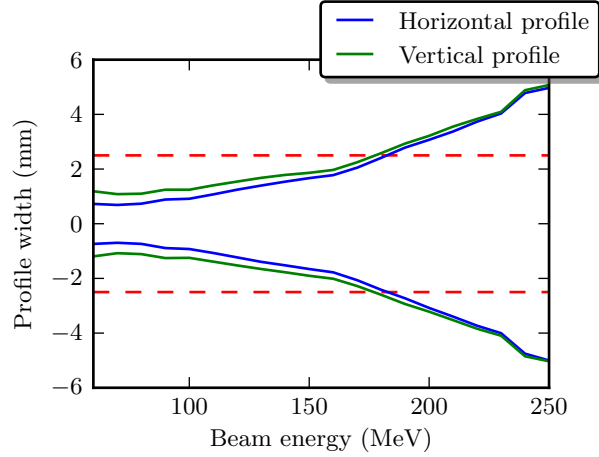

Figure 4.14.: Interquartile range of the particle hits on the first active layer after the range shifter for a proton beam (carbon suffers from less scattering and therefore less growth). The horizontal and vertical profile midrange is shown as blue and green lines respectively. The red dashed lines indicate the dimensions of the suggested diamond detector ($5 \times 5 \, mm^2$). For those dimensions, roughly 35 % of the 250 MeV protons hit the detector.

4.6.4. Layer surface

The surface of the available diamond detectors is limited and the largest commonly available size has been chosen, which is $5 \times 5 \, mm^2$. A smaller detector surface means a lower signal, because the transverse blow-up of the beam especially at high beam energies means that less energy is deposited in the active volume. Figure 4.14 shows the interquartile ranges of the transversal coordinates of the hits on the first active layer.

4.6.5. Range shifter material

Due to the little available space and the small layer surface, it is imperative to constrain the transverse blow-up of the beam as much as possible. This is achieved by choosing a material with a high atomic number. Tungsten stops even the highest energetic beams foreseen at MedAustron within a few centimetres. The resulting compactness together with good thermal conductivity made it the material of choice for the range shifter.

4.6.6. Range shifter slabs

As pointed out in section 4.5.2, the number of range shifter slabs must be chosen such that the detector performance is stable over the entire energy range. At the same time, fewer slabs simplify the mechanical construction. With 6 slabs, the requirements are fulfilled, corresponding to a step size of approximately 0.5 mm (see 4.6.8).

4.6.7. Fixed range shifter thickness

The fixed range shifter thickness is determined by the beam possessing the minimum particle range. The maximum thickness at which the detector is still acceptable is chosen. For 60 MeV protons, a tungsten range shifter must not be thicker than 3.2 mm.

4.6.8. Minimum slab thickness

The minimum slab thickness is an immediate consequence of the maximum range shifter thickness and the number of slabs. The maximum thickness is the smallest thickness at which the detector performance is still acceptable for the particles with the highest range. For 250 MeV protons, a tungsten range shifter must not be thinner than 36.5 mm. The minimum slab thickness is therefore:

$$S_{\text{slab}} = \frac{S_{\text{max}} - S_{\text{min}}}{2^p - 1} = \frac{36.5\,\text{mm} - 3.2\,\text{mm}}{2^6 - 1} \approx 0.5286\,\text{mm} \tag{4.3}$$

4.6.9. Distance of the range shifter to the detector

The distance between the last range shifter slab and the first active layer is important for the number of particles that contribute to the signal. Due to the low energy of the particles that leave the range shifter and consequently their large angles, only an active layer that is close to the range shifter will collect a large amount of particles. In the simulations used for the performance numbers in this section, a distance of 0.5 mm has been used throughout. For low beam energies, larger distances may be advantageous to decrease the radiation damage in the detector because it otherwise receives much more particles than for high beam energies (due to the smaller blow-up compared to the larger range shifter).
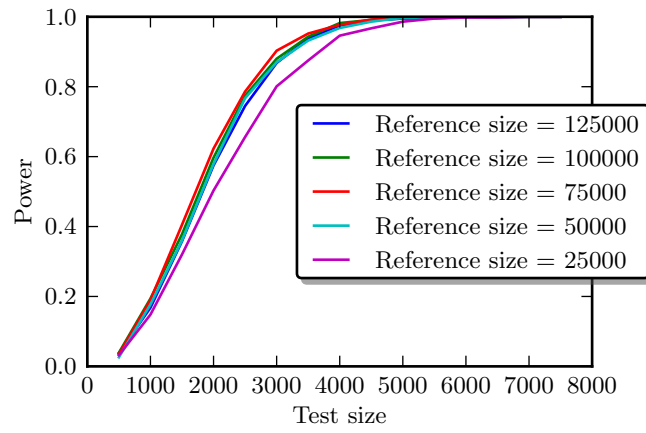
4.6.10. Reference and test sample size

The choice of a reference sample size is a balance between test performance and computational effort. The test sample size is a balance between test performance and bandwidth. Also, if the necessary test sample size is reduced, the dose on the active layer can also be reduced by moderating the number of impinging particles through the distance between the range shifter and the active layer.

Based on a power analysis (see figure 4.15), the following sample sizes have been chosen: For proton beams, the reference sample must contain at least 75000 events (i.e. primary particles) and each measurement must contain at least 5500 events. For carbon ions
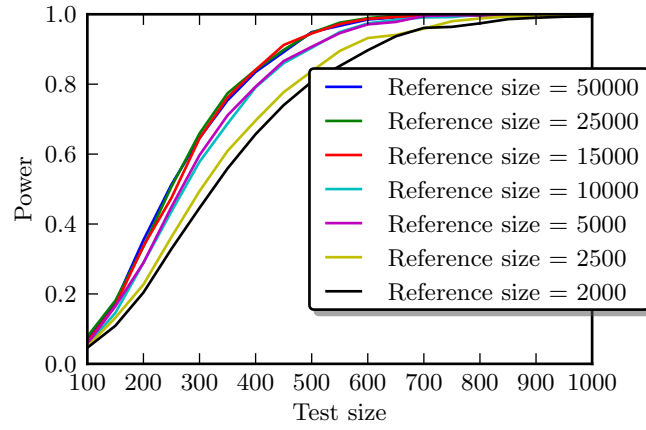
(a) High energy carbon ions.

(b) High energy protons.

Figure 4.15.: Empirical power analysis of different reference and test sample sizes.
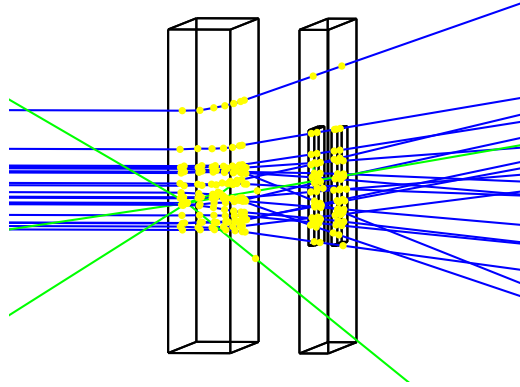
Figure 4.16.: Schematic view of the detector with the fixed pre-absorber and two active layers (the small volumes inside the right-hand side block) and 20 proton events at 60 MeV.

beams, the reference sample must contain at least 15000 events and each measurement must contain at least 800 events. These numbers have been chosen based on a statistical power of 99.7 %. The given values are minima, because more events only improve the power.

4.6.11. Radiation dose

The same simulation ran for plotting figure 4.14 in section 4.6.4 has been used for evaluating the foreseen yearly dose in the active layers. The dose deposited in the first active layer by protons per year is approximately 0.1 MGy, the dose deposited by carbon ions per year is approximately 0.44 MGy, hence the total expected dose per year in the first active layer is approximately 0.54 MGy (the corresponding dose in the second layer is about the same).

4.7. Beam halo option

The measurement discussed so far is a qualification measurement, meaning that it verifies the beam energy at the beginning of every extraction. After the beam has been successfully qualified, the detector receives no further particles and therefore has no possibility to detect energy changes later on during the extraction. If the detector is placed in a different location, possibly close enough to the beam that a certain small amount of the beam periphery is absorbed, the energy can be monitored continuously. Unfortunately the small number of primary particles together with the blow-up at high energies reduce the signal below the minimum test sample size and render this method impractical.
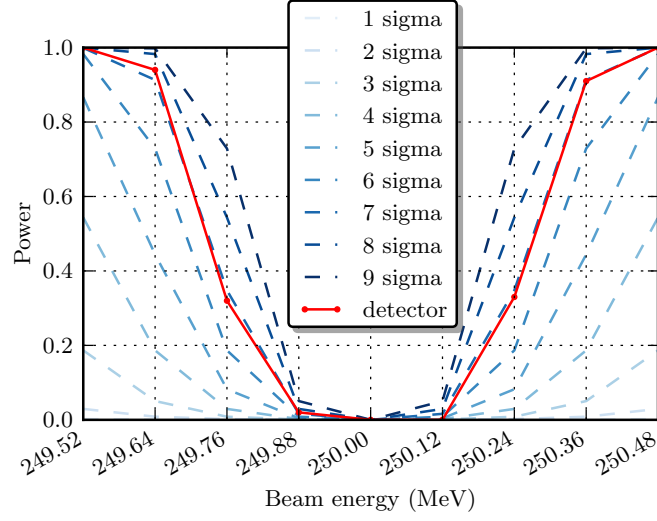
(a) 250 MeV proton beam.
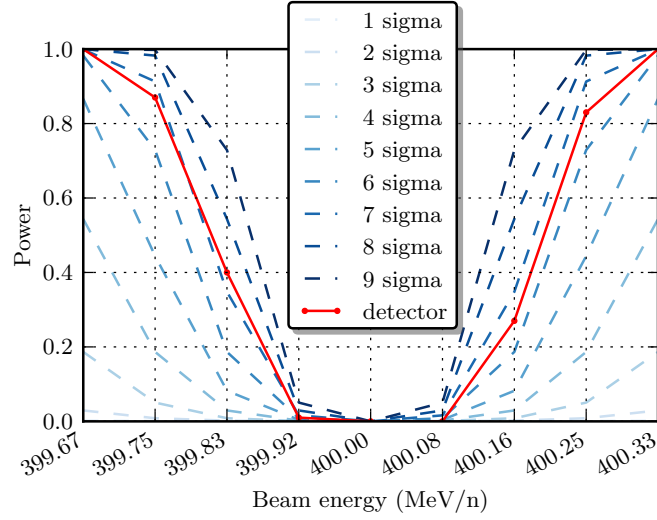
(b) 400 ᴹᵉⱽ/ₙ carbon ion beam.

Figure 4.17.: Power of the energy verification detector for a high energy proton and carbon ion beam at different energy offsets. The minimum and maximum plotted energy correspond to the maximum acceptable energy offset ΔE. The dashed lines show the power of an energy measurement at different precisions ranging from $\sigma = \Delta E$ to $\sigma = \Delta E/9$. Comparison shows that a similar statistical power (at constant significance) can only be achieved with an energy measurement of a 1σ precision between $\Delta E/6$ and $\Delta E/7$.

4.8. Results & risk assessment

A detector for energy verification has been designed and characterised by simulation. It is composed of a tungsten range shifter with 6 slabs ranging from roughly 0.5 mm to 16.5 mm thickness providing 64 discrete steps and two redundant $5 \times 5 \times 0.5$ mm single-crystal diamond detectors connected to low-noise current integrating read-out electronics. A data interpretation strategy based on a non-parametric two-sample statistical test has been developed, comparing the measurements recorded during beam qualification with a reference sample recorded under controlled conditions. The predicted performance of the test regarding small energy deviations is plotted in figure 4.17 for proton and carbon ions beams at maximum respective energy. The maximum energy tests are the most challenging because the least primary particles reach the active detector layers and contribute to the test statistics. The risk that an incorrect energy outside the limits specified in section 2.3 is used for treatment is reduced by at least 99.5 % with the energy verification detector proposed in this chapter.

5. Summary & Conclusions

Cancer is one of the main causes of death today and 70 % of all cancer patients receive radiation therapy. Compared to traditional X-ray radiation, ion beam therapy has the advantage of almost entirely sparing the tissue surrounding the tumour. This is thanks to the characteristic Bragg peak in the dose curve beyond which almost no dose is applied. The position of the Bragg peak in the target is determined by the energy of the ion beam. When homogeneous dose levels must be achieved inside the target, a "stack" of beams with different energies is required. Unfortunately, errors in the beam energy lead to unacceptable dose inhomogeneities of the stack even at relatively small values.

To maintain acceptable dose levels, the beam energy errors must not exceed ± 0.14 MeV for a 60 MeV proton beam (the limit rises to ± 0.48 MeV for a 250 MeV proton beam) or ± 0.22 MeV/n for a 120 MeV/n carbon beam (here the limit rises to ± 0.33 MeV/n for a 400 MeV/n carbon beam). Those requirements were established by means of simulation of dose homogenity. Apart from these precision requirements, energy verification must be as fast as possible and degrade as little as possible the beam quality and availability.

The approaches for energy verification used by existing facilities were investigated and two options for an energy verification measurement have been regarded in detail. The time-of-flight measurement determines the energy of the bunched beam in the synchrotron before extraction. This is done via an orbit length measurement performed by beam position monitors and a frequency measurement to detect the bunch revolution frequency. The achieved energy precision is limited mainly by the precision of the beam position monitors and the limited measurement time. At the foreseen beam position monitor precision ($\Delta x = 0.4$ mm) and an assumed measurement time of 5 ms, the time-of-flight measurement meets the energy verification requirements. Eventual energy changes during the betatron-core driven 3rd order extraction mechanism – which is intended to be used at MedAustron – when the beam is no longer bunched, must take into account .

The second option is a depth-dose measurement carried out by a novel detector conceptwhich was developed "within this thesis" specifically for the purpose of energy verification. The advantage of this option is that it detects energy errors of the extracted beam and therefore also covers energy errors that happen during the extraction procedure. Unlike the time-of-flight or other energy measurements, this measurement does not determine the energy, but makes a decision whether the beam energy at the moment of measurement matches a given reference beam energy. Consequently, the detector performance is characterised not by an energy precision but by the statistical power to identify incorrect energies. This power depends significantly on the number of particles absorbed during the measurement. The proposed detector concept – based purely on simulation results – consists of a range shifter using 7 tungsten slabs of different thickness and two

5. Summary & Conclusions

$5 \times 5 \times 0.25\,\text{mm}^3$ single-crystal diamond detector layers. It provides a statisitcal power (i.e. probability of rejection of incorrect energies) of at least $99.5\,\%$ at minimum beam intensity.

As there is relatively little additional hardware necessary, the time-of-flight measurement should be performed at least as a fall-back option. If it is decoupled from the conventional control systems (e.g. by a separate frequency measurement outside the Radio Frequency; often refers to the Radio Frequency accelerating cavity (RF) control loop) and reports to a medical supervisory system (e.g. a beam delivery system), this measurement is an effective protection against a large number of errors that can happen during injection and acceleration, e.g. incorrect cycle selection. The depth-dose measurement on the other hand is confined to one relatively simple detector. Therefore the associated sources of errors can be managed more easily than for the time-of-flight measurement. The detector does not interact with any instrument used for the accelerator operation, i.e. it is an entirely redundant safety device. However, while being the potentially superior energy verification method, it needs to be prototyped and tested before a unreserved recommendation can be given.

A. Derivations

A.1. Arc length

The arc length differential ds of a curved path in polar coordinates for an arc radius, which depends on the sector angle $r = f(\theta)$, is

$$
\begin{aligned}
ds &= \sqrt{dx^2 + dy^2} \\
&= \sqrt{\left(\frac{dx}{d\theta}\right)^2 + \left(\frac{dy}{d\theta}\right)^2}\, d\theta \\
&= \sqrt{\left(r\cos\theta + \frac{dr}{d\theta}\sin\theta\right)^2 + \left(-r\sin\theta + \frac{dr}{d\theta}\cos\theta\right)^2}\, d\theta \\
&= \sqrt{r^2 + \left(\frac{dr}{d\theta}\right)^2}\, d\theta
\end{aligned}
$$

A.2. Arc length integral

The arc length of a curved path with a variable radius $r = \rho + x$, which depends on the distance s along the arc, where the variations x are small $(x \ll \rho)$, slow $(dx/ds \ll 1)$ and only linear $(dx/ds \approx \text{const})$, the line integral can be simplified:

$$\ell^\star = \int_{\ell^\star} ds^\star$$

$$= \int_a^b \sqrt{\left(\frac{\rho + x}{\rho}\right)^2 + \left(\frac{dx}{ds}\right)^2} \, ds$$

$$= \int_a^b \left(\frac{\rho + x}{\rho}\right) \sqrt{1 + \left(\frac{dx}{ds}\right)^2 \left(\frac{\rho}{\rho + x}\right)^2} \, ds$$

$$= \int_a^b \left(\frac{\rho + x}{\rho}\right) \left[1 + \frac{1}{2}\left(\frac{dx}{ds}\right)^2 \left(\frac{\rho}{\rho + x}\right)^2\right] ds$$

$$= \int_a^b \left(\frac{\rho + x}{\rho}\right) ds + \frac{1}{2}\left(\frac{dx}{ds}\right)^2 \int_a^b \left(\frac{\rho}{\rho + x}\right) ds$$

$$= \ell + \int_a^b \left(\frac{x}{\rho}\right) ds + \frac{1}{2}\left(\frac{dx}{ds}\right)^2 \int_a^b \left(\frac{\rho}{\rho + x}\right) ds$$

A.3. Logarithm series representation

$$\log\left(\frac{a + x}{a}\right) = -\sum_{k=1}^{\infty} \frac{(-1)^k \left(\frac{x}{a}\right)^k}{k} \qquad \forall \left|\frac{x}{a}\right| < 1$$

Bibliography

[1] Council directive 93/42/EEC of 14 june 1993 concerning medical devices. *OJ*, L (169):1–43, 1993. 1.3.1

[2] Bundesgesetz betreffend Medizinprodukte, 1996. URL `http://www.ris.bka.gv.at/GeltendeFassung.wxe?Abfrage=Bundesnormen&Gesetzesnummer=10011003`. 1.3.2

[3] Council directive 96/29/Euratom of 13 may 1996 laying down basic safety standards for the protection of the health of workers and the general public against the dangers arising from ionizing radiation. *Official Journal of the European Union*, L(159):1–114, 1996. 1.3.1

[4] Council directive 97/43/Euratom of 30 june 1997 on health protection of individuals against the dangers of ionizing radiation in relation to medical exposure, and repealing directive 84/466/Euratom. *Official Journal of the European Union*, L (180):22–27, 1997. 1.3.1

[5] Directive 2006/42/EC of the european parliament and of the council of 17 may 2006 on machinery, and amending directive 95/16/EC. *Official Journal of the European Union*, L(157):24–86, 2006. 1.3.1

[6] Kolmogorov–Smirnov test. http://en.wikipedia.org/wiki/Kolmogorov-Smirnov_test, 2012. URL `http://en.wikipedia.org/wiki/Kolmogorov-Smirnov_test`. 4.4.4.4

[7] Kuiper's test. http://en.wikipedia.org/wiki/Kuiper's_test, 2012. URL `http://en.wikipedia.org/wiki/Kuiper's_test`. 4.4.4.4

[8] P. Adzic, N. Almeida, D. Andelin, et al. Radiation hardness qualification of PbWO4 scintillation crystals for the CMS electromagnetic calorimeter, 2009. URL `http://cdsweb.cern.ch/record/1230325`. 2.6.3.2

[9] S. Agostinelli, J. Allison, K. Amako, et al. Geant4—a simulation toolkit. *Nuclear Instruments and Methods in Physics Research Section A: Accelerators, Spectrometers, Detectors and Associated Equipment*, 506(3):250 – 303, 2003. 1.1.2, 2.1.2, 4.3.1

[10] Francesc Alted, Ivan Vilata, et al. *PyTables: Hierarchical Datasets in Python*. 2002. 4.3.1

[11] Ugo Amaldi and M. Silari, editors. *The TERA project and the Centre for Oncological Hadrontherapy*, volume 1. INFN, Rome, second edition edition, 1995. 2.1.1

Bibliography

[12] L. Arnaudon, B. Dehning, A. Hofmann, et al. Effects of terrestrial tides on the LEP beam energy. *Nuclear Instruments and Methods in Physics Research Section A: Accelerators, Spectrometers, Detectors and Associated Equipment*, 357(2-3):249–252, 1995. 3.2

[13] David Ascher, Paul F. Dubois, Konrad Hinsen, et al. *Numerical Python.* Livermore, CA, UCRL-MA-128569 edition, 1999. 4.3.1

[14] V Auzelyte, F Andersson, M Elfman, et al. On-line measurement of proton beam current in pA range. *Nuclear Instruments and Methods in Physics Research Section B: Beam Interactions with Materials and Atoms*, 249(1-2):760–763, 2006. 2.6.4.2

[15] L. Badano, S. Rossi, and S. Rossi. Characteristics of a betatron core for extraction in a proton-ion medical synchrotron, 1997. URL `http://cdsweb.cern.ch/record/327305`. 2.5.3.3

[16] G. Battistoni, S. Muraro, P. R. Sala, et al. The FLUKA code: Description and benchmarking. In M. Albrow and R. Raja, editors, *Proceedings of the Hadronic Shower Simulation Workshop 2006*, volume 896, pages 31–49, Fermilab, 2007. AIP Conference Proceeding. 4.3.1

[17] E. Berdermann, M. Pomorski, W. de Boer, et al. Diamond detectors for hadron physics research. *Diamond and Related Materials*, 19(5-6):358–367, 2010. 4.2.3

[18] T Bortfeld. An analytical approximation of the bragg curve for therapeutic proton beams. *Medical Physics*, 24(12):2024–2033, 1997. 2.1.2

[19] Daniel Boussard and Daniel Boussard. Schottky noise and beam transfer function diagnostics, 1995. URL `http://cdsweb.cern.ch/record/302475`. 3.5

[20] P. J. Bryant, L. Badano, M. Benedikt, et al. *Proton-Ion Medical Machine Study*, volume 1. CERN, Geneva, 2000. 2.1.1, 2.1.3, 2.5.2.1, 3.1.1, 3.2.4

[21] Y. Chen and S. Ahmad. Evaluation of inelastic hadronic processes for 250 MeV proton interactions in tissue and iron using GEANT4. *Radiation Protection Dosimetry*, 136(1):11 –16, 2009. 4.2.2

[22] R Cirio, E Garelli, R Schulte, et al. Two-dimensional and quasi-three-dimensional dosimetry of hadron and photon beams with the magic cube and the pixel ionization chamber. *Physics in Medicine and Biology*, 49(16):3713–3724, 2004. 2.6.5.2

[23] G Cirrone, G Cuttone, S Lonigro, et al. Dosimetric characterization of CVD diamonds irradiated with 62MeV proton beams. *Nuclear Instruments and Methods in Physics Research Section A: Accelerators, Spectrometers, Detectors and Associated Equipment*, 552(1-2):197–202, 2005. 4.2.4

122

[24] G.A.P. Cirrone, G. Cuttone, S. Guatelli, et al. Implementation of a new monte Carlo-GEANT4 simulation tool for the development of a proton therapy beam line and verification of the related dose distributions. *IEEE Transactions on Nuclear Science*, 52(1):262–265, 2005. 4.3.1

[25] G. Coutrakon, D. Miller, N. Wang, et al. Dose error analysis for a scanned proton beam delivery system, 2005. 2.2.2.4, 2.2.3

[26] Wim de Boer, Johannes Bol, Alex Furgeri, et al. Radiation hardness of diamond and silicon sensors compared. *physica status solidi (a)*, 204:3004–3010, 2007. 4.2.1

[27] Rudolf Dölling. Progress of the diagnostics at the PROSCAN beam lines. In *Proceedings of DIPAC 2007, Venice, Italy*, pages 361–363, Venice, Italy, 2007. 2.6.4.2, 2.6.4.2

[28] Ulrich Dorda. Baseline specifications of the beam in irradiation rooms. 2.3

[29] Ulrich Dorda. MedAustron accelerator parameter list. Technical Note EN-091202-a-UDO -V1.2, MedAustron, Geneva, 2011. 4.1

[30] Daniele Dubini, Stefano Gallo, Franco Gerardi, et al. The CNAO functional specifications. Technical Note CNA-TNDC-050WXX-00250, Fondazione CNAO, Milano, Italy, 2003. 1.4, 2.2.2.4, 2.2.3

[31] Paul F. Dubois, Konrad Hinsen, and James Hugunin. Numerical python. *Computers in Physics*, 10(3), 1996. 4.3.1

[32] Emmanuel Egger, Leonidas Zografos, Ann Schalenbourg, et al. Eye retention after proton beam radiotherapy for uveal melanoma. *International Journal of Radiation OncologyBiologyPhysics*, 55(4):867–880, 2003. 1.1.4

[33] J. Ferlay, P. Autier, M. Boniol, et al. Estimates of the cancer incidence and mortality in europe in 2006. *Annals of Oncology*, 18(3):581–592, 2006. 1.1.1

[34] Alfredo Ferrari, P. R. Sala, A. Fasso, et al. FLUKA: a multi-particle transport code, 2005. 4.3.1

[35] P. Finocchiaro, A. Amato, G. Ciavola, et al. Low intensity ion beam diagnostics with particle detectors. In *3rd European Workshop on Beam Diagnostics and Instrumentation for Particle Accelerators*, pages 53–57, Frascati, Italy, 1997. Laboratori Nazionali di Frascati. 2.6.4.3

[36] P. Forck, T. Hoffmann, and A. Peters. Detectors for slowly extracted heavy ions at the GSI facility. In *3rd European Workshop on Beam Diagnostics and Instrumentation for Particle Accelerators*, pages 165–167, Frascati, Italy, 1997. Laboratori Nazionali di Frascati. 2.6.4.3

[37] R Frühwirth and M Regler. *Data analysis techniques for high-energy physics.* Cambridge University Press, Cambridge, U.K.; New York, 2000. 4.2.2

[38] R. Garoby. Low level RF and feedback. In *Joint US-CERN-Japan Accelerator School on Frontiers of Accelerator Technology*, pages 455–489, Tsukuba, Japan, 1996. World Scientific. 3.3

[39] Michael T. Gillin, Narayan Sahoo, Martin Bues, et al. Commissioning of the discrete spot scanning proton beam delivery system at the university of texas M.D. anderson cancer center, proton therapy center, houston. *Medical Physics*, 37(1):154–163, 2010. 2.6.1.3, 2.6.2.2

[40] Bernard Gottschalk, Rachel Platais, and Harald Paganetti. Nuclear interactions of 160 MeV protons stopping in copper: A test of monte carlo nuclear models. *Medical Physics*, 26(12):2597, 1999. 2.6.4.2

[41] Erich Griesmayer, Heinz Pernegger, Daniel Dobos, et al. High-Resolution energy and intensity measurements with CVD diamond at REX-ISOLDE, 2009. 4.2.1, 4.2.6

[42] The HDF Group. *Hierarchical data format version 5*. 2000. 4.3.1

[43] Mia Hubert, Peter J Rousseeuw, Karlien V, et al. ROBPCA: a new approach to robust principal component analysis. *TECHNOMETRICS*, 47:64—79, 2005. 4.4.4.5

[44] John D. Hunter. Matplotlib: A 2D graphics environment. *Computing In Science & Engineering*, 9(3):90–95, 2007. 4.3.1

[45] IAEA, editor. *Relative biological effectiveness in ion beam therapy*. Number 461 in Technical Reports. International Atomic Energy Agency, Vienna, 2008. 1.1.1, 1.2.1

[46] Standard Imaging. 1D water scanning system. http://www.standardimaging.com. URL `http://www.standardimaging.com`. 2.6.5.2

[47] J Janni. Energy loss, range, path length, time-of-flight, straggling, multiple scattering, and nuclear interaction probability in two parts. part 1. for 63 compounds part 2. for elements 1 ? z ? 92. *Atomic Data and Nuclear Data Tables*, 27(2-3):147–339, 1982. 2.6.2.2, 4.2.2

[48] J. L. W. V. Jensen. Sur les fonctions convexes et les inégalités entre les valeurs moyennes. *Acta Mathematica*, 30(1):175–193, 1906. 3.1.1

[49] A Knopf, K Parodi, H Paganetti, et al. Quantitative assessment of the physical potential of proton beam range verification with PET/CT. *Physics in Medicine and Biology*, 53(15):4137–4151, 2008. 2.6.6

[50] Jeong-Wan Kwon, Hyung-Jun Ryu, Wi-Ho Ha, et al. Development of a CCD-Scintillator device and a Multi-Layer faraday cup for therapeutic proton beam monitoring. *Journal of the Korean Physical Society*, 48(4):759–762, 2006. 2.6.4.2

[51] Lev Davidovich Landau. On the energy loss of fast particles by ionisation. *Journal of Physics-USSR*, 8(201), 1944. 4.2.2

[52] A. Lebedev, V. Kozlovski, N. Strokan, et al. Radiation hardness of wide-gap semiconductors (using the example of silicon carbide). *Semiconductors*, 36(11):1270–1275, 2002. 2

[53] S. Lin, T. Böhringer, Eros Pedroni, et al. A multilayer ionization chamber (MLIC) for proton beam bragg peak curve measurements. 2.6.5.2

[54] Regina Y. Liu and Kesar Singh. A quality index based on data depth and multivariate rank tests. *Journal of the American Statistical Association*, 88(421):252–260, 1993. 4.4.4.5

[55] H. B. Mann. On a test of whether one of two random variables is stochastically larger than the other. *The Annals of Mathematical Statistics*, 18(1):50–60, 1947. 4.4.4.4

[56] Jermey N. A. Matthews. Accelerators shrink to meet growing demand for proton therapy. *Physics Today*, 62(3):22, 2009. 1.2.2

[57] P. Moritz, E. Berdermann, K. Blasche, et al. Diamond detectors for beam diagnostics in heavy ion accelerators. In *3rd European Workshop on Beam Diagnostics and Instrumentation for Particle Accelerators*, pages 153–155, Frascati, Italy, 1997. Laboratori Nazionali di Frascati. 4.2.1

[58] P Moritz, E. Berdermann, K. Blasche, et al. Broadband electronics for CVD-diamond detectors. *Diamond and Related Materials*, 10(9-10):1765–1769, 2001. 2.6.2.3

[59] Fabian Moser, Marcus Palm, and Ulrich Dorda. Beam delivery and verification. Minutes of Meeting MM-091210-a-FMO, MedAustron, 2009. 2.6.1.3

[60] M. F. Moyers, G. B. Coutrakon, A. Ghebremedhin, et al. Calibration of a proton beam energy monitor. *Medical Physics*, 34(6):1952–1966, 2007. 2.3, 2.6.2.2

[61] K Nakamura, K Hagiwara, K Hikasa, et al. Review of particle physics, 2010-2011. review of particle properties. *J. Phys. G*, 37(7A):075021, 2010. 4.2.2

[62] E. Niederlaender. Causes of death in the EU. *Statistics in focus*, (10/2006), 2006. 1.1.1

[63] Travis E. Oliphant. *Guide to NumPy*. Brigham Young University, Provo, UT, 2006. 4.5.3

[64] International Commission on Radiation Units, Measurements, and International Atomic Energy Agency. *Stopping Power and Ranges for Protons and Alpha Particles*. Journal of the ICRU. Oxford University Press, Oxford, 1993. 2.6.2.2

[65] International Commission on Radiation Units, Measurements, and International Atomic Energy Agency. *Prescribing, recording and reporting proton-beam therapy*, volume 2 of *Journal of the ICRU*. Oxford University Press, Oxford, 2007. 2.6.5.1

[66] Marcus Palm and Olaf Nairz. Beam delivery system requirements, 2011. 2.3

[67] Eros Pedroni, R. Bearpark, T. Böhringer, et al. *Conceptual design of a new compact scanning gantry for proton therapy.* Paul Scherrer Institute, 2004. 2.6.1.3

[68] P Pemler, J Besserer, J Deboer, et al. A detector system for proton radiography on the gantry of the Paul-Scherrer-Institute1. *Nuclear Instruments and Methods in Physics Research Section A: Accelerators, Spectrometers, Detectors and Associated Equipment*, 432(2-3):483–495, 1999. 2.6.5.3

[69] Ervin B. Podgorsak, editor. *Radiation Oncology Physics: A Handbook for Teachers and Students.* International Atomic Energy Agency, Vienna, Austria, 2005. 2.6.5.1

[70] M Pomorski, E Berdermann, W Deboer, et al. Charge transport properties of single crystal CVD-diamond particle detectors. *Diamond and Related Materials*, 16(4-7): 1066–1069, 2007. 4.2

[71] Michal Pomorski. *Electronic Properties of Single Crystal CVD Diamond and its Suitability for Particle Detection in Hadron Physics Experiments.* PhD thesis, Johann Wolfgang Goethe Universität, Frankfurt am Main, 2008. 4.2.3, 4.2.4, 4.2.5, 4.2.6

[72] PTCOG. Particle therapy facilities in operation. http://ptcog.web.psi.ch/ptcentres.html, 2011. URL `http://ptcog.web.psi.ch/ptcentres.html`. 1.1.4

[73] PTW. PEAKFINDER water column. http://www.ptw.de/peakfinder.html. URL `http://www.ptw.de/peakfinder.html`. 2.6.5.2

[74] M Rebisz, B Voss, A Heinz, et al. CVD diamond dosimeters for heavy ion beams. *Diamond and Related Materials*, 16(4-7):1070–1073, 2007. 2.6.5.4

[75] Alvin C Rencher. *Methods of Multivariate Analysis; 2nd ed.* Wiley Series in Probability and Mathematical Statistics. Wiley, Newark, NJ, 2002. 4.4.4.3

[76] Sheldon M Ross. *Statistik für Ingenieure und Naturwissenschaftler.* Elsevier Spektrum Akad. Verl., München, 2006. 2.4

[77] Peter J Rousseeuw and Katrien Van Driessen. A fast algorithm for the minimum covariance determinant estimator. *TECHNOMETRICS*, 41:212—223, 1998. 4.4.4.5

[78] Mark F. Schilling. Multivariate Two-Sample tests based on nearest neighbors. *Journal of the American Statistical Association*, 81(395):799–806, 1986. 4.4.4.6

[79] Jacobus Maarten Schippers, J. Duppich, G. Goitein, et al. Considerations on the reliability of the PROSCAN facility. Technical Report Volume 4, PSI, 2004. 1.4

[80] Daniela Schulz-Ertner and Hirohiko Tsujii. Particle radiation therapy using proton and heavier ion beams. *Journal of Clinical Oncology*, 25(8):953 –964, 2007. 1.1.3

[81] Daniela Schulz-Ertner, Anna Nikoghosyan, Christoph Thilmann, et al. Results of carbon ion radiotherapy in 152 patients. *International Journal of Radiation OncologyBiologyPhysics*, 58(2):631–640, 2004. 1.1.4

[82] Sergej Schuwalow. Recent studies of diamond detectors radiation hardness, 2009. 4.2.4

[83] Slavko Simić. On an upper bound for jensen's inequality. *Journal of Inequalities in Pure and Applied Mathematics*, 10(2):5 pp, 2009. 3.1.1

[84] J Slater, C Rossi, L Yonemoto, et al. Proton therapy for prostate cancer: the initial loma linda university experience1. *International Journal of Radiation OncologyBiologyPhysics*, 59(2):348–352, 2004. 1.1.4

[85] Helmuth Spieler. *Semiconductor detector systems*. Semiconductor Science and Technology. Oxford Univ. Press, Oxford, 2005. 4.2.3

[86] O. Toker, S. Masciocchi, E. Nygård, et al. VIKING, a CMOS low noise monolithic 128 channel frontend for si-strip detector readout. *Nuclear Instruments and Methods in Physics Research Section A: Accelerators, Spectrometers, Detectors and Associated Equipment*, 340(3):572–579, 1994. 4.2.5

[87] G. van Rossum and F. L. Drake, editors. *Python Reference Manual*. 2011. 4.3.1

[88] N Vinogradov. A detector of bunch time structure for cw heavy-ion beams. *Nuclear Instruments and Methods in Physics Research Section A: Accelerators, Spectrometers, Detectors and Associated Equipment*, 526(3):206–214, 2004. 2.6.2.3

[89] B. Voss, M. Henske, A. Heinz, et al. Fast measurements of single bragg peaks with an active multi-plane phantom, 2006. 2.6.5.2

[90] Uli Weber and Gerhard Kraft. Design and construction of a ripple filter for a smoothed depth dose distribution in conformal particle therapy. *Physics in Medicine and Biology*, 44(11):2765, 1999. 2.2.1, 2.2.2.4

[91] Jörg Wenninger, Gianluigi Arduini, Claudio Arimatea, et al. Energy calibration of the SPS with proton and lead ion beams. In *Proceedings of 2005 Particle Accelerator Conference*, pages 1470–1472, Knoxville, Tennessee, 2005. 3.3

[92] Richard Wigmans. *Calorimetry : Energy Measurement in Particle Physics*. Clarendon Press, Oxford, 2000. 2.6.3.1, 2.6.3.1, 2.6.3.4

[93] Rand R. Wilcox. *Introduction to robust estimation and hypothesis testing*. Elsevier, Amsterdam, 2nd ed. edition, 2005. 4.4.4.4, 4.4.4.5, 4.5.1

[94] R. R. Wilson. Radiological use of fast protons. *Radiology*, 47:487–491, 1946. 1.1.2

[95] J Ziegler. SRIM-2003. *Nuclear Instruments and Methods in Physics Research Section B: Beam Interactions with Materials and Atoms*, 219-220:1027–1036, 2004. 2.6.5.2